ELECTROPRODUCTION OF KAONS ON HELIUM-3 AND HELIUM-4

A Dissertation

By

Alicia Renee Uzzle

Submitted to the Graduate College of
Hampton University
in partial fulfillment of the requirements
for the degree of

DOCTOR OF PHILOSOPHY

May 2002

This dissertation submitted by Alicia Renee Uzzle in partial fulfillment of the requirements for the degree of Doctor of Philosophy at Hampton University, Hampton, Virginia, is hereby approved by the committee under whom the work has been completed.

Oliver K. Baker, Ph.D.
Chair of Committee

Donald R. Lyons, Ph.D.

Jörg Reinhold, Ph.D.

Benjamin Zeidman, Ph.D.

Donald A. Whitney, Ph.D.
Dean of the Graduate College

Date

ABSTRACT

ELECTROPRODUCTION OF KAONS ON HELIUM-3 AND HELIUM-4. (May 2002)

Alicia Renee Uzzle, B.S., Hampton University;
M.S., Hampton University; Ph.D., Hampton University
Chair of Advisory Committee: Dr. Oliver K. Baker

The coincidence reactions, ^{3,4}He(e,e'K$^+$)YX, where Y is a Λ or Σ hyperon, were measured in experiment E91-016 at Jefferson Laboratory. These coincidence measurements were taken for $Q^2 = 0.35$ GeV^2/c^2 at $\theta_{\gamma K} = 0^o, 6^o$, and 12^0 for an angular distribution. The recently acquired data extend the study of the kaon quasifree production mechanism from deuterium to ^{4}He, the most dense nucleus available. The elementary reaction, p$(e, e' K^+)\Lambda(\Sigma^0)$, provided a comparison for the measurement on ^{3,4}He, and of the Λ/Σ^0 production ratio. This ratio remaining the same for the quasifree production on ^{3,4}He was an assumption used to separate the missing mass distribution for Σ^-. Further investigation of the ^{3,4}He missing mass distributions lead to the search of hyperon bound states.

DEDICATION

To Robert III, Aaron, Jared, and my husband, Robert Jr.

And

My parents Linda and Grant Wallop.

ACKNOWLEDGMENTS

I must first give thanks to my Lord and Savior Jesus Christ. There are no words to express the appreciation that I have for my parents for their unconditional love and never accepting anything less than what they felt I could achieve. I give a special thanks to my grandmother, Mabel Green, for always having words of wisdom and caring hugs. Thanks to my brother and sister, Antonio and Terrall. Thanks to all my family and friends for their love and support. I wish to thank the members of my committee: Dr. Oliver K. Baker, Dr. Donald R. Lyons, Dr. Jörg Reinhold, and Dr. Ben Zeidman. Thanks to the collaboration and spokespersons of E91-016, Ben Zeidman and Jörg Reinhold for providing me the opportunity to work on the experiment. A special thanks to Dr. Baker, my advisor, for his support and encouragement from my undergraduate years at Hampton University to the present. Thanks to the postdoc on E91-016, Frank Dohrmann, for his many trips and phone calls to Jefferson Lab in order to work with me throughout the data analysis. Thanks to the Hall C staff scientists and technicians: Rolf Ent, Dave Mack, Bill Vulcan, Steve Wood, Hamlet Mkrtchyan, Joe Beaufait, Joe Mitchell, and Howard Fenker. Thanks to John Arrington, Jim Dunne, and Herbert

Breuer. I give thanks to the Hampton University faculty and staff: Dr. Keith Baker, Dr. Liquang Tang, Dr. Khin Maung Maung, Dr. Donald Lyons, Dr. Jose Goity, Dr. Cynthia Keppel, Dr. Eric Christy, and Dr. Doyle Temple. I extend a special thanks to Dr. Paul Gueye and the former and present Hampton University graduate students: Dr. Steven Avery, Dr. Jinseok Cha, Dr. Mark Harvey, Dr. Wendy Hinton, Anthony Cochran, Lulin Yuan, Leon Cole, and Ceasar Jackson. Thanks to the former kaon students: Jinseok Cha, Wendy Hinton, Doug Koltenuk, Richard Mohring, Gabriel Niculescu, and Pawel Ambrozewicz.

I give a very special thanks to my loving husband and friend, Rob Jr., and my beautiful sons, Robert III, Aaron, and Jared for giving me the support and understanding that I needed to accomplish this task. Rob encouraged me to work harder at times when I felt like quitting, and I will be forever appreciative of that. I have been truly blessed with a wonderful family, and I hope that I have made them proud of me.

Finally, I need to give thanks to my late great-grandmother, Clara Marshall, whose influence in my life was priceless. Her recent passing deeply saddened me, but I know her love is still shining down on me from Heaven.

TABLE OF CONTENTS

Page

LIST OF TABLES

TABLE Page

LIST OF FIGURES

FIGURE Page

FIGURE Page

FIGURE Page

CHAPTER 1

Introduction and Motivation

1.1 Introduction

The study of nuclear physics provides a description of the forces, reactions, and internal structures of hadronic matter. Understanding nuclear physics is key to understanding the universe, as matter comes from nuclei and nuclear reactions. Quantum hadrodynamics (QHD) are the quantum field theories which describe the interactions between relativistic hadrons [1]. Hadrons are divided into two classes of particles; baryons and mesons. The nucleus of an atom contains baryons, which are a complex system of quarks and gluons. Baryons have half integral spin and participate in the strong, electromagnetic, and the weak force. Mesons have integral spin and masses generally intermediate between leptons and baryons. Baryons are composed of quark triplets (qqq), while mesons are composed of quark-antiquark ($q\bar{q}$) pairs. The complicated many-body system of the quarks and gluons which form the baryon can be described by quantum chromodynamics (QCD), based on the internal color symmetry. The *confinement* of quarks and gluons in the interior of the hadron and the small coupling constant of quarks at very small distances (asymptotic freedom) are two of the most important properties described by QCD [1]. Although QCD provides the most complete description of quark and gluon interactions, it is most difficult, and sometimes impossible, to solve analytically.

The study of nucleon-nucleon interaction in the medium is a significant objective of nuclear physics. The use of electromagnetic probes to study nuclear structure, and nucleon structure with higher energies, is ideal because the electromagnetic interaction is governed by quantum electrodynamics (QED). Electron interactions are well understood and described accurately by QED. There is minimal disturbance to the target because electromagnetic interactions are weak compared to the strong interactions involved with using hadronic probes. This weak interaction allows the electron to probe the entire nucleus with minimal disturbance to the target [2]. Some disadvantages of electron scattering are the smaller cross sections when compared to hadronic scattering and the easily emitted Bremsstrahlung radiation.

1.2 Electromagnetic Production of Strangeness

The use of strangeness in physics allows the investigation of baryonic interactions with a new degree of freedom [3]. This new degree of freedom means that energy levels which are inaccessible by other baryons can be occupied by strange baryons. These baryons that contain a single strange quark are called hyperons. Strange baryons are not constrained by the Pauli Principle, in this case, and can occupy any level in its well [2]. The uniqueness of strange physics is the study of hyperon properties and hyperon-nucleon interactions. Strangeness is conserved in the strong and electromagnetic interactions, but not in the weak interaction [2]. Hypernuclear structure can also be studied when a proton or nucleon in the target nucleus is replaced by a hyperon (a u quark is converted to an s quark in the nucleus). The use of few-body systems, such as D and ^{3,4}He, limits the complexities in studying such interactions [4].

The kaon is the lightest meson that contains a strange quark. The K^+ meson quark constituents are the up quark paired with an anti-strange quark, with a strangeness quantum number of +1. It was discovered in the first half of the 20th century and has a mass of 493.7 MeV. The lightest baryon with strangeness is the isoscalar Λ (uds) hyperon with a mass of 1115.6 MeV. This experiment will also measure the production of Σ^0 and Σ^- hyperons. Table 1.1 lists some of the particles that will be detected and their properties [5].

The field of electromagnetic production of strangeness was slowly abandoned due to the inadequate duty factor of the electron accelerators in the 1970s. The experimental data was very scarce until the more recent abundance of quality data acquired with the high duty factor, high energy, and high quality beam at Jefferson Lab [6]. Data has been available through associated strangeness production with the (K^-,π^-) and (π^+,K^+) reactions [2] [7]. One of the advantages of using hadronic probes is the possibility to reach zero momentum transfer to form a

Particle	Quarks	Mass (MeV)	Charge	I(J^P)
up quark	u	≈ 1 - 5	+ $\frac{2}{3}$ e	$\frac{1}{2}(\frac{1}{2}^+)$
down quark	d	≈ 3 - 9	- $\frac{1}{3}$ e	$\frac{1}{2}(\frac{1}{2}^+)$
strange quark	s	≈ 60 - 170	- $\frac{1}{3}$ e	$0(\frac{1}{2}^+)$
π^-	$\bar{u}$d	139.57	-1e	$1(0^-)$
π^+	u$\bar{d}$	139.57	+1e	$1(0^-)$
K$^+$	u$\bar{s}$	493.68	+1e	$\frac{1}{2}(0^-)$
p	uud	938.27	+1e	$\frac{1}{2}(\frac{1}{2}^+)$
n	udd	939.57	0	$\frac{1}{2}(\frac{1}{2}^+)$
Λ	uds	1115.68	0	$0(\frac{1}{2}^+)$
Σ^0	uds	1192.64	0	$1(\frac{1}{2}^+)$
Σ^-	dds	1197.45	-1e	$1(\frac{1}{2}^+)$

Table 1.1: Properties of some particles and their constituent quarks. These are the mesons and baryons that will be detected and/or studied in E91-016.

hypernucleus. Electroproduction generally gives rise to high momentum transfers which decreases the *sticking* probability of the hyperon in the nucleus. However, a minimal momentum transfer can be achieved when the angle between the photon and kaon is zero. Another notable difference between hadronic and electromagnetic reactions is the pions and kaons preference to excite natural parity, or non-spin flip states due to the pseudoscalar nature. The vector spin nature of the photon causes a preference to excite non-natural parity, or spin-flip states. Probably the most significant advantages of using the electromagnetic process are the relatively small wave distortions and the one-step, well understood reaction mechanism [2].

The electromagnetic process of creating hyperons generally has a large momentum transfer. When sufficient momentum is transferred from the incident particle to the target nucleus, the interaction is considered to occur from a single nucleon. This describes the process of quasifree scattering. Quasifree reactions are useful tools to study the propagation of the nucleons in the nuclear medium, as well as final state interaction effects [8]. The weakly interacting electron can penetrate the nuclear interior allowing the virtual photon to illuminate the entire nuclear volume. In strangeness production, the behavior of the nucleons and the hyperon can be studied [9].

1.3 Previous Measurements

Experiment **E91-016** presents the first data for kaon electroproduction from ^{3}He and ^{4}He targets. Hypernuclear states have been studied by the (K^-, π^-), (π^+, K^+), and stopped K reactions. Recently, evidence of a bound Σ state from ^{4}He was seen in the $^4\mathrm{He}(K^-, \pi^-)$ at Brookhaven National Lab with an energy resolution of 2-3 MeV [10]. This present data will be focusing on quasifree hyperon production due to the large momentum transfer, which is characteristic for electroproduction, but less favorable for hypernuclear states.

In 1996, **E91-016** presented the first measurement on deuterium with sufficient statistics and resolution to clearly separate the Λ and Σ contributions. A parameterization for the angular dependence for Λ production was extracted for the kinematic variables $Q^2, W, t,$ and ϕ which describes the data well [11] [12]. A phase space factor was used to describe the Σ^0 production [13]. The missing mass distribution were well described by the quasifree production, including Y-N final state interactions. The cross sections for Λ, Σ^0, and Σ^- were measured by assuming the nucleons were free in the quasifree region. The D/H Λ cross section ratios were $\sim$ 99%. Treating the proton in deuterium as a free proton lead to the extraction of the Σ^-/Σ^0 ratio of $\sim$ 0.61 for all kinematics. With the comparison of the Clebsch-Gordan coefficients, this ratio agrees with the calculated isospin-$\frac{3}{2}$ exchange. Figure 1.1 displays the missing mass spectrum for deuterium with kinematics similar to this experiment.

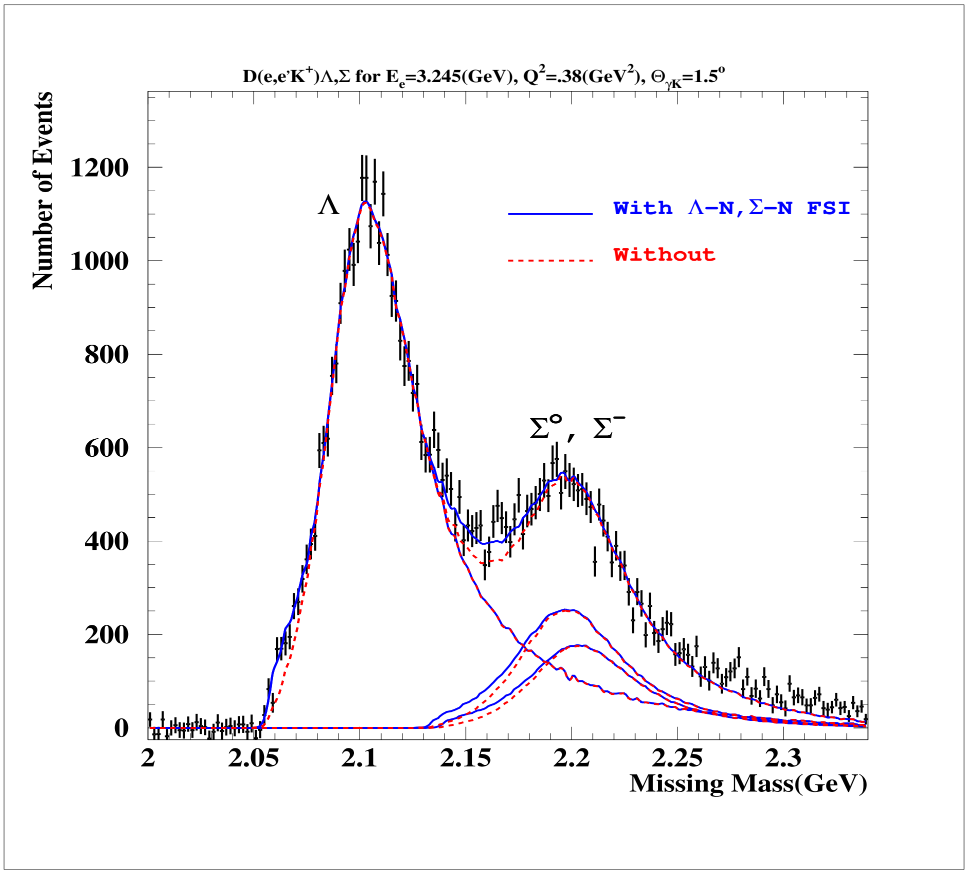

Figure 1.1: 1996 D(e,e'K$^+$) missing mass for $Q^2 = 0.38$ GeV^2. The points are the data and the solid and dashed lines are the simulations with and without FSI.

Quasifree kaon electroproduction from carbon and aluminum was also performed during **E91-016** in 1996. The Fermi motion of the nucleons in the carbon and aluminum target caused the Λ and Σ distributions to be indistinguishable due to the significant overlap of the two regions. The effective proton number was measured by comparing the cross section for Λ production from hydrogen to those from carbon and aluminum [9].

1.4 A(e,e'K$^+$)YN Reaction

1.4.1 Motivation

Kaon electroproduction on ^{3}He and ^{4}He should allow for the extraction of the reaction mechanisms on the proton and the neutron inside the nuclear medium. The helium targets are the lightest complex nuclei that can provide information between two-body and three-body interactions in complex hypernuclei. The study of two-body and three-body systems limits the complexity of possible interactions that can provide valuable information on the features of hyperon-nucleon interactions in the nuclear medium [4] [14]. Equation 1.1 gives the process for kaon electroproduction from ^{3}He and ^{4}He as,

$$e + A \rightarrow e' + K^+ + Y + N \tag{1.1}$$

where, Y is a Λ or Σ^0 if scattering from a proton, or a Σ^- if scattering from a neutron. The residual system, N, has several possible final states. Scattering from a proton in ^{3}He could leave ^{2}H or pn (unbound), whereas, scattering from the neutron leaves pp in the final state. Scattering from a proton in ^{4}He could leave ^{3}H, ^{2}Hn, or pnn (unbound). The possible final states resulting from scattering off a neutron include ^{3}He, ^{2}Hp, or ppn (unbound).

An abundance of quality data of kaon electroproduction on deuterium was taken for **E91-016** in 1996 [11] [13]. The weak binding in the deuterium nucleus lead to the two distinct reaction channels for producing a Λ or Σ which were separable from each other. The missing mass spectra were well described by quasifree production in which the nucleons were assumed to be free. The Λ/Σ^0 production ratio was assumed to be the same as hydrogen. This assumption lead to the extraction of the Σ^- cross section. The binding in the ^{3}He nucleus is $\sim$ 4 times stronger than deuterium and $\sim$ 13 times stronger in the ^{4}He nucleus. The Fermi motion of the nucleons in the helium targets causes a large overlap between the Λ and Σ missing mass regions. The separation of the the Λ and Σ^0 reaction channels was made by also assuming the production from a free proton. The A-dependence of the cross section for each hyperon was also studied. Although the kinematics for producing hypernuclei were not optimized for significant cross sections, the bound regions were studied for any evidence of bound hypernuclear states in both ^{3}He and ^{4}He nuclei. Experiment **E91-016** yielded the first data from kaon electroproduction on ^{3}He and ^{4}He by taking advantage of the continuous wave, high intensity, and high duty factor electron beam at Jefferson Lab.

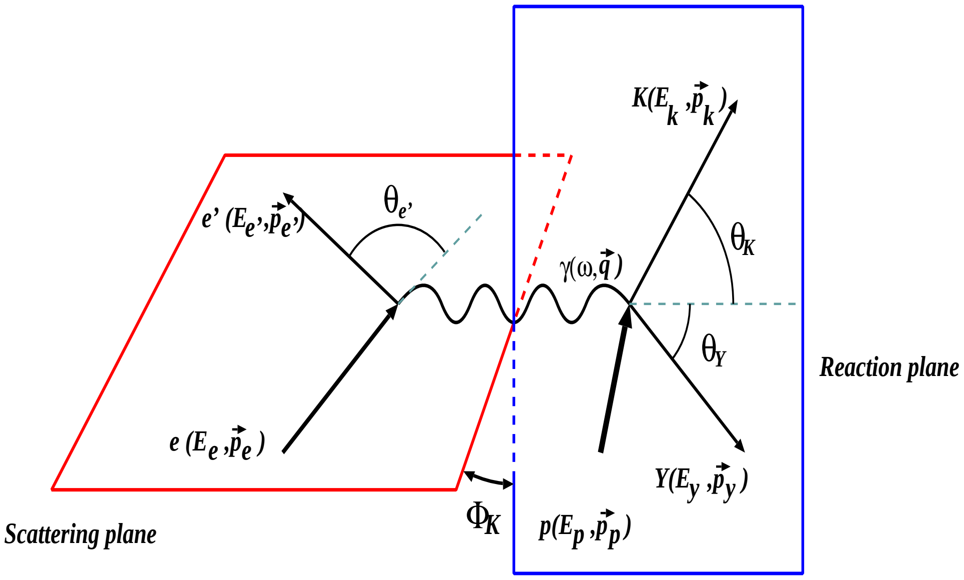

Figure 1.2: Diagram of elementary p(e,e'K^+)Y reaction.

1.4.2 Formalism

The elementary reaction of kaon electroproduction for an electron interacting with a single proton or neutron is illustrated in Figure 1.2 and given as

$$e + p \rightarrow e' + K^+ + \Lambda, \Sigma^0, \tag{1.2}$$

or

$$e + n \rightarrow e' + K^+ + \Sigma^-. \tag{1.3}$$

An incident electron, e, interacts with a proton (or neutron) by radiating a virtual photon, γ, carrying the momentum transfer from the electron to the target. From this exchange, the recoiling kaon (K^+) and the residual system, hyperon (Λ

, Σ^0, or Σ^-), are formed. The incident electron is scattered at an angle, $\theta_{e'}$, and detected in the High Momentum Spectrometer. The K$^+$ travels at an angle, $\theta_{\gamma K}$, with respect to the virtual photon and detected in the Short Orbit Spectrometer. The plane defined by the incident and scattered electron is the scattering plane. The reaction plane is defined by the electroproduced kaon and the hyperon. The Lorentz invariant quantities are given by

$$\begin{aligned} q^2 &= (P_e - P_{e'})^2, && (1.4) \\ s &= (q + M_p)^2, && (1.5) \\ t &= (q - P_{K+})^2, && (1.6) \end{aligned}$$

where P_e, $P_{e'}$, and P_{K+} are the four momenta of the incident electron, scattered electron, and kaon, respectively. The four momentum transfer to the target is denoted as q.

In the center-of-mass frame, the cross section for kaon electroproduction can be expressed as [15],

$$\frac{d\sigma}{d\Omega_{cm}} = \frac{d\sigma_T}{d\Omega_{cm}} + \epsilon_L \frac{d\sigma_L}{d\Omega_{cm}} + \sqrt{2\epsilon_L(\epsilon+1)}\frac{d\sigma_{LT}}{d\Omega_{cm}} cos\phi + \epsilon\frac{d\sigma_{TT}}{d\Omega_{cm}} cos2\phi. \quad (1.7)$$

The term, $\frac{d\sigma_T}{d\Omega_{cm}}$, is the cross section due to transversely polarized virtual photons, while $\frac{d\sigma_L}{d\Omega_{cm}}$ is the cross section due to longitudinally polarized virtual photons. The cross sections due to interference between transversely and longitudinally polarized virtual photons and two different states of transversely polarized virtual photons are given as $\frac{d\sigma_{LT}}{d\Omega_{cm}}$ and $\frac{d\sigma_{TT}}{d\Omega_{cm}}$, respectively. The virtual photon degree of transverse and longitudinal polarization are written as

$$\epsilon = \frac{1}{1 + 2(1 + \frac{\omega^2}{Q^2}) tan^2 \frac{\theta_{e'}}{2}} \tag{1.8}$$

$$\epsilon_L = \frac{Q^2}{\omega^2} \epsilon. \tag{1.9}$$

One of the most recent theoretical efforts to reproduce kaon production is the approach of the isobaric models [3]. The isobaric model attempts to calculate kaon production amplitudes from *one particle exchange* QHD Feynman diagrams with the use of the effective Lagrangian approach. These models include extended Born terms for p, K, and Y, as well as resonant terms for N^* and Y^*. In these exchange Born term diagrams, the $s-$, $u-$, and $t-$ channels are determined by the propagator. The propagator could be a baryon, a strange baryon, or a strange meson. Figure 1.3 shows the $s-$, $u-$, and $t-$ channel Feynman diagrams for a p(e,e'K$^+$)Y reaction [16].

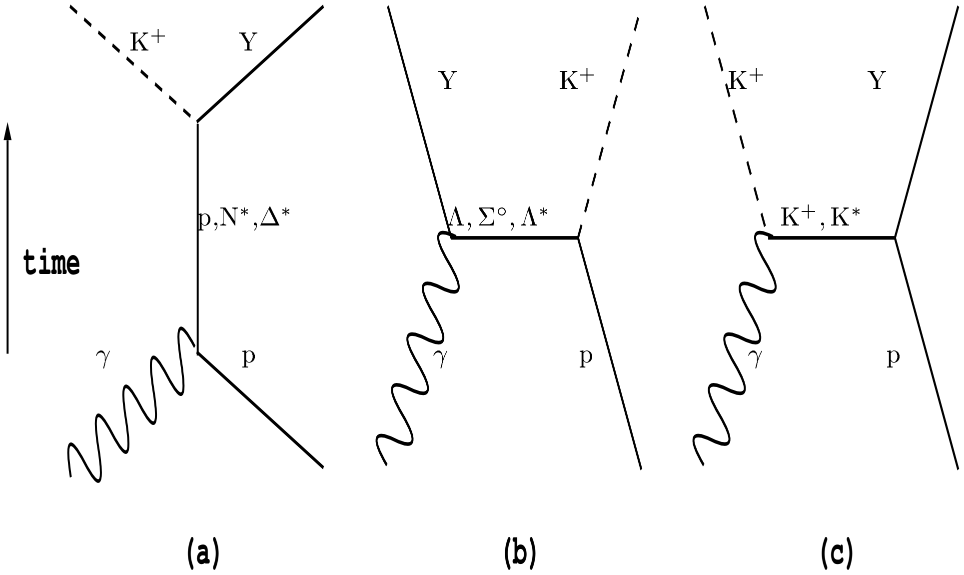

Figure 1.3: Feynman diagrams for p(e,e'K$^+$)Y reaction. The s-channel is shown in (a), u-channel in (b), and t-channel in (c).

1.5 Bound Hypernuclei

In addition to providing information on hyperon-nucleon interactions, measurements of hypernuclear formation was also one of the motivations of **E91-016**. The earlier associated strangeness production and hadronic strangeness exchange reactions were performed to produce the majority of bound hypernuclei. The bound Λ has been observed via the (K^+, π^-) reaction on heavier targets where the neutron was removed and replaced by a recoilless Λ. For the mass 3 system, the only bound state is the $1/2^+$ state where the lambda is weakly coupled to the deuteron by 130 keV. The 0^+ ground state with a lambda binding energy of 2.04 MeV and the 1^+ excited state bound by 1.04 MeV are the two bound states in the ${}^4{}_\Lambda$H hypernucleus. The hadronic reactions were favorable for producing hypernuclei due to the low momentum transfer. The reports from ^{4}He(K^-, π^-) experiments at Brookhaven National Lab give evidence of narrow peaks near sigma threshold which would suggest the observation of a sigma hypernuclear bound state. The ^{3,4}He(e,e' K^+) reaction should be more favorable to producing bound Σ^- due to the Coulumb interaction that was not present in the BNL hadronic reactions. Confirmation of the peak seen near sigma threshold from ^{4}He and the observation of bound sigma in ^{3}He would be quite interesting and have significant consequences. The missing mass spectra were studied for bumps near the values that correspond to threshold production of lambda and sigma.

CHAPTER 2

Experimental Setup

2.1 Overview

Experiment **E91-016**, “Electroproduction of Kaons and Light Hypernuclei”, was run in Hall C at Jefferson Lab during the Fall of 1999. The Continuous Electron Beam Accelerator Facility (CEBAF) was designed to provide high luminosity, 100 % duty factor continuous wave electron beams with energies currently up to 5.7 GeV.

During **E91-016**, the scattered electrons were detected in coincidence with electroproduced kaons in the reaction, e + A $\longrightarrow$ e' + K^+ + X, where A is the target and X is the residual system. Electrons from the CEBAF accelerator with an energy of 3.245 GeV were incident upon liquid ^{3}He, ^{4}He, and deuterium targets located in an evacuated scattering chamber. Data from hydrogen were taken for calibration and normalization, and the yields from a dummy replica of the empty target cell were measured separately for each kinematic setting. The standard Hall C equipment was used during **E91-016**, with the High Momentum Spectrometer (HMS) detecting the scattered electrons and the Short Orbit Spectrometer (SOS) detecting the kaons before their in-flight decay.

2.2 Accelerator

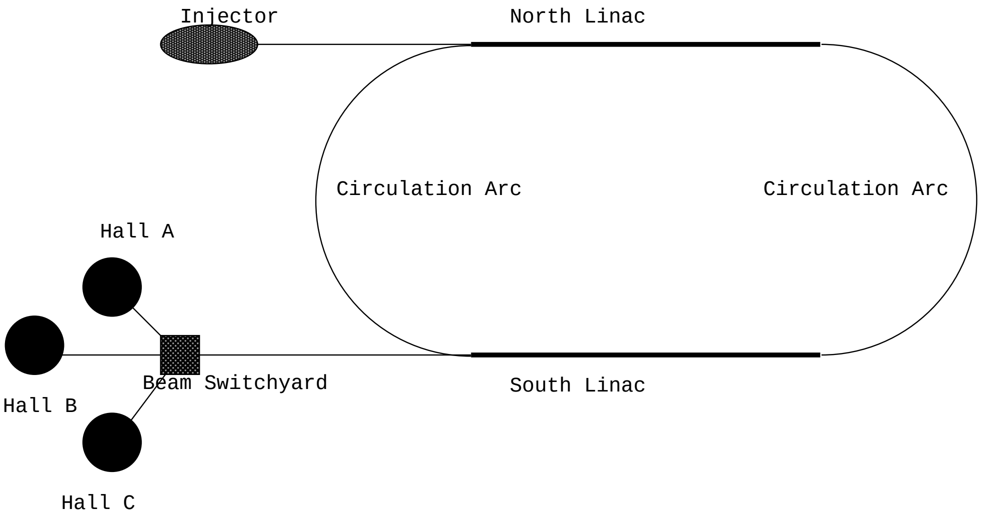

Figure 2.1: Overview of CEBAF and experimental halls.

The CEBAF accelerator at Jefferson Lab is capable of providing a CW unpolarized (polarized) 100% duty factor electron beam with a total current of 200 μA to three experimental halls simultaneously. A schematic diagram of the accelerator is shown in Figure 2.1. The electron beam begins in the injector where it is accelerated up to 45 MeV. It is then accelerated through the north linac by superconducting niobium RF cavities where it gains an additional 400 MeV. The beam is then guided through the east arc and re-injected into the south linac where it gains another 400 MeV. From that point, the beam can be sent to the beam switch yard (BSY) for distribution into the experimental halls or through the west arc and again to the linacs for additional energy gains. After each pass through a linac, the electrons are momentum analyzed and sent through the appropriate circulation arc. A maximum of five passes could be made yielding a maximum energy of 4.045 GeV. Currently, the accelerator has achieved a maximum energy of 5.7 GeV.

The microstructure of the beam consists of short (1.67 ps) beam pulses at a frequency of 1497 MHz. Each hall is designed to get one-third of the total number of beam bunches, resulting in a pulse train of 499 MHz to each hall with the spacing of the bunches 2 ns apart. Typically, the beam has an emittance of 2x10^{-9} mrad. The relative beam energy can be measured with a fractional uncertainty of 10^{-4} and is known absolutely within 10^{-3}. During the running of **E91-016**, Jefferson Lab provided unpolarized, CW electron beams with a nominal energy of 3.245 GeV and currents ranging from 10 to 30 μA.

2.3 Hall C Beamline

Once the electron beam has been accelerated to the desired energy, the beam is sent to the BSY where it is transported to the Hall C arc and into the end station. The arc consists of various monitors for measuring the energy, current, position, and profile of the beam. Figure 2.2 shows the hardware in the Hall C beamline.

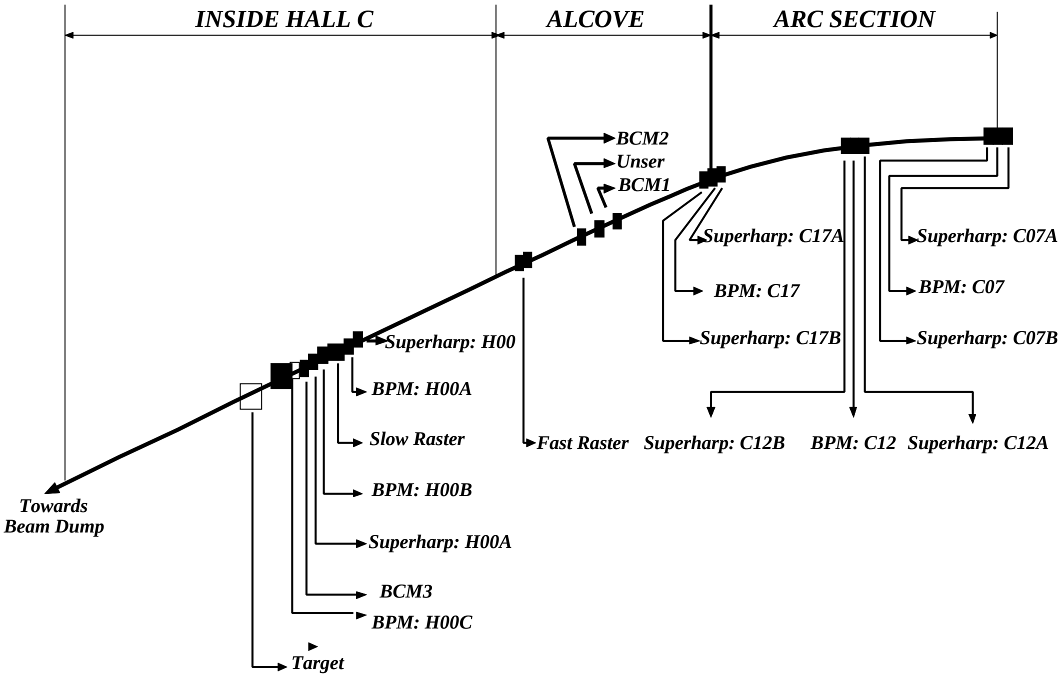

Figure 2.2: Hall C beamline and arc.

2.3.1 Beam Measurements

Beam Energy

A precise measurement of the beam energy was done by using the superharps to measure the absolute beam position at the entrance, middle, and exit of the Hall C arc. The superharp is a wire scanner that measures the horizontal and vertical beam profile. As each of the three wires of the superharp passes through the beam, an ADC measures the signal on the wires and a position encoder measures the position of the ladder. With this information, the position and profile of the beam can be measured. By knowing the settings of the magnets in the Hall C arc and the absolute position from the superharps, the beam energy can be extracted with an absolute uncertainty within 10^{-3}. This process for measuring beam energy is destructive for the beam, so it cannot occur concurrently with data taking.

Beam Position

The position of the beam in the arc and Hall C was monitored using six beam position monitors (BPMs) situated along the beamline for continuous measurement. The BPM is a resonant cavity mounted in the beamline such that its axis will coincide with the nominal axis of the beam. The four antennae on the BPM collect a signal from the fundamental frequency of the beam which is proportional to the distance from the antennae. This information is used to determine the relative (X,Y) position of the beam. Superharp scans are used to calibrate the BPMs so the precision of the position measurement is ±1.0 mm with an uncertainty of 0.1-0.2 mm. The Hall C beamline has three BPMs and two additional superharps.

Beam Current

Beam current measurements in the hall were performed using three beam current monitors (BCMs). The BCM is a microwave cavity in which the beam excites resonant modes. The resonant modes are coupled to the wire loops contained in these cylindrical wave guides. The design of the BCMs is similar to that of the BPMs except that the coupling of interest is that of the transverse electric and magnetic modes which are sensitive to the beam current and insensitive to the beam position. Calibrations for the BCMs were done using a parametric DC current transformer (Unser monitor). Calibration runs were taken once a day in which the beam was alternately turned on and off in 2 minute intervals [17]. Although the Unser monitor has large drifts in the offsets, it has a very stable and absolute gain (measured to 10^{-7}) ; therefore, it was used to calibrate the gain of the cavity monitors during the beam-on periods. During the beam-off periods, the offsets of the BCMs and the Unser monitor could be determined.

2.3.2 Beam Rastering

The CEBAF accelerator produces an electron beam with a high current and small transverse size ($\leq 200\ \mu m$). In order to prevent local liquid target boiling or solid target melting, a fast raster system was designed to increase the effective size of the beam spot which will decrease damage done to the target in Hall C.

The fast raster system is located about 25 m upstream of the target along the beamline. It consists of two sets of steering magnets for which one set rasters the beam horizontally and the other set rasters the beam vertically. The current steering the magnets varied sinusoidally to prevent the beam motion from forming a stable figure on the target. The typical raster size in **E91-016** was ±0.5 mm in both the horizontal and vertical direction to form a 1 mm x 1 mm square. The average intensity was greatest along the edges of the square due to the sinusoidal

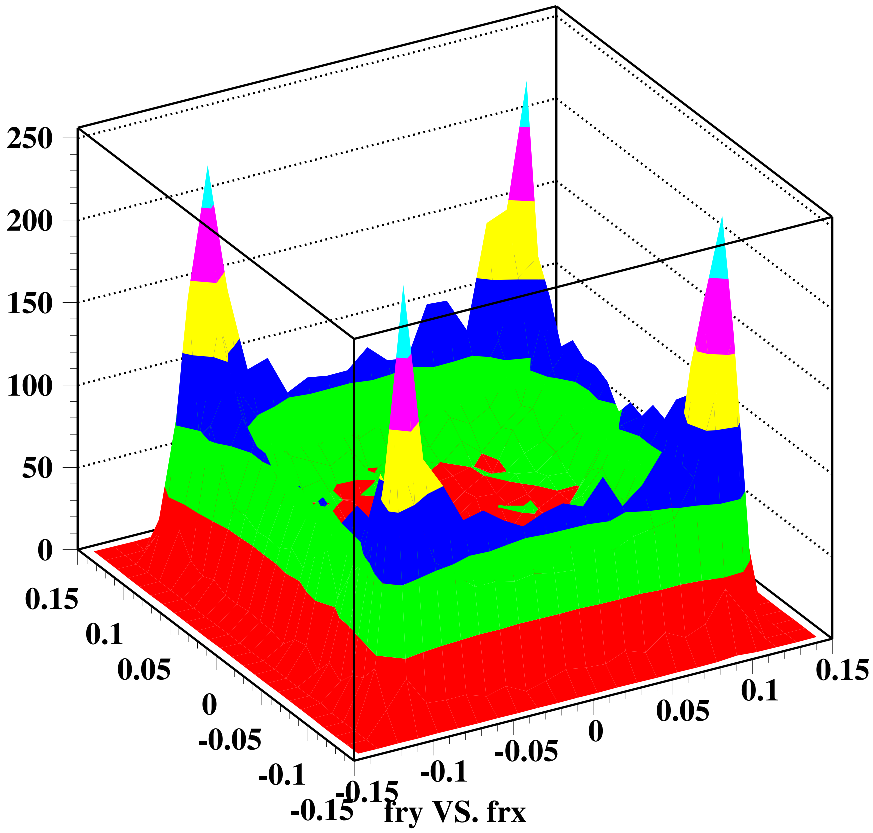

Figure 2.3: Beam profile with fast raster.

rastering, but the reduction in power density was enough to prevent localized target boiling. Figure 2.3 shows the beam profile with the fast raster in use [18].

The slow raster, or dump raster, is located upstream of the target just before the scattering chamber. This raster is used to protect the beam dump, but the current in **E91-016** was never above 80 μA , so it was not used.

2.4 Target

The target assembly for Hall C consists of a cryogenic and solid target ladder contained in an evacuated, cylindrical scattering chamber located at the spectrometer pivot. A schematic of the target ladder is shown in Figure 2.4. The purpose of the scattering chamber is to mechanically and thermally protect the target assembly. Each target ladder is remotely controlled to allow vertical and horizontal movement such that the desired target is positioned in the beam path.

The cryotarget ladder has a set of three loops through which the cooled liquid target cryogens flow. Each loop has a 4 cm target cell, a circulation fan, a heat exchanger, a high power heater, and a low power heater. The target cells are aluminum and cylindrical in shape with its length along the direction of the beam. The target cells in this experiment were referred to as *tuna cans.* The diameter of the target cell is 4.016 cm with an average wall thickness of 0.0121 cm. The fan forces the liquid to flow through the target cell. The high power heaters are used to maintain a constant heat load such that the cooling power would decrease when the beam is on target and increase when the beam is not on target. For **E91-016**, liquid deuterium was in loop 1, liquid hydrogen was in loop 3 , and liquid helium-3 (helium-4) in loop 3. Because all three loops were not operational at the same time (due to mechanical failures), down time was required to switch from the hydrogen target to the helium targets. This required the warm-up of the present target, evacuating the loop, and cooling down the next target. The only exception to this

Target	Temperature (K)	Density (g/cm^3)	Length (cm)
Hydrogen	19.0 ±0.05	0.0723	4.00
Deuterium	22.0 ±0.05	0.16708	4.00
Helium-3	5.5 ±0.01	0.0773	4.00
Helium-4	5.5 ±0.01	0.1364	4.00

Table 2.1: Cryogenic target properties.

case was having liquid deuterium and hydrogen cooled simultaneously towards the end of the running period. The cryotarget ladder also has a pair of dummy cells which consists of two flat aluminum targets separated by the same distance as the length of the target cells. These aluminum targets were used to measure the contribution from the target cell wall and approximately ten times thicker than the actual target cell wall [19] [20].

The hydrogen and deuterium targets were cooled through heat exchange with 15 K helium gas provided by the CEBAF End Station Refrigerator (ESR). The nominal temperature and pressure for hydrogen was 19 K and 24 psi, 22 K and 20 psi for deuterium, and 5.5 K and 133 psi for helium. The average density for the helium-3 target was 0.0773 g/cm^3 and 0.136 g/cm^3 for the helium-4 target. The target temperatures were stable to better than 1% while local density fluctuations were minimized by beam rastering. Table 2.1 lists some properties of the cryogenic targets used in this experiment.

The solid targets that were used during **E91-016** were the carbon, CH2, and quintar. These targets were used for spectrometer checkout and calibration purposes. The carbon target was used for optics studies in sieve slit runs.

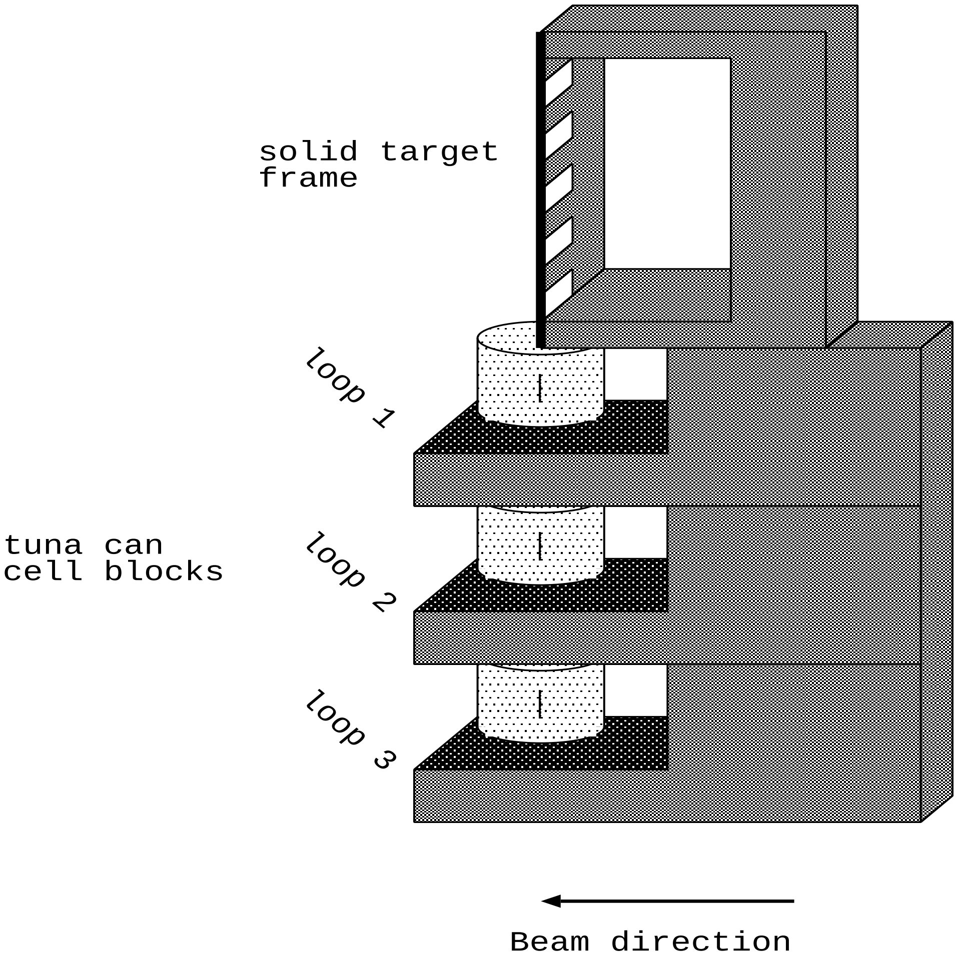

Figure 2.4: Schematic of Hall C cryotarget ladder.

2.5 The Hall C Spectrometers

The standard detector packages in Hall C at Jefferson Lab consist of two magnetic spectrometers which were used for this coincidence experiment. The High Momentum Spectrometer (HMS) was used to detect the scattered electrons and pions while the Short Orbit Spectrometer (SOS) was used to detect the scattered kaons, pions, and protons in coincidence. Both spectrometers have a large solid angle and momentum acceptance with the HMS capable of analyzing particles with a momentum up to 7.6 GeV/c, and the SOS having a maximum central momentum of 1.7 GeV/c. The momentum bite, Δp/p, of the HMS is $\pm$10 %, while the SOS has a larger momentum bite of $\pm$20 %.

2.5.1 High Momentum Spectrometer

The HMS is a superconducting spectrometer with a $Q\bar{Q}QD$ configuration and a 25^0 vertical bend. The magnets and the detector frame are supported on a common carriage which rotates around a rigidly mounted central bearing, thus fixing the detector frame with respect to the optical axis. In order to distribute the weight, the shielding hut which protects the detector hut is supported by a different carriage. A side view of the HMS is shown in Figure 2.5.

The HMS was operated in its standard operating mode of point-to-point focusing in the dispersive and non-dispersive directions. This tune allowed for a large momentum acceptance, solid angle, and extended target acceptance. In this

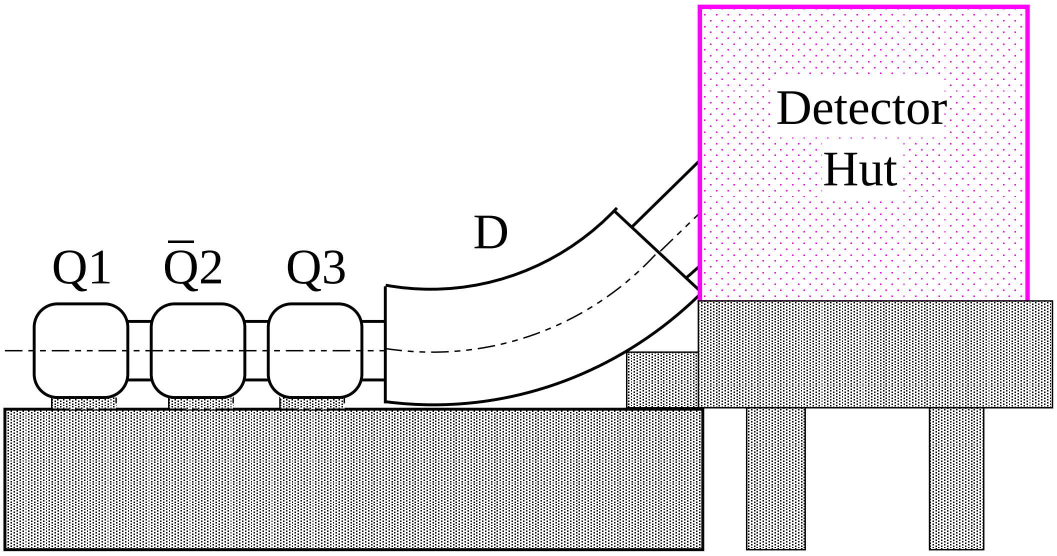

Figure 2.5: Side view of the High Momentum Spectrometer.

tune, Q1 and Q3 focus in the dispersive direction and Q2 focuses in the transverse direction. This means that an event originating from a point target would be focused to a point at the focal plane of the spectrometer. Data was taken with an octagonal collimator placed before the entrances of the spectrometer. This aperture was designed to limit the solid angle acceptance to 6.8 msr and to keep losses within the spectrometer low for a point target. The octagonal collimator was replaced by a set of sieve slits for optics studies. This system is an array of small holes used to compare focal plane distributions to data with known angular distributions. There are two holes missing in order to verify left-right and top-bottom reconstruction. Table 2.2 summarizes the nominal performance parameters of the HMS.

Maximum central momentum	7.4 GeV / c
Momentum acceptance	± 10 %
Momentum resolution [δp/p]	< 0.1 %
Solid angle (no collimator)	> 6 msr
In-plane angular acceptance	$\pm$ 32 mr
Out-of-plane angular acceptance	$\pm$ 85 mr
In-plane angular reconstruction	0.4 mr
Out-of-plane angular reconstruction	0.9 mr
Extended target acceptance	10 cm
Horizontal vertex reconstruction	2 - 3 mm
Momentum setting flexibility	0.5 $\Rightarrow$ 7.4 GeV / c
Angle setting flexibility	$10.50^0 \Rightarrow$ ˜ $90^{\ 0}$

Table 2.2: Summary of the HMS Performance.

2.5.2 Short Orbit Spectrometer

The SOS is a $QD\bar{D}$ design based upon the Medium Resolution Spectrometer (MRS) at LAMPF. The magnets are water cooled and powered by three separate InverPower power supplies which can be remotely controlled from the control room. The power supplies can reverse the output polarity, which allowed for detecting both positively and negatively charged particles. The magnets and the detector hut rest on a common carriage assembly, and the dipoles share a common yoke. The SOS is designed to be compact in order to allow detection of short lived particles such as kaons and low momentum pions. A side view of the SOS is shown in Figure 2.6.

For this experiment, the SOS was operated in the standard point-to-point tune with the quadrupole focusing in the non-dispersive direction followed by the two dipoles which bend the beam up 33^o and then down 15^o . This tune has a large solid angle acceptance and momentum bite, but a small extended target

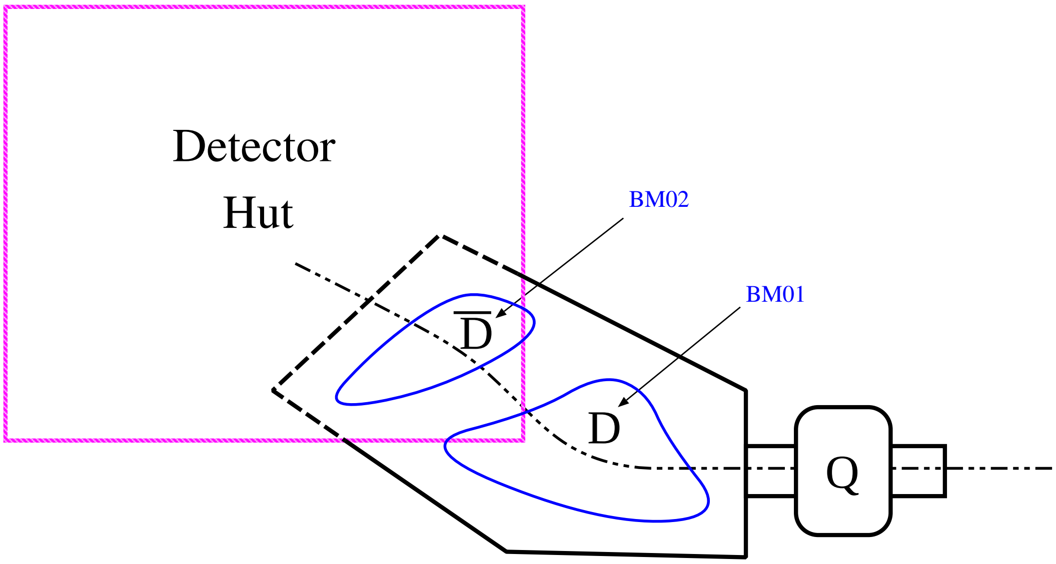

Figure 2.6: Side view of the Short Orbit Spectrometer.

acceptance. Similar to the HMS, a slit system consisting of three collimators was installed in front of the SOS quadrupole to allow remote insertion of the various collimators. The first is a sieve slit used for optics studies. The other two, named *large* and *small*, are octagonally designed to limit the solid angle acceptance. For this data, the large collimator was used, which limited the solid angle acceptance to 7.55 msr and limited the losses within the spectrometer for a point target. Table 2.3 summarizes the SOS nominal performance.

2.6 Detector Package

The standard HMS and SOS detector packages are nearly identical in that each has a pair of drift chambers, two sets of x-y hodoscopes, a gas Čerenkov detector, and a lead glass shower counter detector. For **E91-016**, the SOS also

Maximum central momentum	1.70 GeV / c
Momentum acceptance	±20 %
Momentum resolution [δp/p]	< 0.1 %
Solid angle (no collimator)	˜ 9 msr
In-plane angular acceptance	±70 mr
Out-of-plane angular acceptance	±40 mr
In-plane angular reconstruction	0.5 mr
Out-of-plane angular reconstruction	1.0 mr
Extended target acceptance	4 cm
Horizontal vertex reconstruction	2 - 3 mm
Momentum setting flexibility	0.1 ⇒ 1.7 GeV / c
Angle setting flexibility	$13.3^0 \Rightarrow$ ˜$169.4\ ^0$

Table 2.3: Summary of the SOS performance

had an aerogel Čerenkov detector between the last two scintillator planes and a lucite Čerenkov detector placed in front of the third scintillator plane. The hodoscope scintillators were used to form the primary trigger and provide time-of-flight information. The drift chambers provided tracking information. The shower counter and Čerenkov detectors were used for particle identification in the trigger and offline analysis. The layout of the detector packages are nearly identical, except the SOS detector package is more compact. Schematic diagrams of both the HMS and SOS detector packages are shown in Figure 2.7 and Figure 2.8.

2.6.1 Drift Chambers

Particles entering the detector hut first encounter the pair of drift chambers. The HMS chambers were designed and built at Jefferson Lab by a Hampton University group. The chambers consist of six wire planes with multiple orientations. Two planes measure x (dispersive direction), two measure y (non-dispersive

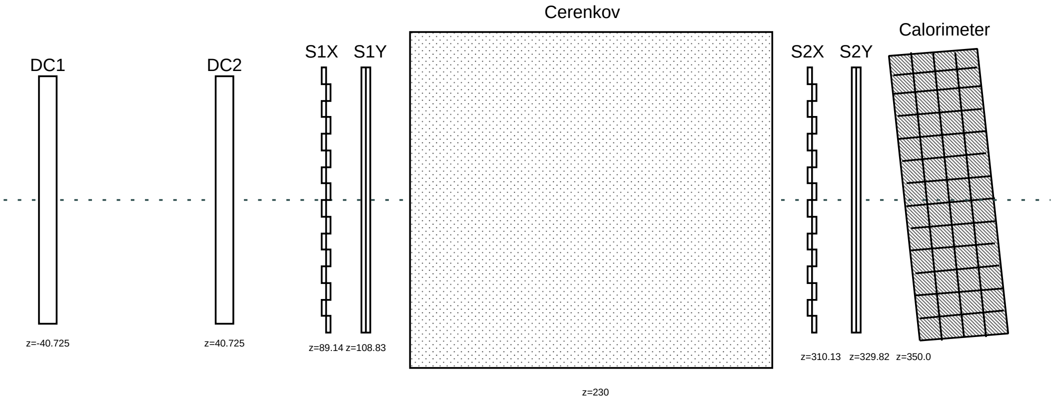

Figure 2.7: HMS detector hut

direction), and two stereo planes that were rotated by ± 15^o with respect to the x planes. As seen by incoming particles, the planes were ordered *x, y, u, v, y', x'*. Each chamber has a large active area of approximately 107x52 cm^2. The planes were spaced by 1.8 cm while the chambers were separated by $\sim$ 80 cm. Figure 2.9 shows the side view of the HMS and the SOS drift chambers.

Each plane contains alternating 25 μm diameter gold-plated tungsten sense wires and 200 μm gold-plated copper beryllium field wires. Each plane is separated by 200 μm copper beryllium guard wires. The basic HMS drift chamber cell is a rectangular lattice with the sense wire in the center surrounded by eight field wires. The chambers (both HMS and SOS) are filled with a 50:50 argon-ethane mixture. When a charged particle passes through the chamber, the gas will ionize, and the liberated electrons will move to the nearest sense wire by the voltage differential maintained by the chamber. By detecting which sense wire collected the charge,

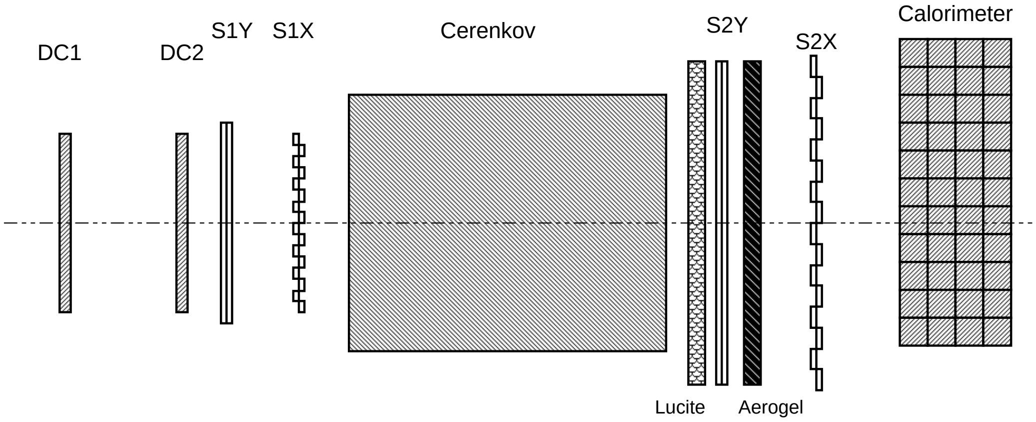

Figure 2.8: SOS detector hut.

the position can be measured within an accuracy of 0.5 cm, which is half the size of the cell. The drift distance can be extrapolated from the drift time which is measured by taking the time difference between the passage of the charged particle and the signal on the wire. This information was collected by Fastbus Time-to-Digital Converters (TDC). By measuring the position with the six planes, the trajectory of the particle through the chamber can be measured. More details on the HMS drift chambers can be found in [6].

The SOS drift chambers were constructed at Brookhaven National Laboratory. Two chambers, DC1 and DC2, were placed in front of the detector package. Each chamber consists of six wire planes with x and x' measuring the position in the dispersive direction, and the u/u' and v/v' rotated 60^0 clockwise and counterclockwise, respectively. As in the case of the HMS chambers, the x', u', and v' planes are offset by a half cell from the x, u, and v planes in order to resolve the

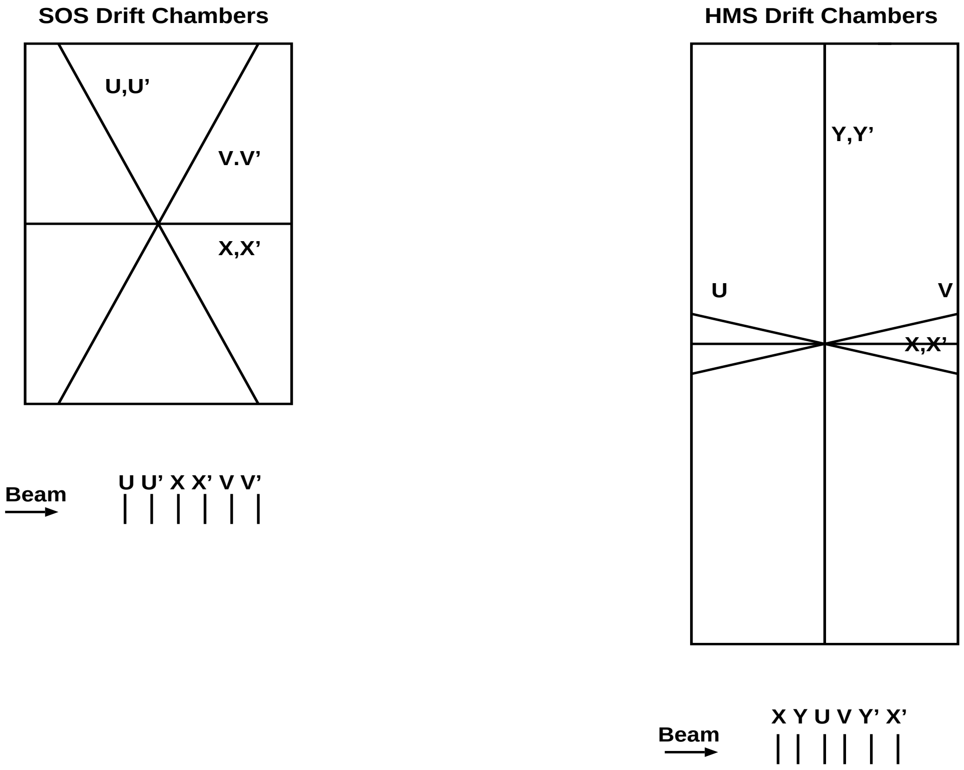

Figure 2.9: Side view of drift chambers.

left-right ambiguity. Each chamber is composed of sixteen layers of 1/8 inch G10 plates sandwiched between two 1/2 inch Al plates. The G10 plates holding the cathode foils were mounted alternatively to the plates that hold the sense and field wires. The field wires alternate with the sense wires, which were separated by 1 cm within the plane. A large positive high voltage is maintained on the cathode foils and the field wires to provide the field for the sense wires. The wire positions were measured during construction and matched the expected design values within ±87 μm accuracy limits. The drift time is converted to drift distance and added to the wire position in to determine the position of the event.

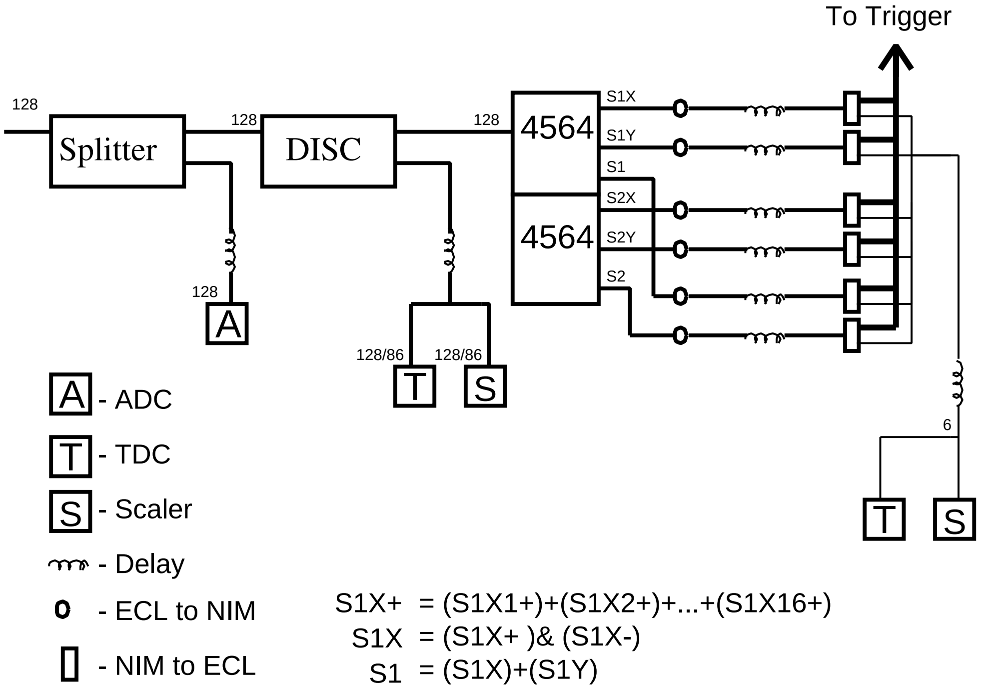

Figure 2.10: Hodoscope electronics for the HMS/SOS.

2.6.2 Hodoscopes

Both the HMS and SOS detector stacks have two pairs of x-y hodoscopes separated by approximately 2 m. The purpose of the scintillator hodoscopes was to provide the primary trigger as well as particle identification through time-of-flight information. The hodoscope paddles are long narrow strips of 1 cm thick BC404 scintillator with UVT lucite light guides. The signal from the scintillators are read out by two Philips XP2282B photomultiplier tubes. These PMT's are 8-stage tubes with nominal operation at 2500 volts. Because of variations in gain in each PMT, individual high voltages had to be adjusted to balance the gains, which do not normally need to be readjusted. Timing calibrations of the scintillators were done using data during the running, and the “time walk” corrections (due to pulse height variations) were done using an offline fitting procedure [21] [22]. The hodoscope elements in the HMS and SOS were identical except for the size and number of elements. The HMS elements are wrapped with one layer of aluminum foil and two layers of tedlar to make them light tight. The scintillators have a 0.5 cm overlap between paddles to avoid gaps. All of the HMS elements are 8.0 cm wide. The front and back x planes (S1X and S2X) have 16 elements which are 75.5 cm long. The front and back y planes (S1Y and S2Y) have 10 elements each which are 120.5 cm long. The SOS elements are wrapped with one layer of aluminized mylar followed by two layers of tedlar. In the SOS, the front hodoscope pair is smaller than the rear pair. The front x plane has 9 elements which are 7.5 cm wide and 36.5 cm long. The front y plane also has 9 elements which are 4.5 cm wide and 63.5 cm long. The back x plane has 16 elements, each 7.5 cm wide and 36.5 cm long. The back y plane has 9 elements, each 4.5 cm in width and 112.5 cm in length. The total active area for the HMS is 120.5 x 75.5 cm^2, and 112.5 x 36.5 cm^2 for the SOS.

The output from the tubes is sent from a patch panel in the detector hut to the counting house through approximately 450 feet of RG8 cable. From there, the signals are sent through a splitter, giving two signals with 1/3 and 2/3 of the amplitude of the original signal. The smaller signal is put through $\sim$ 400 ns of delay cable to Analog-to-Digital Converters (ADC) to measure the integral of the signal. The other output signal goes to discriminators, with one set going through logic delay modules to TDC's and VME scalers. The other output from the discriminators is sent to a LeCroy 4654 logic module to generate the OR of all tubes on one side of a given plane. The trigger logic used the AND of the sets of tubes on each side of a plane (e.g., S1X = S1X+ & S1X-) as well as the OR of the front (and back) pairs of planes (e.g., S1 = S1X + S1Y). The hodoscope electronics are shown in Figure 2.10 [23].

2.6.3 HMS and SOS Čerenkovs

For improved particle identification, both the HMS and SOS have threshold gas Čerenkov detectors located between the front and back pairs of the hodoscopes. In addition, the SOS had an aerogel Čerenkov detector inserted between the X and Y planes of the rear pair of hodoscopes and a lucite Čerenkov in front of the third scintillator plane. The detector works by detecting the Čerenkov radiation emitted by particles when they move through a medium with an index of refraction, n, at velocities greater than the speed of light in that medium. Charged particles moving above the speed of light in this medium will emit light in a forward pointing cone. By properly choosing the index of refraction, a threshold velocity can be set such that only certain particles will emit Čerenkov radiation. The electronics for the Čerenkov detectors are shown in Figure 2.11.

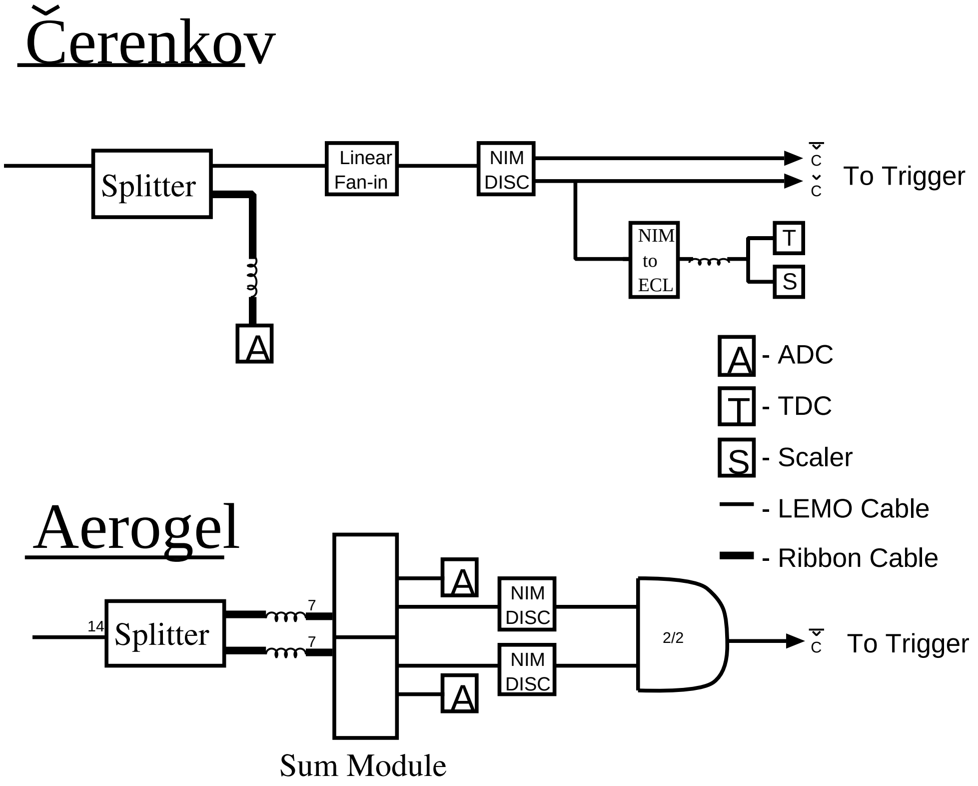

Figure 2.11: Electronics for the HMS and SOS Čerenkov detectors.

Gas Čerenkov Counters

The HMS gas Čerenkov detector is a large cylindrical tank approximately 152 cm in length and 150 cm in diameter designed by the University of Virginia. The detector contains two mirrors which focus light onto two 5 inch Burle 8854 photomultiplier tubes and has 0.04 inch thick aluminum windows covering the circular ends of the cylindrical tank. The gas handling system for the tank is designed for it to operate at low atmospheric pressures. For this experiment, the detector was filled with CO_2 at 1 atmosphere. This yielded a pion threshold of

4.9 GeV/c and an electron threshold of 17.9 MeV/c averaging 9 photoelectrons. Because the HMS gas Čerenkov was in an "OR logic" trigger with the shower counter detector, the high voltages were adjusted so that each tube gave the same signal within 10%.

The SOS Čerenkov, designed and built at the University of Colorado, is a nearly rectangular aluminum box, 99 cm high, 73.7 cm wide, and 111 cm long. The walls are 1.3 cm thick, and the entrance and exit windows are composed of one layer of 0.254 mm lexan graphics film and one layer of 0.05 mm tedlar film. The box has four ports for Burle 5-inch 8854 photomultiplier tubes. Because there was no need to distinguish between between pions and positrons for this experiment, the SOS gas Čerenkov was not used.

SOS Aerogel Čerenkov

In order to separate a clean sample of kaons from the large background of pions and protons, a silica aerogel Čerenkov detector was installed as part of the standard SOS detector package. Although p/K^+separation was easily achieved via TOF measurements, $\pi^+/K^+$was not possible due to the resolution of the TOF measurements. The index of refraction of the silica aerogel was 1.034 ± 0.001. With this index of refraction, pions had a threshold of about 520 MeV/c and a kaon threshold of about 1800 MeV/c. Therefore, pions (and positrons) would create Čerenkov photons, but kaons and protons would not create Čerenkov photons.

The aerogel material (n(SiO_2)+2n(H_2O)) is a 9 cm thick slab cut and arranged into three layers (slightly staggered to avoid cracks) of 25x25x3 cm^3. This entire block was wrapped in one layer of Millipore paper ($\sim$ 97% reflection) and two layers of aluminized Mylar, except the side facing the diffusion box. The block was placed, uncovered side up, in an aluminum tray and held in place by thin steel brackets along the sides and thin wires strung across the top. The diffusion box was inverted on the open face of the silicon tray. All of the remaining internal surfaces were covered with two layers of Millipore paper. The entire box was then bolted shut and sealed with teflon and electrical tape to be light-tight and reasonably air-tight. Complete details can be found in [24]. Because the aerogel material is hygroscopic, the detector was flushed continuously with nitrogen through gas feedthroughs located on the diffusion box to avoid moisture from the air contaminating the material.

After the first kaon electroproduction experiments were completed in 1996, the aerogel detector was removed and stored in a wooden box on-site. Since the wooden box could not prevent the material from absorbing moisture over a period of three years, the tray of aerogel was placed in a convection oven and heated for 48 hours to remove water. Even though this process removed the moisture from the aerogel, the Millipore paper probably lost some reflectivity due to discoloration during the baking. The average photoelectron yield dropped significantly from 16 photoelectrons in 1996 to 12 photoelectrons in 1999.

On each side of the diffusion box were seven circular ports which held the 5-inch Burle 8854 photomultiplier tubes. The fourteen signals from the detector were sent through a splitter in the counting house, similar to that of the hodoscopes. The larger signals were sent to ADCs, and the smaller signals were used to build an aerogel pretrigger for hardware pion rejection. The fourteen signals were amplified and summed to form two combined signals, A and B. Each of the sums was sent to a discriminator programmed to a threshold of 3 photoelectrons. Both signals must have been above the discriminator threshold to be sent to the SOS pretrigger logic as a veto signal. A schematic of the aerogel detector is shown in Figure 2.12.

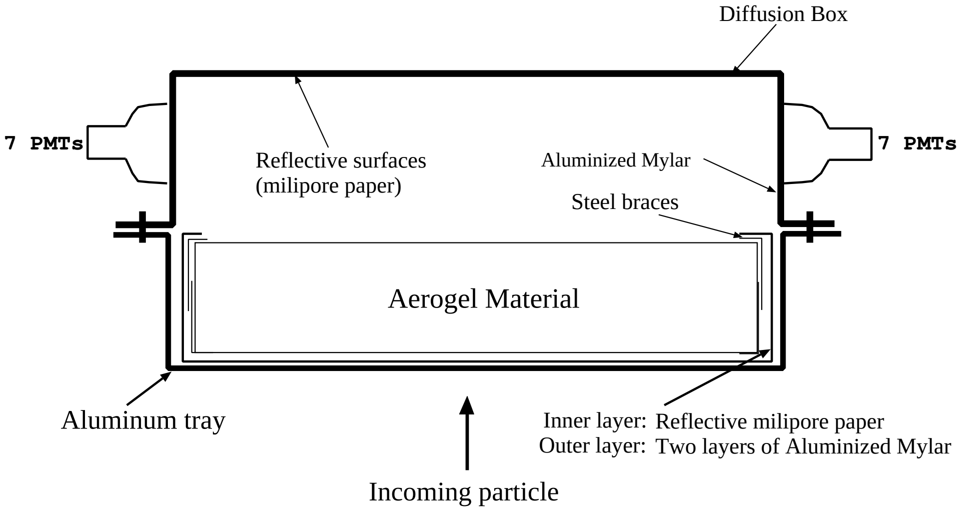

Figure 2.12: Cross section of the SOS aerogel Čerenkov detector.

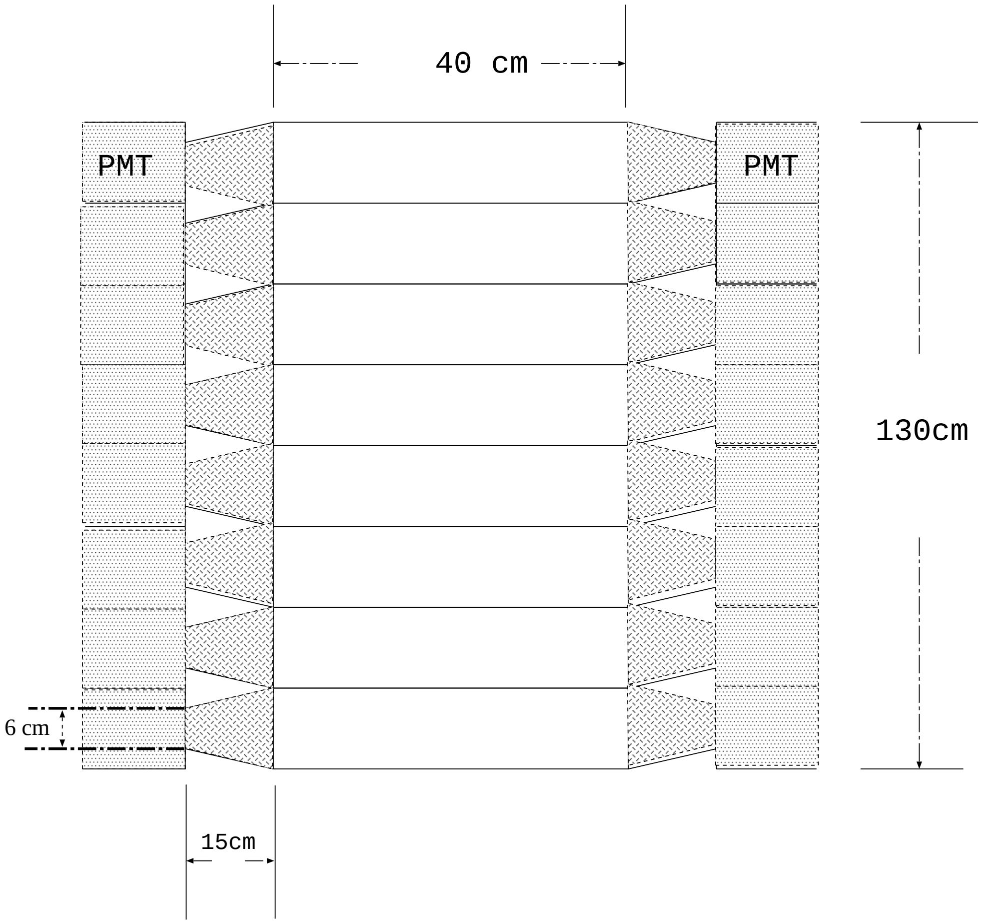

Figure 2.13: Front view of the SOS lucite Čerenkov detector.

Lucite Čerenkov

The lucite Čerenkov detector is a threshold detector used to discriminate between $p^+$and K^+. Figure 2.13 shows a schematic of the detector [9]. The TOF measurements provide clean particle separation, but the lucite detector was additionally used in the online trigger for nearly half of the experiment running time. The angle of the Čerenkov radiation cone depends on the index of refraction of the medium and the velocity of the particle. The index of refraction of the lucite was 1.49, so the threshold velocity was 0.672 (v/c). For the SOS momentum of 1.290 GeV/c during **E91-016**, the protons have a mean $\beta = 0.830$ and will emit Čerenkov light. By including the principle of total internal reflection, TIR, the threshold of detected radiation is increased. The incident radiation angle must be greater than the critical angle to have TIR, otherwise the light will be transmitted out of the material. With the inclusion of TIR, the $\beta_{threshold}$ is raised to 0.905, therefore the detector is able to discriminate between protons and kaons.

The lucite detector was designed and built jointly by the Hampton University and Temple University groups. It consists of eight individual ultra-violet transmitting lucite bars with dimensions of 40x13.7x2.5 cm wrapped in black teflon foil. Each end of a bar has a 15 cm light guide tapered on end to fit the 3-inch Philips photomultiplier tube. The detector was mounted on a metal frame in the SOS detector hut which was attached to the S2Y hodoscope frame. Each signal from the PMT was amplified above noise and gain matched by adjusting the high voltage. The signal was split such that 1/3 of the signal went to an ADC and the remaining to a summing module. The 16 signals were summed and sent to a discriminator so that a summed signal above 3 photoelectrons meant the event was accepted. To prevent throwing out good K^+events, the coincidence between the left and right PMT was not required. From the discriminator, the signal was sent to trigger logic and outputs for TDCs [9].

2.6.4 Lead Glass Calorimeter

For further e/π^- separation, both the HMS and SOS have lead-glass calorimeters (shower counters) installed at the rear of the detector stacks. The shower counters are constructed from 10x10x70 cm of TF1 lead glass blocks. The blocks are stacked transversely to the incoming particles, four layers deep. Each layer is 13 blocks high in the HMS (11 in the SOS). Both calorimeters are rotated 5^0 from the optical axis to avoid loss through the cracks between the modules. The detectors are identical in design and construction except for their total size. The shower counter is an electromagnetic calorimeter that detects the energy deposited when a charged particle transverses the material. High energy electrons interact with matter mainly through Bremsstrahlung radiation and radiate photons. These photons will generate positron-electron pairs which will also radiate photons. The photomultiplier tubes will detect the Čerenkov light given off by this shower of charged particles. The total pathlength of the particles is proportional to the energy of the initial charged particle, so the total Čerenkov light is therefore proportional to the energy of the showering particle. Hadrons (pions) will generally deposit a constant energy per layer while electrons will tend to deposit all of their energy in layer one or two resulting in an energy fraction (ratio of energy detected to the particle momentum) of one.

2.7 Trigger

The signals produced by the HMS and SOS detectors are sent from the detector huts to the counting house to be split in such a way that one signal is sent to ADC while the remaining is sent to TDCs and VME scalars. Since the counting rates were high, some particle selection had to be provided for each spectrometer.

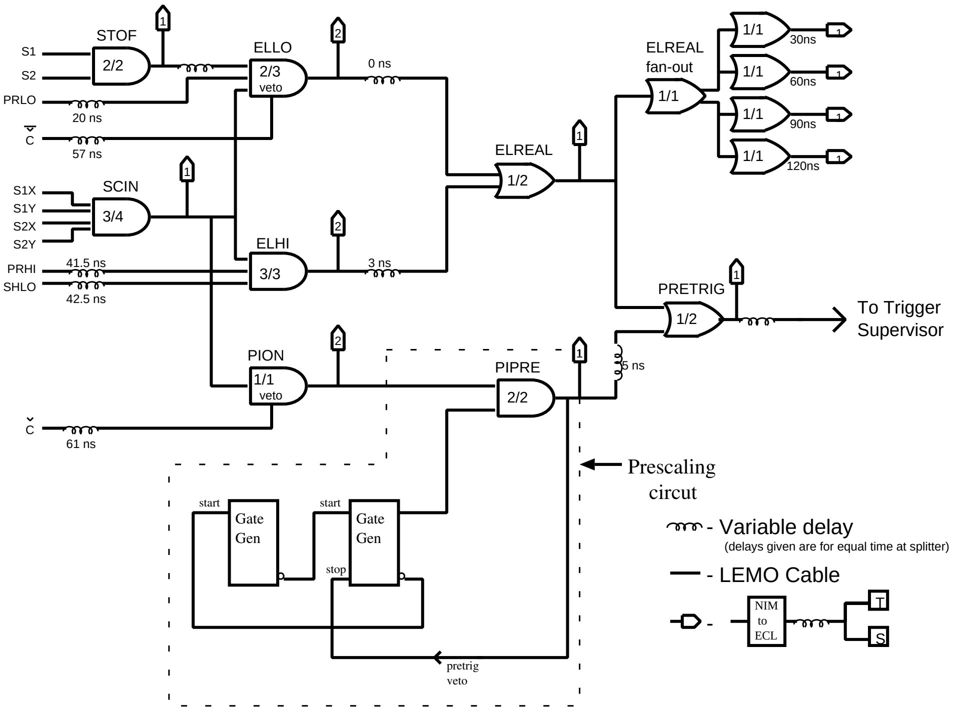

Figure 2.14: HMS single arm electronics.

2.7.1 Spectrometer Trigger

The HMS and SOS have separate trigger electronics providing accepted events for each spectrometer, which are shown in Figure 2.14 and Figure 2.15.

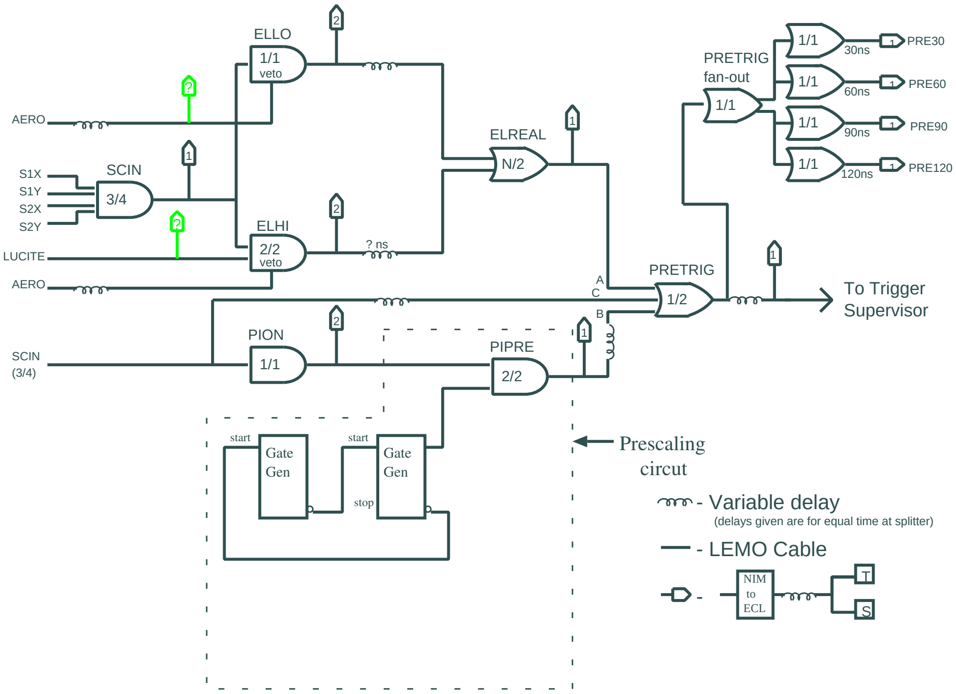

Figure 2.15: SOS single arm electronics.

The hodoscopes provided the first part of the trigger for both spectrometers when a charged particle passed through them. After each end of a paddle was read and discriminated (for each plane), the signals were OR-ed together to create the signals, S1X+, S1X-, S1Y+, S1Y-, S2X+, S2X-, S2Y+, and S2Y-. A hit in a given plane was then defined as a coincidence between the corresponding "plus" and "minus" signals, but not necessarily on the same paddle. The basic trigger is created by 3/4 of S1X, S1Y,S2X, and S2Y (SCIN). For the HMS, a less restrictive trigger, S1 AND S2 (STOF), could also be used. In addition to the hodoscope trigger, the gas Čerenkov counter and calorimeter signals were used to determine whether the charged particle was an electron or pion. An electron was detected if there was a Čerenkov signal or a large shower counter signal. Triggers with no Čerenkov signal were labeled as pions triggers and prescaled to take a sample of pions. Additional logic was used to create the HMS pretrigger from the raw spectrometer trigger which was then sent to the Trigger Supervisor (TS) [23].

The SOS was different in that the detection of kaons required use of the aerogel detector to reject pions. While the hodoscope trigger was basically the same as the HMS, the aerogel detector was inserted in the trigger in a manner analogous to that used in the HMS for pion-electron separation. For higher proton rates (as the case for the helium-4 target), the lucite Čerenkov detector was inserted into the trigger to reject a fraction of protons. A signal from the lucite and an aerogel Čerenkov-veto signal indicated that a kaon was detected. As with the HMS, this raw spectrometer trigger formed the SOS pretrigger for the trigger supervisor.

2.7.2 Trigger Supervisor

The trigger supervisor is the sophisticated electronic hardware which served as the interface between the trigger hardware and the computer data acquisition. A diagram of the electronics is shown in Figure 2.16. It is programmed to accept, reject, or prescale each of the different types of triggers, depending on the experiment. The trigger supervisor makes all the decisions about how to actually process a trigger. When a trigger arrives at the trigger supervisor, it latches all of the enabled trigger types into a data word after a 10 ns delay. The event type

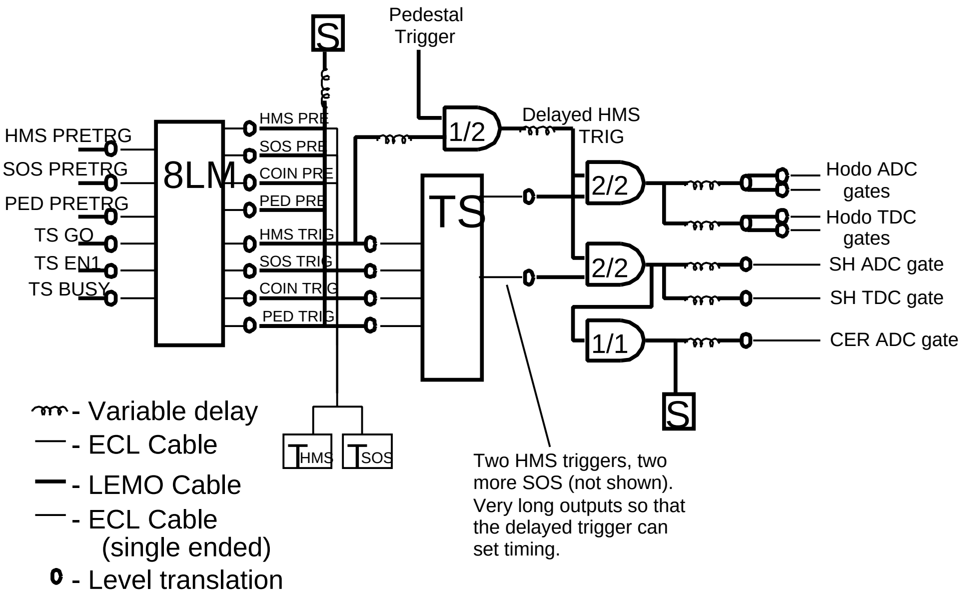

Figure 2.16: Trigger Supervisor electronics.

is determined and the appropriate gate is generated for data readout. The four defined event types are HMS, SOS, COIN, and PED events. In order to measure the pedestal values for the ADCs, a fixed number of events (usually 1000) were generated by a random trigger. Because of high data rates, the sparsification feature of the ADCs and TDCs was used to reduce the event size. In this mode, an output for a channel was not given if there was no stop signal after the common start for the TDCs. For the ADCs, all channels that had a signal smaller than a threshold for that channel were ignored. For that reason, the pedestal events were taken with the data sparsification disabled. The rest of the data for each run were taken with real triggers and sparsification enabled. The data acquisition mode was controlled using the TS status outputs to determine how an event will be processed. While a run is in progress, the TS GO signal is active. The TS EN1 signal indicates that a run is in progress and normal data taking is enabled. The TS BUSY signal is active whenever the TS is busy processing an event.

The control signals of the trigger supervisor and the trigger signals were sent to the 8LM logic module. The 8LM has eight outputs, four of which are used for the HMS, SOS, COIN, and PED pretriggers. Even if the TS was busy, a pretrigger was generated for each incoming pretrigger during the appropriate part of the run. The other four outputs were the HMS, SOS, COIN, and PED triggers. These triggers were sent directly to the TS because they required the TS to have no BUSY signal. After the trigger is fed to the trigger supervisor, it then needs to determine what hardware needs to be read based on the trigger type. Once the appropriate gate has been generated and sent out for data readout, each spectrometer re-times the gate it receives with respect to the single arm trigger for that spectrometer. Because the coincidence trigger has its timing set by the last of the two spectrometers, the ADC gates must come at a fixed time with respect to the time the particle passed through the detector. For this reason, the gates from the TS are then delayed and have their widths fixed so that they are properly timed for use as ADC gates and TDC starts. Table 2.4 shows the programming of the 8LM.

output signal		definition
HMS PRETRG	=	(HMS)&(EN1)
SOS PRETRG	=	(SOS)&(EN1)
COIN PRETRG	=	(COIN)&(EN1)
PED PRETRG	=	(PED)&(GO)&($\overline{EN1}$)
HMS TRG	=	(HMS)&(EN1)&($\overline{BUSY}$)
SOS TRG	=	(SOS)&(EN1)&($\overline{BUSY}$)
COIN TRG	=	(COIN)&(EN1)&($\overline{BUSY}$)
PED TRG	=	(PED)&(GO)&($\overline{EN1}$)&($\overline{BUSY}$)

Table 2.4: 8LM Trigger Logic

2.7.3 Other Signals

All of the intermediate signals were sent to scalers and TDCs which show the signals that were present when the trigger was taken. This allowed for the determination of the event types that formed a particular trigger. All of the scaler information were recorded in the data stream, while a set of visual scalers allowed for quick detection of certain types of electronics problems in the intermediate steps of trigger formation. The scalers were also used to measure computer and electronic dead time.

2.7.4 Data Rates

Due to the high duty factor and current provided by the Jefferson Lab CEBAF machine, there was the potential to have very high raw data rates. The maximum data acquisition rate was limited by the Fastbus conversion time and the data readout time. For basic data acquisition mode, the total time to process an event was just under 1 ms. With this, the data acquisition was limited to approximately 1.1 kHz, but gave large computer dead times at even lower rates. Improvements have been made to improve the data rate and decrease the dead time, such as the optimization of the Fastbus readout and the utilization of the multi-block read features of the ADCs. These improvements reduced the total processing time to 400 μs and doubled the coincidence trigger rate limit to 2 kHz.

2.8 Data Acquisition

The CEBAF Online Data Acquisition (CODA) system is the standard data acquisition component of the experimental equipment of Hall C. The conversion from a collection of electronic signals to a physics event written to disk is managed by the CODA system. The data files for the runs contained both event information and slow controls readout, which are read out separately.

2.8.1 CODA - Physics Events

CODA controls the several pieces of the data acquisition in Hall C. It provides the user interface and determines how to handle triggers from the trigger supervisor. CODA also includes a graphical user interface (RunControl) which allows the user to start and stop runs, as well as define run parameters. Information for each event is temporarily stored in TDCs and ADCs, which are housed in Fastbus and VME crates. The trigger supervisor controls the state of the run, and generates the triggers which cause the data to be read out from the Read-Out

Controllers (ROCs). One of the main two components of CODA, the Event Builder (EB), reads and combines the data fragments from the ROCs to build an event with the necessary header information into an event file. The EB also checks the synchronization of the data stream where fragments for every 1000 events are read at a time. If synchronization has been lost within the 1000 events, the EB resets it. The data can also be sent through the other main subsystem of CODA, the Event Analyzer (ANA). In this system, the data is allowed to be full or partially analyzed or preprocessed before the events are written to tape. Because this data analysis process was relatively time-consuming, the default analysis was an empty/dummy subroutine. To improve performance, the EB and the ANA were combined into one program. For this experiment, the spectrometers provided independent triggers and the physics events contained only data for the associated spectrometer. Beam related quantities, such as beam position monitors, beam loss monitors, and beam raster readback values, were read out and recorded on an event-by-event basis.

2.8.2 EPICS - Slow Controls

Other user event types can be defined in CODA, which allows readout of hardware scalers or execution of user scripts. The HMS, SOS, and oincidence hardware scalers were read by an asynchronous process every two seconds. A script was triggered by CODA every 30 seconds to read the detector controls, beamline

Set	E_e (GeV)	$p_{e'}$ (GeV/c)	p_{K^+} (GeV/c)	$\theta_{e'}$ Deg	θ_{K^+} Deg	Q^2 (GeV^2)	W (GeV)	-t (GeV^2)
1	3.245	1.576	1.290	15.00	13.33	0.349	1.914	0.156
2	3.245	1.576	1.290	15.00	19.33	0.349	1.914	0.191
3	3.245	1.576	1.290	15.00	25.33	0.349	1.914	0.284

Table 2.5: Nominal kinematics for E91-016 angular distribution.

controls, and readouts not directly associated with data acquisition. These various slow control variables from the Jefferson Lab EPICS database were sent into the Hall C data stream. Jefferson Lab also uses an EPICS database as the interface to the accelerator and various Hall C instrumentation, such as spectrometer magnet settings, accelerator settings, and target status variables. A separate process was used to log target and magnet status information.

2.9 Kinematics

The kinematics for **E91-016** are listed in Table 2.5. Data were obtained on hydrogen, helium-3, and helium-4 for each setting. Each kinematic value is the mean of the kinematic variable for Λ production.

CHAPTER 3

DATA ANALYSIS

3.1 Engine

The raw data files were analyzed using the standard Hall C event reconstruction software written in FORTRAN, called ENGINE. This program has interfaces with CODA and CERN's CERNLIB/GEANT libraries. The CEBAF Test Package (CTP), which was written at Jefferson Lab in C, provides a flexible way to store and modify histograms, tests, and scaler definitions. This code, which was modeled loosely on the LAMPF Q system, read and parsed the input parameters and flags at the beginning of the analysis [25]. Results from detector calibrations were stored in ASCII files and taken as input to the ENGINE software. ENGINE reads the raw events, decodes the detector hits, and generates tracks and particle identification information. The data is output into report files, PAW HBOOK files, and PAW Ntuple files [26]. Report files contain the hardware and software scalers, information about the detector efficiencies, dead time corrections, beam line information, and charge. The HBOOK files contain a standard set of histograms which are used to monitor detector performance and hardware during a run. The Ntuple files contain event-by-event information for the offline physics analysis [22].

3.2 Tracking

Once the hodoscope information has been decoded and timing corrections applied, the information from the other detectors was decoded. The track independent quantities, such as calorimeter energy, were then calculated, and the tracking routine called. The information from the drift chambers is used to measure the trajectories of the events at the focal plane. Before tracking is attempted, at least 5 out of the 6 wire planes for each chamber must have had a hit. Once a wire has fired, the position of the wire is known and the drift time is determined. The drift time is determined by measuring the difference between the hodoscope start time (the time that the particle passed through the focal plane) and the time at which the wire detected the particle. Knowing the drift time and the drift velocity of the electron-ion pairs in the gas mixture used in the chamber provided the means to calculate the distance from the wire at which the event occurred. It is assumed that the particle is moving nearly perpendicular to the plane. Corrections are applied to compensate for the time required for the signal to propagate along the wire and differences in cable lengths from the chamber to the TDCs.

With the drift distance determined, space points were defined for each hit wire and linked between planes to form stubs. These are tracks determined by just using the hits in the first chamber. However, for each hit wire, the event could have occurred on the left or right of the wire. With this, reconstructing a track was a matter of fitting each combination (2^6 possibilities) and choosing the stub

Quantity	Applied Offset
hsdelta	no offset
hsxptar	no offset
hsyptar	hsyptar + 0.001
ssdelta	(ssdelta+0.0)-ssxptar×1.5
ssxptar	ssxptar - 0.001
ssyptar	no offset

Table 3.1: Offset and modification for matrix reconstructed quantities.

with the lowest χ^2. To improve the speed of the tracking algorithm, the small angle approximation was used to take advantage of the fact that planes measuring the same coordinate of a track are staggered by half a cell. This was used for the y and y' planes in the HMS and all of the planes in the SOS. The x planes in the HMS were too far apart and the stereo planes are not parallel. If there is a hit in both planes, one can choose the left-right combination that makes the particle go between the wires. Using this approximation, the possible left-right combinations are reduced to 2^4 in the HMS and no left-right ambiguity in the SOS. After all the space points have been found and stubs fit for each one in the front chamber, the same procedure is done for the second chamber. The final part of the tracking algorithm checks the consistency for each combination of stubs between the front and back chamber. A full track is fit if the two stubs were consistent, and the χ^2 is recorded. There are typically 1-2% events with multiple tracks. The track with the lowest χ^2 is chosen as the best track. This final track is projected to the focal plane [23].

Using the known optics properties of the spectrometer, the track was then propagated back through the spectrometer to the target by way of the transport matrix to reconstruct the momentum, slopes (x' and y'), and y at the target. The transport matrix was initially determined by the COSY INFINITY model transport code. The SOS matrix reconstruction elements distributed by K.A. Assamagan in October 97 were used [27]. The matrix elements were fine-tuned by taking calibration data with a sieve slit between the spectrometer and target. A thin carbon target was used to take the optics calibration data. The first order offset components for each reconstruction element are shown in Table 3.1.

3.3 Particle Identification

The preliminary step in analyzing the **E91-016** data is to select a clean sample of kaons which are coincident with scattered electrons. Loose cuts on the aerogel and lucite Čerenkov detectors were used to reject some pions and protons in the trigger. The detector packages in the HMS and SOS allowed for a clean sample of kaons and electrons when operating within the design specifications. The good timing resolution of the scintillator hodoscopes provided fairly clean separations between kaons, pions, and protons. The efficiencies of the cuts had to be calculated in order to correct for the number of real kaons that were lost.

Acceptance cuts for both data and SIMC		
$\lvert hsdelta \rvert$	$<$	8. (%)
$\lvert hsxptar \rvert$	$<$	0.075 (rad)
$\lvert hsyptar \rvert$	$<$	0.035 (rad)
$\lvert ssdelta \rvert$	$<$	15. (%)
$\lvert ssxptar \rvert$	$<$	0.035 (rad)
$\lvert ssyptar \rvert$	$<$	0.075 (rad)
PID cuts only for data		
$\lvert cointime - 0.06 \rvert$	$<$	1.00 (ns) ; coincidence time cut for real events
$\lvert \beta - \beta_p \rvert$	$<$	0.045 ; SOS beta
saernpe	$<$	1.7 ; number of aerogel Čerenkov photoelectron
hcernpe	$>$	2. ; number of HMS Čerenkov photoelectron
hsshtrk	$>$	0.70 ; energy deposition in HMS shower counter

Table 3.2: All cuts summary table for kaon production data and SIMC.

3.3.1 Tracking Cuts

The event reconstruction code generates information for the good tracks at the focal plane and the reconstructed tracks at the target. Loose cuts were applied on the reconstructed target quantities to eliminate events which were outside of the spectrometer acceptance, but still got detected at the detector hut. There was also a cut applied on the reconstructed momentum to analyze data within the momentum region of the spectrometer where the matrix elements are well understood. The tracking cuts are listed in Table 3.2.

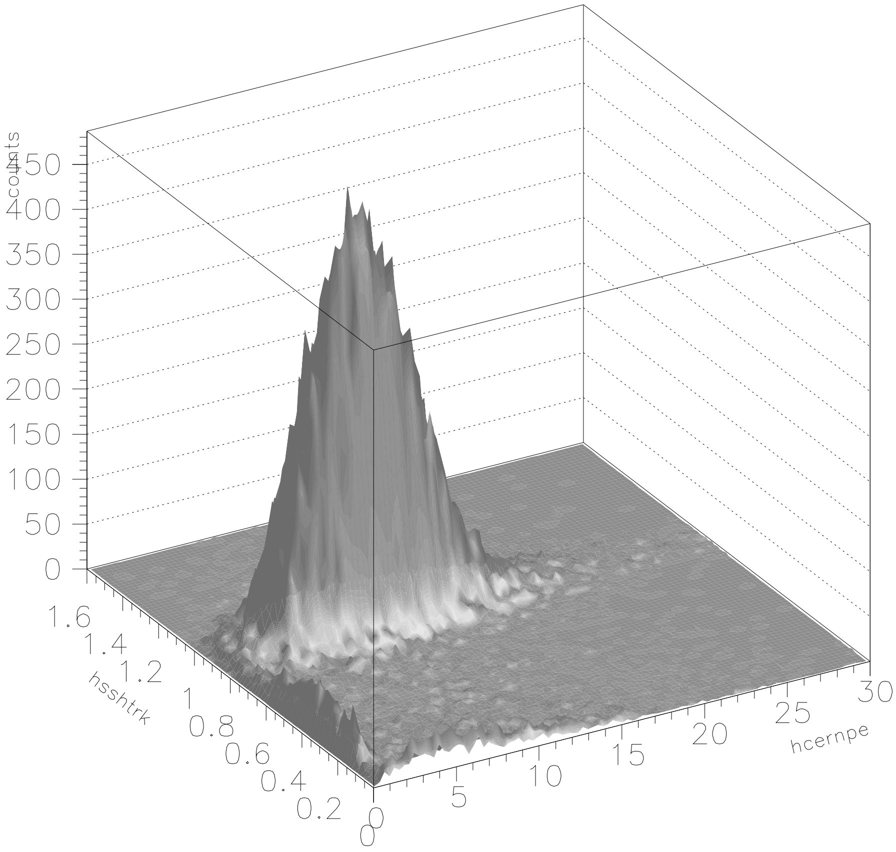

Figure 3.1: HMS Shower counter versus the gas Čerenkov. The electrons are the largest peak.

3.3.2 Electron Identification

The HMS, which served as the electron arm in this experiment, was sensitive to all negatively charges particles. The electrons had to be separated from the background of π^- hadrons. Because the electrons and pions were highly relativistic for the **E91-016** kinematics, they could not be separated by TOF measurements.

However, cuts applied to both the HMS gas Čerenkov and the lead glass calorimeter lead to a clean selection of electrons with an efficiency greater than 99.8%. For this analysis, an electron was identified as producing a signal greater than 2 photoelectrons in the gas Čerenkov and an energy deposition greater than 70% in the lead glass calorimeter. Figure 3.1 shows the clean separation of electrons, which are peaked at 13 photoelectrons, from the pions.

3.3.3 Kaon Identification

The SOS, which served as the hadron arm in this experiment, was sensitive to all positively charged particles. Because the cross sections for pion production and for inelastic proton scattering far exceeded that of kaon electroproduction, the task of separating clean kaons was more difficult than that of electrons. Looking at the velocity distribution in Figure 3.2, the large proton and pion peaks are clearly distinguishable, while the kaons are just a shoulder of the pion peak. The pion peak has already been suppressed due to the aerogel Čerenkov being included in the online trigger. The next several steps describe the process of obtaining the real kaons by eliminating the background of pions and protons.

Aerogel Čerenkov

In order to reduce the counting rates, the aerogel Čerenkov veto trigger in the SOS was set to veto particles generating greater than 6 photoelectrons. This trigger was loose enough to avoid cutting any real kaons, but substantially

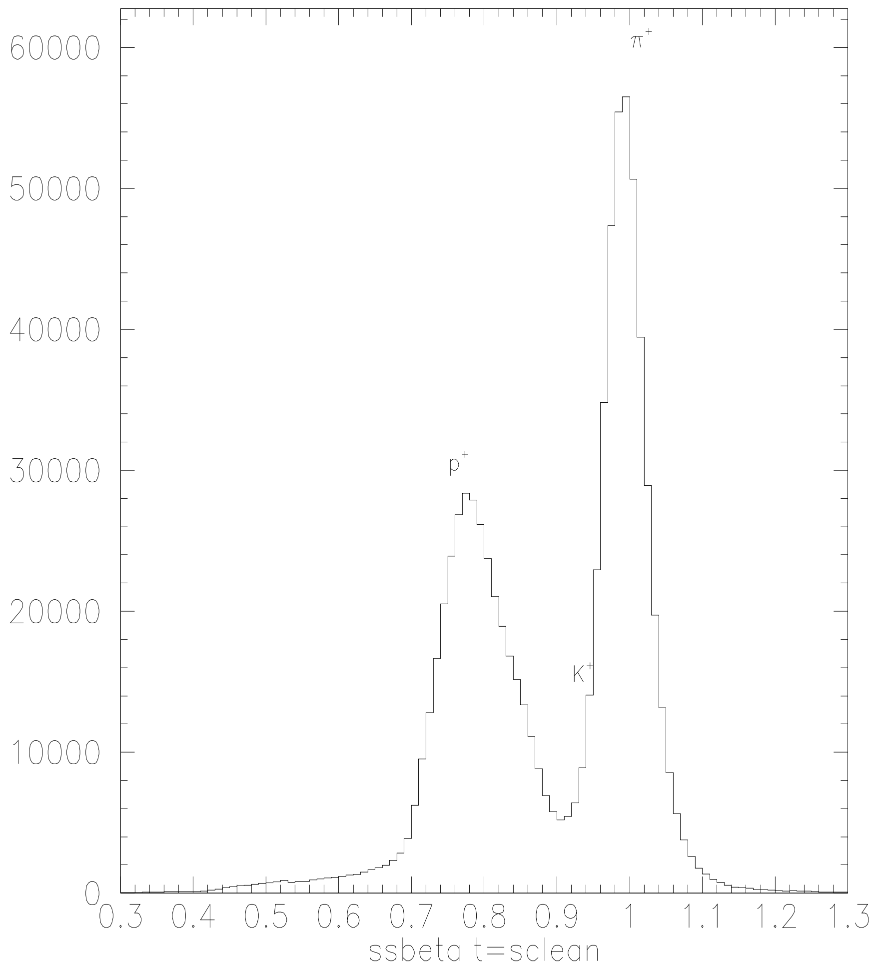

Figure 3.2: The beta distribution for all particles detected in the SOS.

reducing the huge background of pions, which is shown in Figure 3.3. A much tighter cut had to be applied in the offline analysis to further eliminate the pions. For this experiment, $\beta = 1.0$ particles yielded about 12 photoelectrons. Figure 3.4 shows the velocity distribution of particles in the SOS versus the number of photoelectrons in the aerogel detector. After careful analysis, an offline software cut of less than 1.7 photoelectrons was used to select kaons and reject pions. The

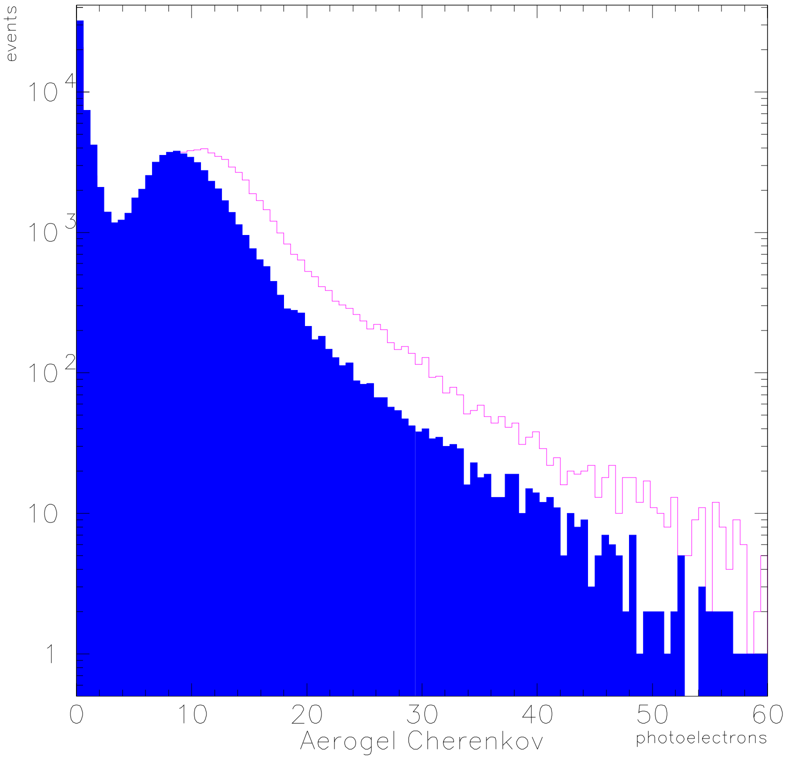

Figure 3.3: The yield of photoelectrons detected by the aerogel detector. Shown is the comparison of the normalized yield with (shaded) and without (unshaded) the aerogel detector in the trigger.

number of kaons that were lost in this cut is shown in Figure 3.5. The efficiency was measured by comparing the number of kaons that passed all the cuts to the number that passed all but the aerogel cut. The efficiency was 88.6 % ± 1.81%.

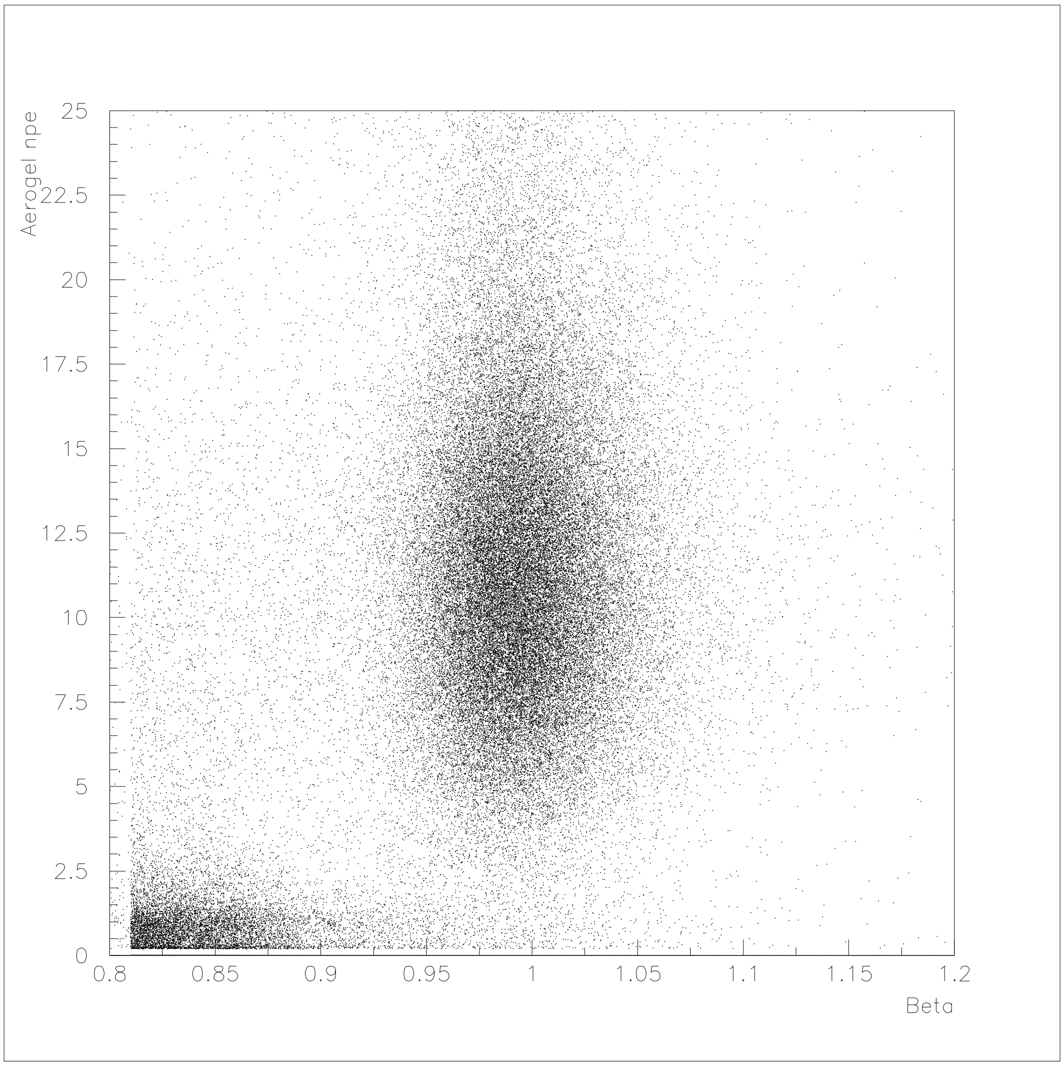

Figure 3.4: SOS beta versus the photoelectrons in the aerogel Čerenkov. The pions have an average photoelectron yield of 12 and $\beta \sim 1$.

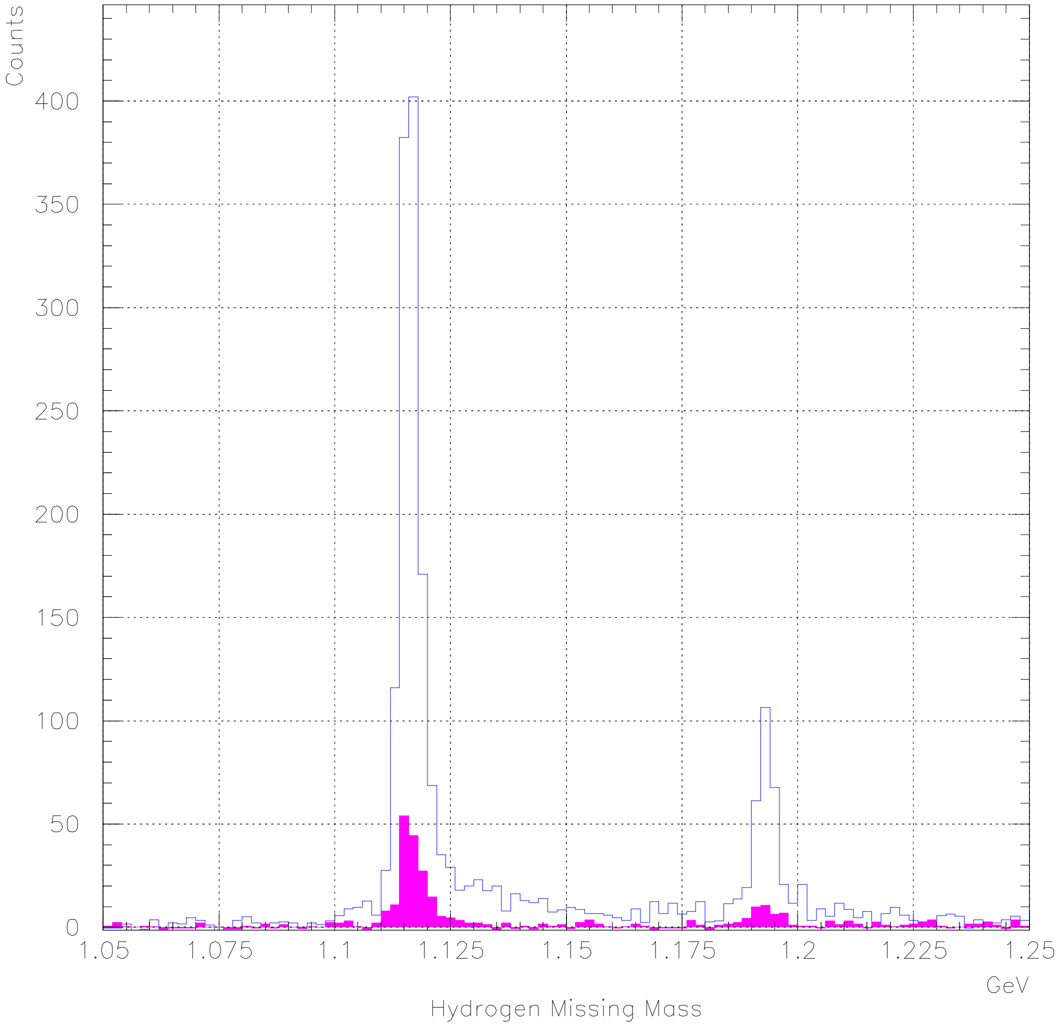

Figure 3.5: A comparison of kaons that passed or missed the aerogel cut.

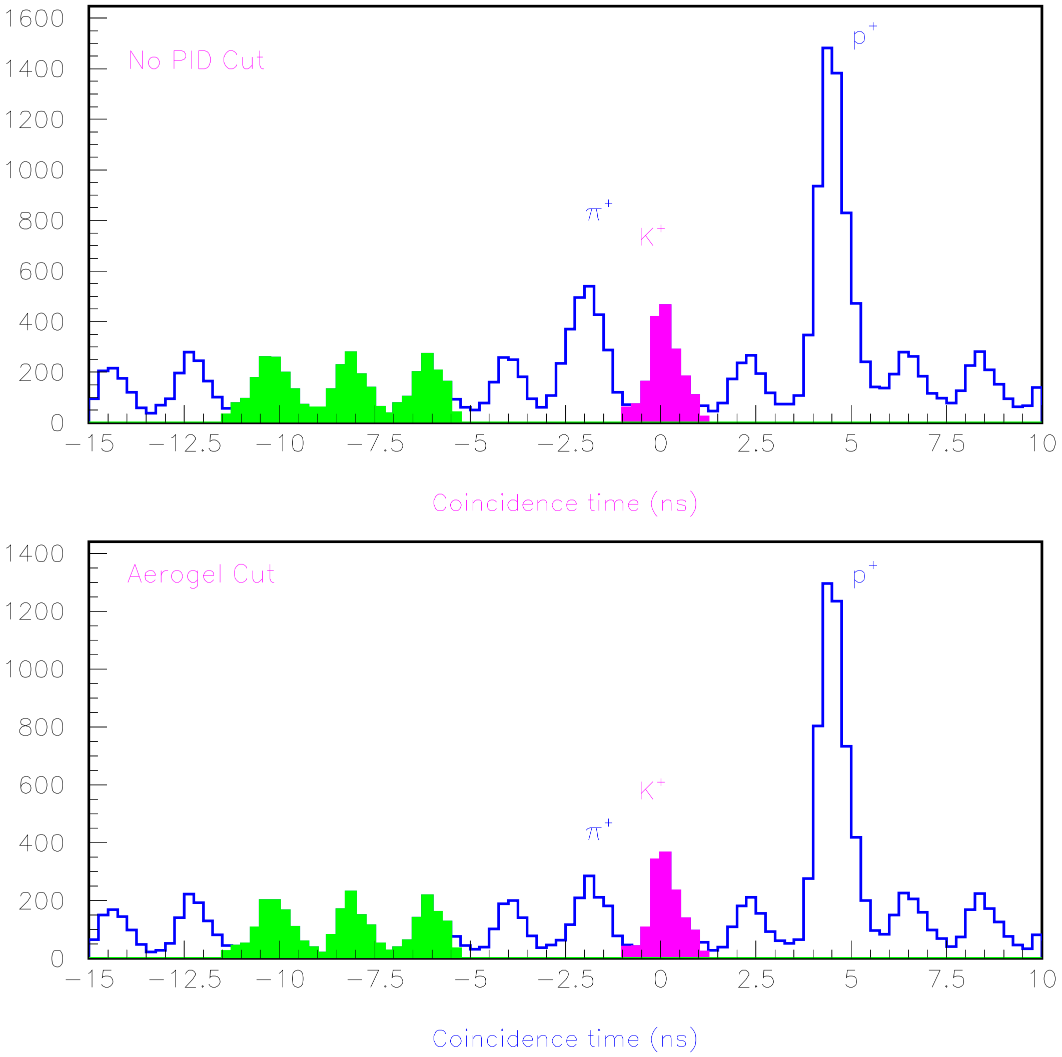

Figure 3.6: The cointime before and after an aerogel detector cut. The kaon and three of the random peaks are shaded. The pion peak has already been suppressed.

Coincidence Time

The coincidence time cut, which is the timing difference between the hadron arm and electron arm, was used to further select clean kaons. The electron and kaon were detected in coincidence with each other to form a coincident event. The top plot of Figure 3.6 shows the coincidence time before the other particle identification cuts have been applied. The electron beam bunches are delivered to Hall C in 2 ns intervals. Due to the good timing resolution in the hall, the beam structure could be seen. The coincidence timing scale has been offset to place the kaon peak at 0 ns. With this scale, the pions were visible at 2 ns and the protons at -4 ns. For each hadron, the random coincidences between uncorrelated events are also seen on each side of the real peaks. The kaon mass was used to evaluate the pathlength correction. This gives a better resolution for the kaon peak, but broadened the pion and proton peaks. To select real kaons without contamination of pions, a 2 ns cut was placed around the kaon peak, but offset by 0.06 ns from the mean coincidence time. Three random peaks were also selected such that there was no real pion contamination, then normalized by dividing by 3. The random event contribution was then subtracted from the real kaon peak to leave the true coincident kaon events. Because the width of the chosen coincidence window was larger than the average width of the coincidence time peak ($\sim$ 1 ns), there was no correction applied to the data for this cut.

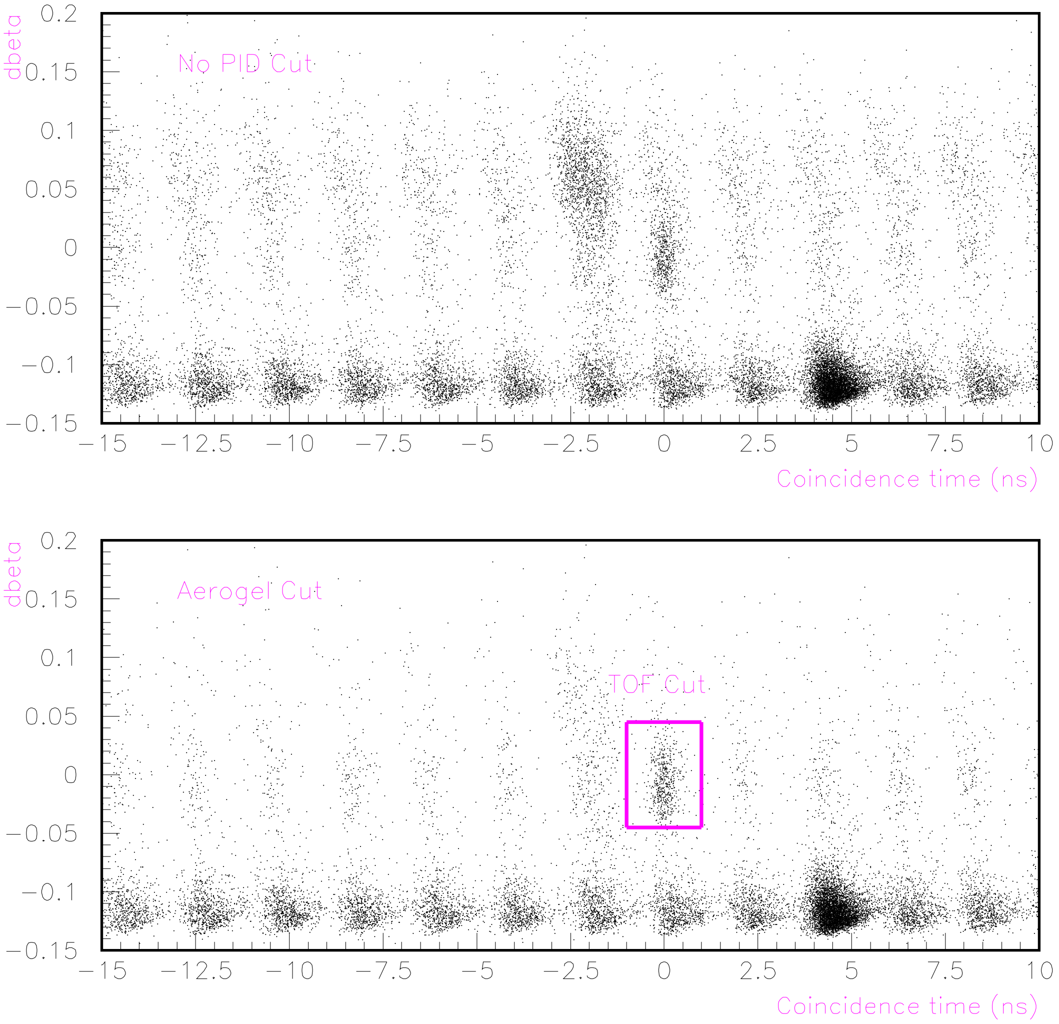

Figure 3.7: The $\beta_{TOF} - \beta_{momentum}$ versus coincidence time.

Time-Of-Flight (TOF)

The method that was chosen in this analysis was to place a cut on the difference between β as measured by TOF from the hodoscopes and β as calculated from the momentum and mass of the kaon. This momentum beta, $\beta_{momentum}$, was calculated according to $\beta_{momentum} = p/\sqrt{p^2 + m_K^2}$. The distribution of $\Delta\beta = \beta_{TOF} - \beta_{momentum}$ is shown in Figure 3.7. With the mass being correctly assigned to that of a kaon, the peak was clearly seen centered around zero. Since most of the kaon events were within a range of ±0.05, this cut is quite effective in eliminating proton and pion contamination. The cut efficiency was measured by comparing the number of kaons that pass all the cuts to the number that pass all but the beta cut. The efficiency was calculated to be 88.3% ± 1.93%. The bottom plot of Figure 3.7 shows $\beta_{TOF} - \beta_{momentum}$ versus coincidence time after the aerogel cut had been applied. The box around the real kaon events represents the $\beta_{TOF} - \beta_{momentum}$ and coincidence time cuts used in this data analysis.

Lucite Čerenkov

With the aerogel detector providing a means of π^+/K^+ discrimination, the lucite was available for p/K^+ discrimination. The lucite was set in the trigger such that if an event did not fire the aerogel detector, but did fire the lucite, it was accepted as a kaon event. This reduced the counting rate by rejecting a fraction of protons. However, this trigger was only used for half of the helium-3 data and most of the helium-4 data. The lucite trigger efficiency was approximately 100%. In this analysis, a time-of-flight cut was sufficient in proton/kaon discrimination, so an offline lucite cut was not used.

PID	Efficiency	Error (%)
Aerogel	0.886	1.81
$\beta_{TOF} - \beta_{mom}$	0.883	1.93
HMS Čerenkov	0.998	0.07
HMS Shower Counter	0.995	0.08
Kaon Absorption	0.950	1.0
Kaon Decay (double counting)	0.030	1.0

Table 3.3: PID cut efficiencies.

Target	Uncorrected Yield	Corrected Yield	Correction	Error(%)
h-0deg	19956	30516	1.58	0.867
h-6deg	30236	41155	1.43	0.930
h-12deg	22754	28764	1.31	0.947
he3-0deg	187596	268796	1.43	0.210
he3-6deg	56187	73704	1.31	0.458
he3-12deg	8393	10630	1.27	1.09
he4-0deg	177461	262539	1.48	0.270
he4-6deg	44827	63681	1.42	0.493
he4-12deg	9142	11892	1.30	1.05
d2-0deg	21097	31296	1.48	0.689

Table 3.4: Correction factors applied to data. This normalization factor includes trigger, tracking, dead times, and lost events due to coincidence blocking and beta=0 assigned events. The correction is the ratio of corrected yield to uncorrected yield.

3.4 Efficiencies/Normalizations

From using the previously discussed particle identification cuts to select real coincidence electron and kaon events, the resulting missing mass was determined. The yield of the missing mass had to be corrected by the calculated cut efficiencies and other losses due to tracking, computer and electronic dead time, absorption, kaon decay, and other detection efficiencies. These various corrections and errors will be described in the following sections. Table 3.3 gives the summary of all the particle identification cut corrections applied to the missing mass yield. Table 3.4 gives the summary of the efficiency corrections that were applied to the data. This final correction includes the weighted average of the trigger and tracking efficiency, computer and electronic dead times, coincidence blocking, and beta = 0 events. Each of these corrections were first calculated on a run-by-run basis to determine the correct weighted average.

3.4.1 Tracking Efficiency

The wire chambers give the essential information needed in calculating the tracking for an event. Since the wire chambers are not included as part of the trigger, a good trigger may not yield good tracking information. This occurs for some events when there is not enough information to reconstruct a track, such as too few or too many wires firing for an event. The tracking efficiency is measured for all events, not just the kaon events. Because of such low statistics, the tracking efficiency could not be measured directly for kaons.

The basic concept of tracking efficiency is to measure tracks that appear to pass through the center of the spectrometer. It is defined as the number of events for which a track is found, divided by the number of events which is expected to have a real track. This ratio is referred to as the fiducial tracking efficiency. The tracking efficiency was first determined on a run-by-run basis. The weighted average was calculated using the correct charge normalization. Figure 3.8 shows that the tracking efficiency for the HMS was typically 97-99% and 94-98% for the SOS.

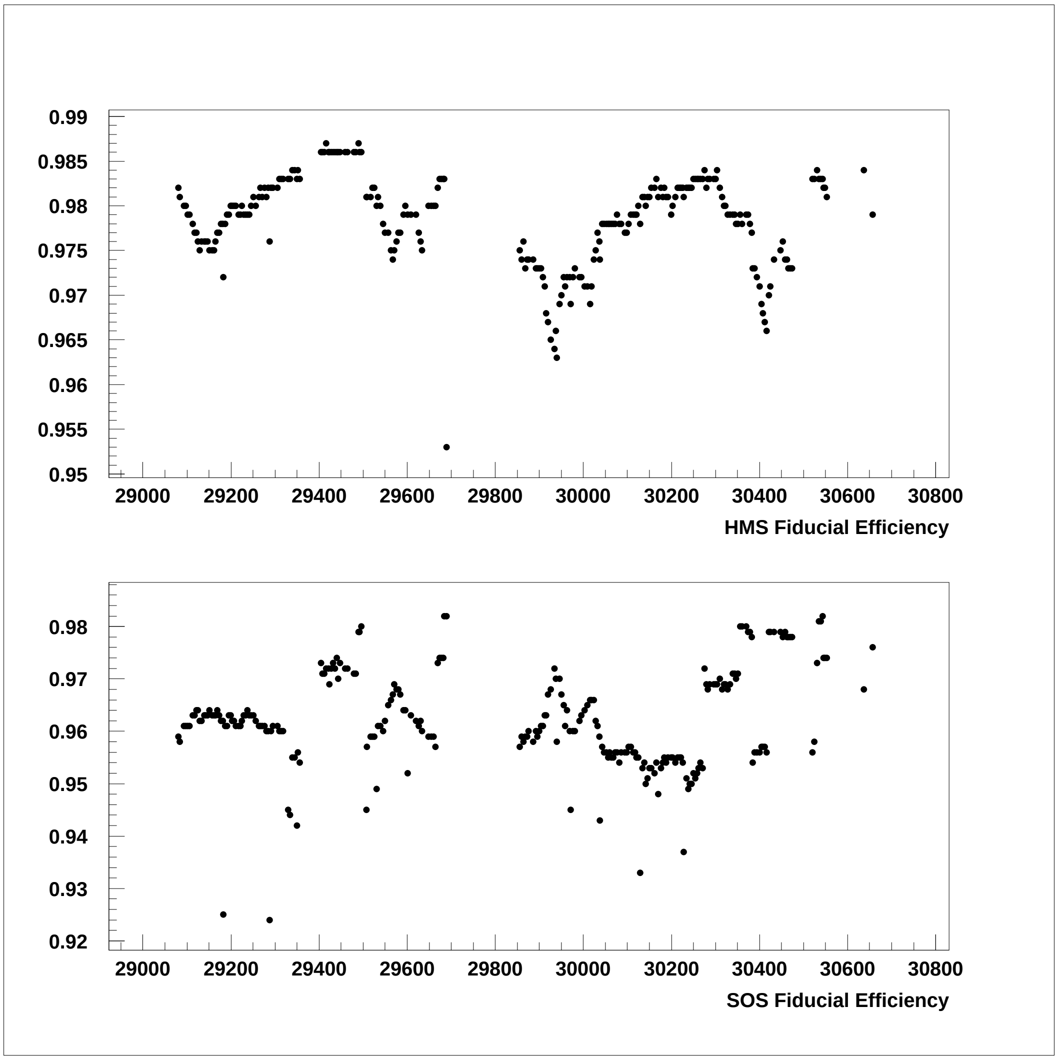

Figure 3.8: The run versus the tracking efficiency.

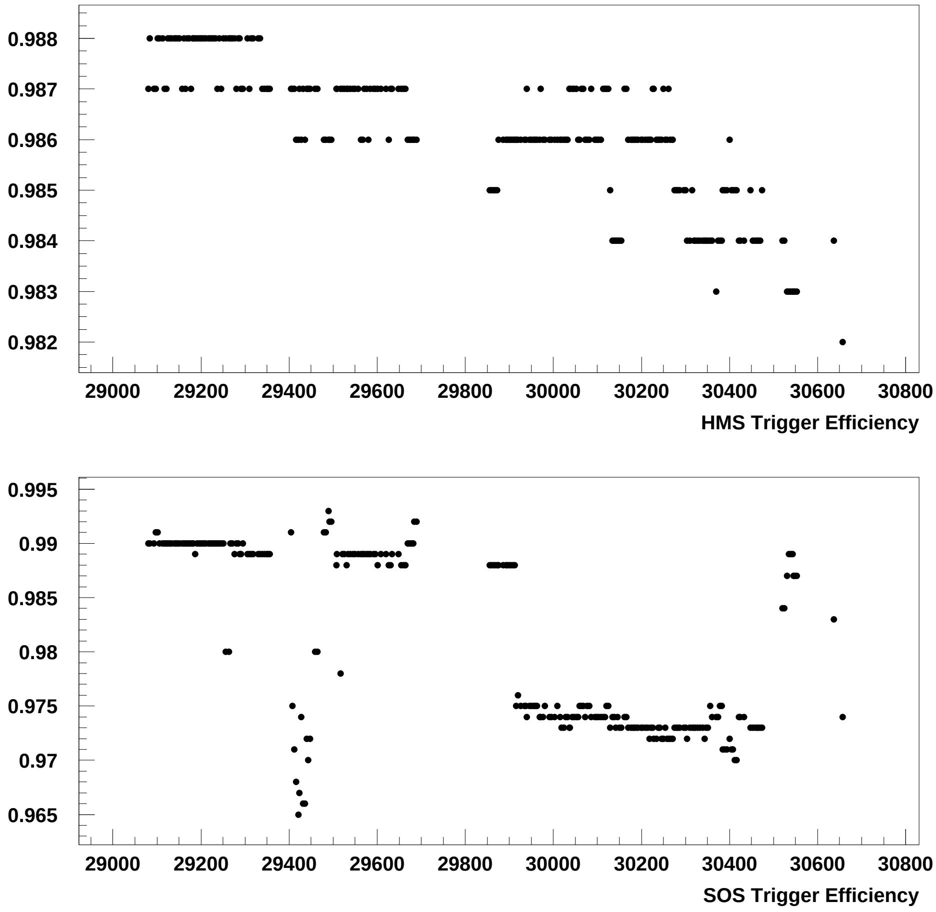

Figure 3.9: The run versus the 3/4 trigger efficiency.

3.4.2 Trigger Efficiency

Events can be missed due to inefficiencies in the hodoscopes. Using the measured efficiency of each scintillator, the probability of missing a trigger was calculated and corrected in the data. Recall that the trigger required only that three of four scintillator planes fire for both the HMS and the SOS. The probability that more than one plane will not fire for any given event is low. The trigger efficiency was calculated by comparing the number of events which had 3/4 planes fire to those that had 4/4. The efficiency was determined on a run-by-run basis, after which a weighted average was calculated. Figure 3.9 shows the trigger efficiency versus run. The HMS and SOS both had high efficiencies of 98-99%.

3.4.3 Electronic and Computer Dead Time

Electronic Dead Time

Events can be lost when a signal reaches a logic module where the gate has already been activated by a previous signal. These ignored events due to open gates gives the loss called electronic dead time. The width of all logic gates used in Hall C was 30 ns. Any event arriving within 30 ns of an event accepted by the gate will be missed by DAQ. The electronic dead time was measured by comparing the number of events missed by the 30 ns window to that of 60, 90, and 120 ns logic gate windows. Figure 3.10 shows the livetime for the HMS and SOS per run. Both the HMS and SOS had small corrections of less than 2%.

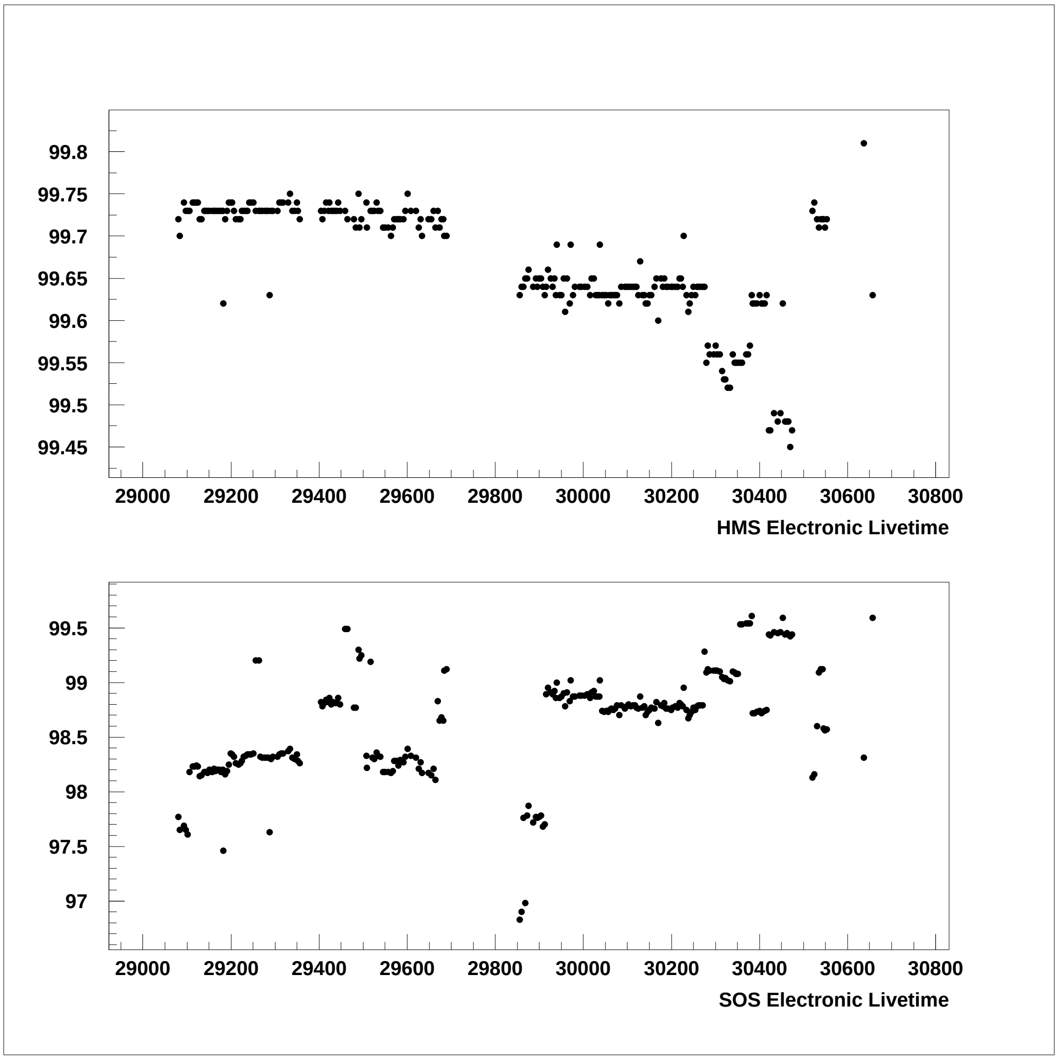

Figure 3.10: The run versus the electronic livetime for the HMS and SOS.

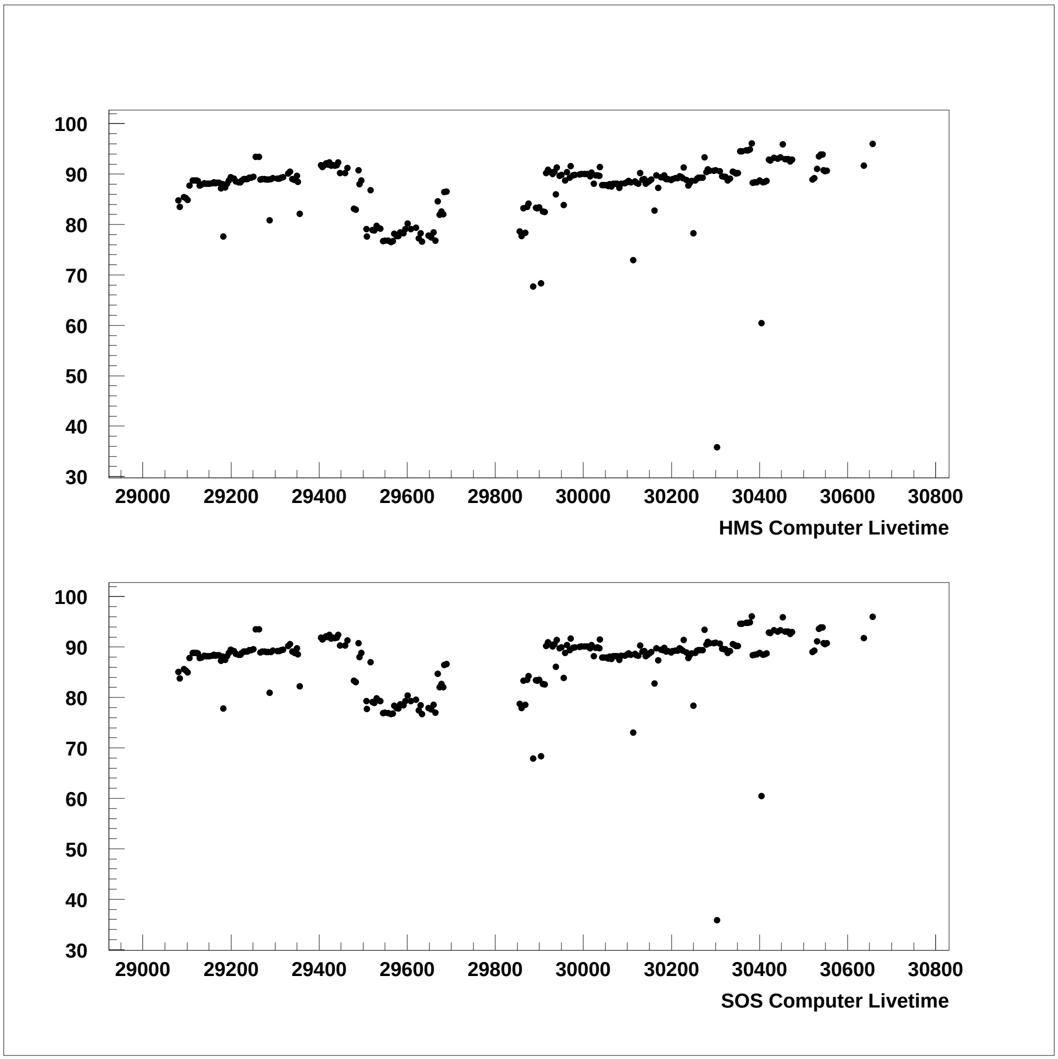

Figure 3.11: The run versus the computer livetime for the HMS and SOS.

Computer Dead Time

Computer dead time is a more significant loss than that of electronic dead time. This loss occurs when events are lost because the data acquisition is busy processing the previous event. The total processing time for an event was $\sim 400\mu$s.

This time interval can be reduced by a factor three when running in buffered mode. In buffered mode, events are stored while DAQ is busy processing an earlier event. The concern in running in buffered mode was the loss of synchronicity. This occurred when TDC readouts were attached to the wrong event. Synchronicity was checked every 1000 events. The processing time for coincidence events was higher than for single arm. The computer dead time was calculated by taking the ratio of triggers to pretriggers. Depending on the target and the current, the computer dead time varied between 8-24%, as shown in Figure 3.11.

3.4.4 Coincidence Blocking

Another source of dead time occurs when an extra SOS single event arrives in the same 40 ns coincidence window of a real coincidence event. This is called coincidence blocking because a mis-timing occurs in the ADC gates and the TDC stops for the next coincidence event. Therefore, the next coincidence event will appear outside the coincidence window. Figure 3.12 shows a typical raw coincidence spectrum. The blocked events are shown clustered several hundreds of TDC channels away from the good coincidence events. The correction was calculated by dividing the number of blocked events (the shaded area) by the total number of coincidences. A weighted average was calculated for each target and setting. The correction varied from 1-5%.

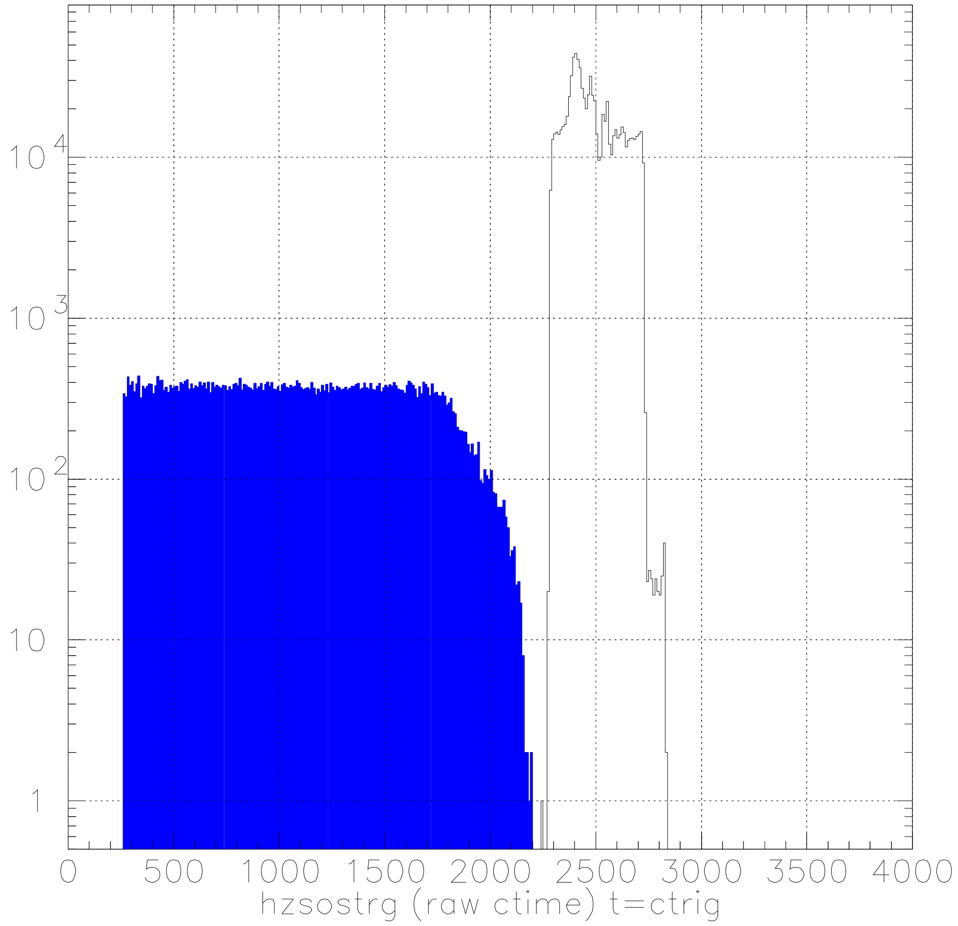

Figure 3.12: A raw coincidence time distribution. This shows the time difference between the blocked (shaded) and unblocked events.

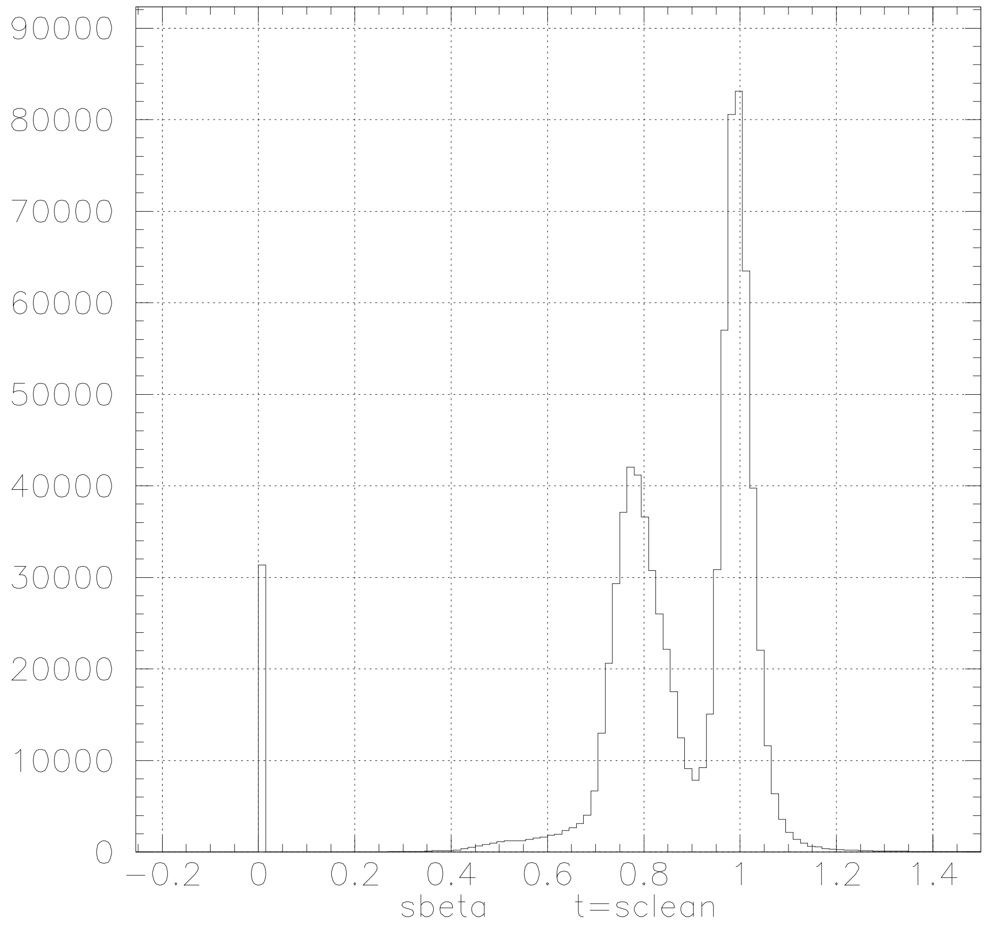

Figure 3.13: A β distribution showing the events assigned a value of $\beta = 0$.

3.4.5 Beta = 0

An event is assigned the value $\beta = 0$ when the projection of the track from the drift chambers did not meet with the corresponding paddle in the hodoscope planes. This could happen when there are not enough recorded scintillator hits on the track or bad scintillator times extracted from the TDC/ADC outputs. These events are lost in the $\beta_{TOF} - \beta_{momentum}$ cut. Since the efficiency of this cut was only evaluated for events with $\beta > 0$, a separate correction had to be applied. It was assumed that the percentage of beta = 0 events was independent of the particle type. Using this assumption, the correction was calculated as the ratio of all blocked events to the total number of events. Figure 3.13 shows a beta spectrum with the beta = 0 events clearly peaked. The correction was typically between 3-5% and applied as a weighted average to the overall yield.

3.4.6 Kaon Decay

The K^+ meson is an unstable particle with a mean lifetime of $\tau = (1.2371 \pm 0.0029)$ x 10^{-8} s. Because of this, a significant percentage ($\sim$ 70%) of the kaons decayed into secondary particles before detection at the SOS detector hut. The Monte Carlo simulation, which will be discussed in the next chapter, includes kaon decay. This simulation allows for decay inside the spectrometer and in the detector hut. The Monte Carlo uses the spectrometer acceptance, detector aperture cuts, and the two-body and three-body decay modes. All decay modes with branching ratios greater than 1% were implemented in the code. Table 3.5 lists the decay channels of the K^+ meson that were included in the simulation code.

In the first approximation, the kaon survival probability was calculated

Decay Modes	Branching Ratio (%)
$\mu^+\nu_\mu$	63.51 ± 0.18
$\pi^+\pi_\circ$	21.16 ± 0.14
$\pi^+\pi^+\pi_-$	5.59 ± 0.05
$\pi^\circ e^+\nu_e$	4.82 ± 0.06
$\pi^\circ\mu^+\nu_\mu$	3.18 ± 0.08
$\pi^+\pi^\circ\pi_\circ$	1.73 ± 0.04

Table 3.5: Table of K^+ decay channels. Other channels with branching ratio less than 1% are not shown.

using the well-known equation:

$$P(x_o) = e^{-Mx_o\Gamma/|\vec{p}|} \tag{3.1}$$

where P(x_o) is the survival probability of a particle with mass, M, and momentum, $\vec{p}$, traveling a distance x_o. Γ is the inverse of the mean lifetime, which is 12.4 ns for a kaon. Careful studies revealed that there is no contribution from kaons which decay in the spectrometer. The primary concerns are for the kaons which decay between the field boundary of the last SOS dipole and the aerogel detector. There is a small fraction of the decay particles which corresponds to the beta of a kaon, fires 3/4 scintillator planes, and does not fire the aerogel. The particle identification process would count these decay products as kaons. Since the Monte Carlo has already corrected for these decayed events, this would lead to double-counting. Previous studies at the same momentum have shown that an overall double-counting correction of 3% needed to be applied to the data [13] [28].

Material	Thickness(cm)	rho(g/cm^3)	$X_0(g/cm^2)$	r.l.(%)	Notes
Target					
Entrance cap	0.0121	2.70	24.01	0.136	
LH2	4.00	0.0723	61.28	0.472	
LHE3	4.00	0.0773	58.36	0.529	
LHE4	4.00	0.1364	94.32	0.578	
Exit cap	0.0121	2.70	24.01	0.136	
Chamber exit	0.0203	2.70	24.01	0.288	8 mil Al
Spectrometer					
Air	~ 15	0.00121	36.66	~ 0.050	
Kevlar entrance	0.0127	0.74	55.2	0.017	5 mil Kevlar
Mylar entrance	0.0076	1.39	39.95	0.027	3 mil Mylar
Kevlar exit	0.0381	0.74	55.2	0.051	15 mil Kevlar
Mylar exit	0.0127	1.39	39.95	0.044	5 mil Mylar
Hut					
Air	~ 15	0.0021	36.66	~ 0.050	
DC Mylar	0.0178	1.39	39.95	0.062	14 planes
Ar/CH_4 gas	7.41	0.00154	~ 25.7	~ 0.044	
Sense Wires(W)	0.00008	19.3	6.76	0.022	$12 \times 30\mu m$ wires
Field Wires(W)	0.00034	19.3	6.76	0.098	$12 \times 60\mu m$ wires
Air	~ 49.5	0.0021	36.66	~ 0.1633	
S1Y	1.098	1.03	43.8	2.582	1.098 for overlap
S1X	1.04	1.03	43.8	2.446	1.04 for overlap
CER entr.	0.05	2.70	24.01	0.056	
CER gas(Freon)	~ 100	0.0051	~ 23.7	~ 2.152	Density for 1 atm.
CER mirror	-	-	-	0.5	
CER exit	0.05	2.70	24.01	0.056	
S2Y	1.098	1.03	43.8	2.582	1.098 for overlap
Aerogel entr.	0.0625	2.70	24.01	0.70	
Aerogel	9.0	-	-	~ 6	
Lucite	2.54	1.16	40.49	7.28	

Table 3.6: Table of SOS materials. These table entries are used to calculate kaon absorption and multiple scattering.

3.4.7 Kaon Absorption

Once the kaons were produced at the target, they had to travel $\sim$ 10.23 m before being detected in the SOS hut. Although most of this distance is in a vacuum system, there are various materials that act as kaon absorbers, including the detectors. A number of hadrons were lost to elastic/inelastic scattering off the materials that were encountered; therefore, an absorption correction factor was applied. The materials which the kaons encountered and interacted from the target through the SOS spectrometer are listed in Table 3.6 . Absorption of electrons in the target and the HMS spectrometer is negligible compared to kaon absorption. The fraction of particles absorbed by each material could be calculated using,

$$n = n_o \frac{N_A \rho}{A} t \sigma_o, \tag{3.2}$$

where A is the atomic number of the material, ρ is the density, t is the thickness, N_A is Avogadro's number, and n_o is the number of particles incident on the material. The absorption cross section, σ_o, was calculated using a K-N scattering calculation based on the multiple scattering theory of Kerman, McManus, and Thaler, where

$$\sigma_o = 21.065 p_K^{-0.99} A^{0.79}. \tag{3.3}$$

For the kaon momentum, p_K, in this experiment, the average absorption correction was previously found to be on average of 5% [13] [28].

CHAPTER 4

Monte Carlo Simulation

A simulation code was needed to accurately analyze data for the kaon electroproduction on helium. In order to determine the contribution from the hyperons, Λ, Σ^0, and Σ^-, each has to be modeled correctly. The Monte Carlo simulation for Hall C, SIMC, is based on a code written by N. Makins and T.G. O'Neill at SLAC. The code was modified for Hall C to model the optics of both the spectrometers and detectors, energy loss, multiple scattering, radiative corrections, and kaon decay. The code was first tested by simulating elastic scattering, *(e,e')* and *(e,e'p)* [29]. It was then modified to include kaon decay and the momentum distribution of the proton in the ^{3}He and ^{4}He nucleus. Complete details of the Hall C simulation code can be found in [30].

4.1 Event Generation

The code begins by randomly generating the quantities needed to fully describe the event. These random quantities cover a range greater than that of the spectrometer acceptance. Taking into account the raster pattern and beam width, the position of the interaction within the target cell is generated. Fluctuations of the beam energy and corrections for ionization loss in the target are implemented

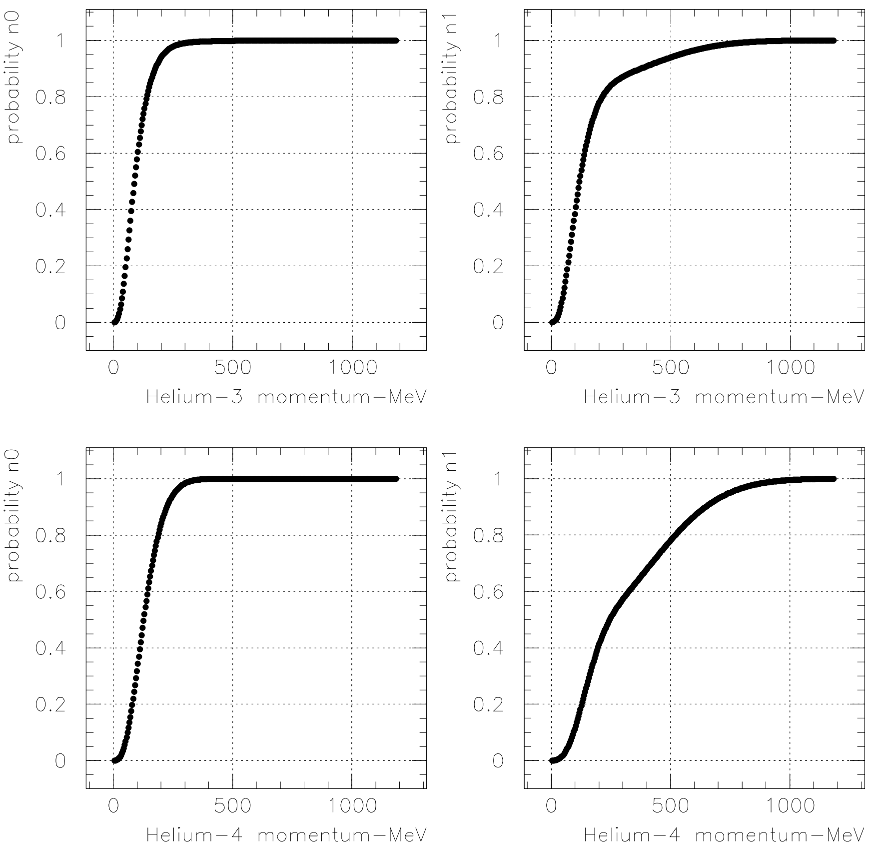

Figure 4.1: Atti normalized momentum distribution for ^{3}He and ^{4}He.

when generating the incoming electron energy. The two angles which determine the direction of the outgoing electron and kaon are randomly generated. The Fermi momentum of the nucleon in the nucleus is calculated for the nuclear targets and energy is conserved by including the recoil of the target nucleus. The last of the generated quantities needed is the electron energy. To model the momentum distribution of the proton in the helium-3 and helium-4 nucleus, a model from Ciofi

Hyperon	Final States	% Contribution
Λ, Σ^0	(pn)	65.3
Λ, Σ^0	pn	34.7
Σ^-	pp	100.0
Λ, Σ^0	(pnn)	80.0
Λ, Σ^0	(pn)n,pnn	20.0
Σ^-	(ppn)	80.0
Σ^-	p(pn),ppn	20.0

Table 4.1: Contribution of final states for Atti momentum distribution. Production from ^{3}He is shown in the top portion and ^{4}He in the bottom. The parentheses indicates a bound system. One weight is applied to the indistinguishable systems.

degli Atti was tested [31]. The probability to find a proton with a certain momentum, P_m, in the nucleus is given. Due to helium-3 and helium-4 having a possibility of several different final states, simulations are used to model these possibilities. Table 4.1 gives the final states that are taken into account for each hyperon production and the contribution weight assigned. The normalized distributions are shown in Figure 4.1. A random number is chosen such that it is greater than the probability of the momentum, but less than one. A high and low value for the Fermi momentum is determined, and the momentum is calculated according to equation 4.1. From this point, the physics angles of the electron and kaon are calculated. If the random choices of variables make the kinematics unsolvable, the event fails. Now that the kinematics are determined, the kaon momentum can be calculated.

$$P_{fer} = P_{low} + (P_{high} - P_{low}) * R \tag{4.1}$$

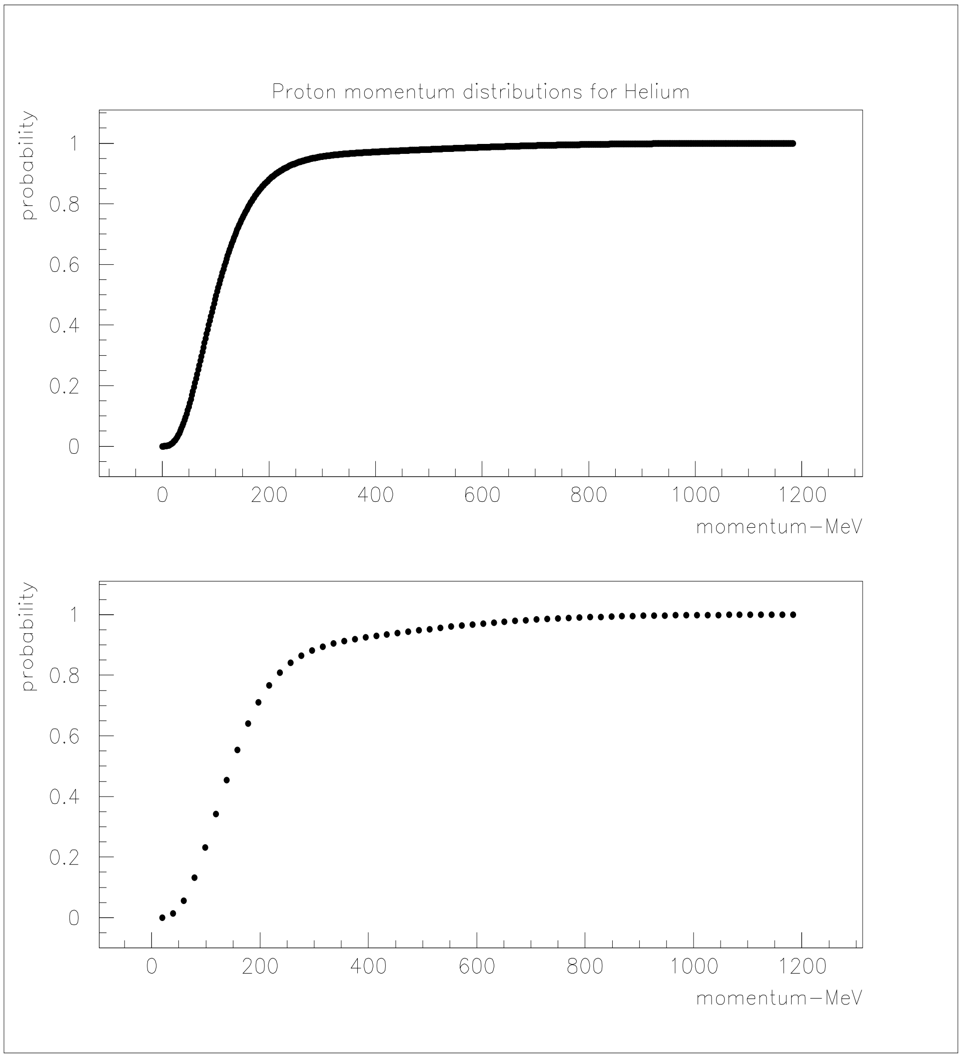

Figure 4.2: Helium momentum distribution for the spectral function. The top figure is ^{3}He and the bottom is ^{4}He. Both are the distributions for the proton.

For this analysis, a simulation which included a spectral function for kaon electroproduction was also used. This spectral function is taken from O. Benhar, and is discussed in more detail in [32]. The spectral function uses P_m to generate E_m by using the E_m distribution appropriate to the given P_m. The probability is known of finding an event with a certain momentum and energy. Figure 4.2 shows the normalized momentum distribution which was used by the spectral function. Ideally, the spectral function should simulate the data more properly than the pure momentum distribution because it contains more information about the event. Figures 4.3 and 4.4 displays an overlay of the missing mass distribution for the Λ, Σ^0, and Σ^- for each simulation. The missing mass distribution for Σ^- using the Atti momentum distribution seems to have a higher normalized yield than that of the Benhar spectral function, although the shapes of each are similar. The leading edge beyond threshold differs by 2 - 4 MeV. Both simulations were available, so the results of both the full spectral function and the pure momentum distribution will be discussed and compared in the final analysis.

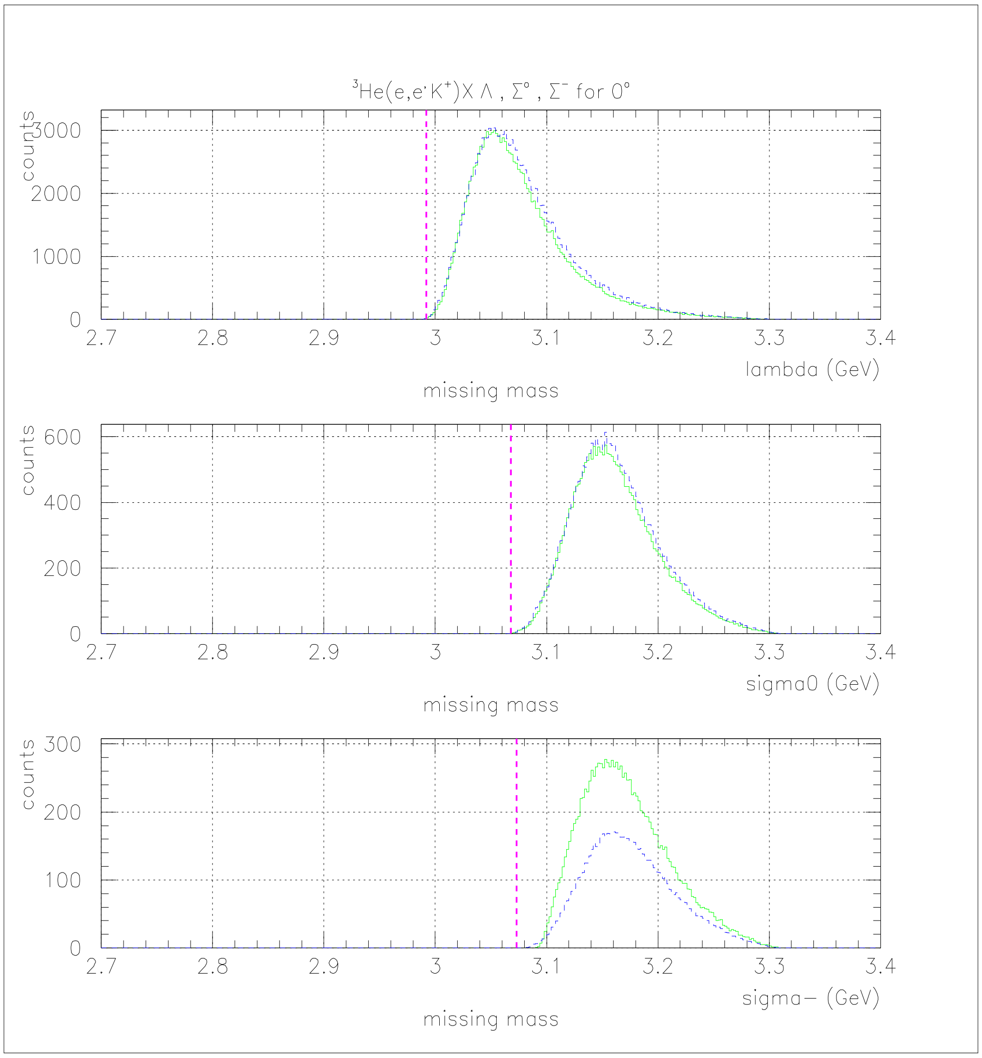

Figure 4.3: Simulation of missing mass for Λ, Σ^0, and Σ^- from ^{3}He. The solid line is the Atti momentum distribution and the dashed is the Benhar spectral function. Each has been properly normalized.

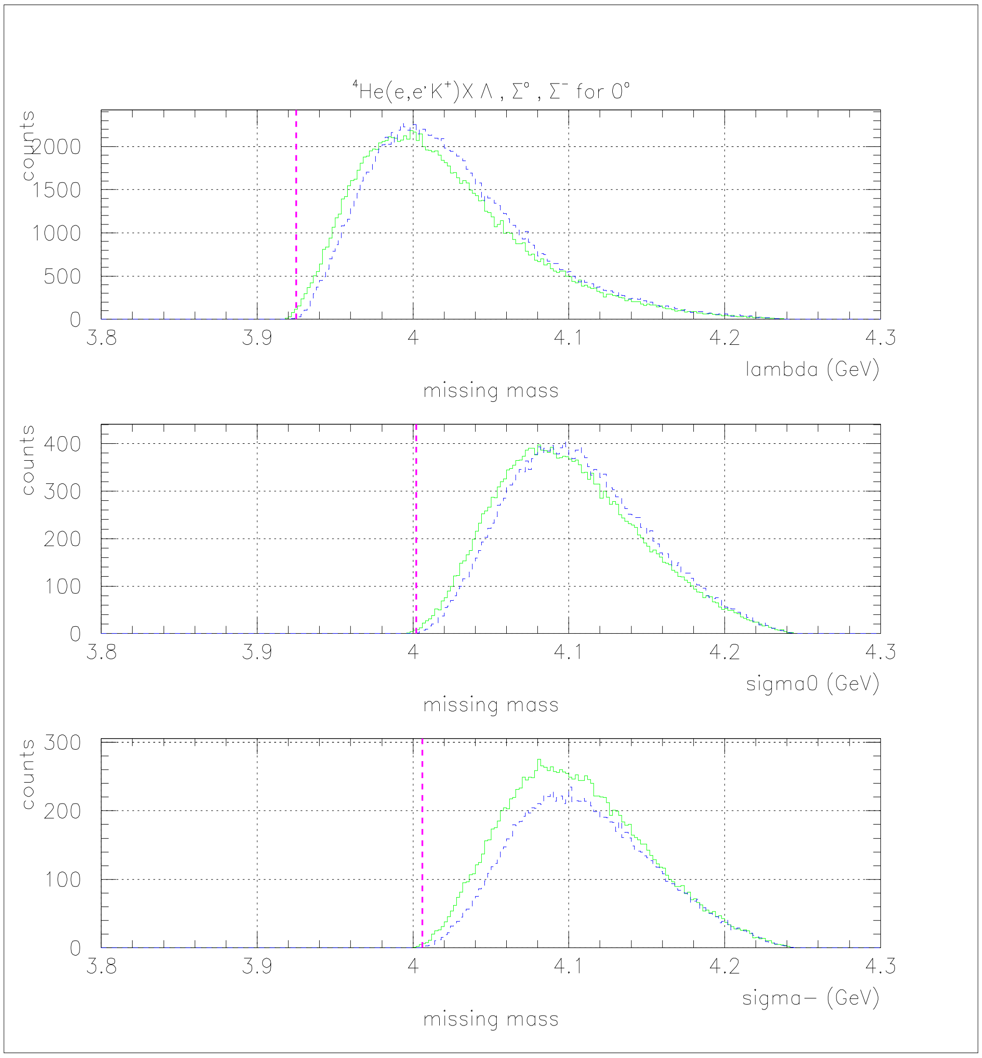

Figure 4.4: Simulation of missing mass for Λ, Σ^0, and Σ^- from ^{4}He. The solid line is the Atti momentum distribution and the dashed is the Benhar spectral function. The threshold for production is also shown.

4.2 Transport through the Spectrometers

Once the momentum and angles are determined for the kaon and outgoing electron, the particles are transported through the spectrometers to the respective detector huts. The path through each spectrometer is determined by a set of sequential matrix elements that are derived from the COSY INFINITY transport program [33]. The matrices transport the particles through each magnet element from A $\rightarrow$ B, B $\rightarrow$ C, and C $\rightarrow$ D. The particles that fell outside of the aperture of the collimators, magnets, and detector elements are thrown out as a failed event.

After the particle has been transported through the spectrometer, it is simulated through the detector hut. For a realistic model of the drift chamber resolution, the position of the particle in each chamber plane is smeared with a Gaussian equal to the width of the measured chamber resolution. The particle is considered to have made it through the detector hut once it passes through each required detector element. For the HMS, this is the third scintillator plane, and for the SOS, it is the aerogel detector. Although most of the particle path is in vacuum, multiple scattering can occur in places such as vacuum windows, air, drift chamber wires, and scintillator paddles, which is also simulated. The focal plane quantities are then calculated and used to determine the reconstructed target quantities. To do this, the path has to be reconstructed back through the spectrometer to the target using the inversion of the forward matrix elements.

4.3 Radiative Corrections

Radiative corrections for the incoming and outgoing electron and hadron are included in SIMC. Because radiative corrections for the reaction (e,e'p) are in the original code, it is only slightly modified by the proton being offshell. For this data, the offshell proton is a kaon, but due to expected small contributions from hadron corrections, this approximation is acceptable. The contribution from the protons and kaons is negligible compared with the electrons. The calculations for the radiative corrections include the external Bremsstrahlung and internal contributions. The external Bremsstrahlung radiation is real photon emission which reduces the energy of the radiating particle. Therefore, the beam energy at the vertex is modified, which changes the kinematics. This same modification is applied to the outgoing particles momenta. The internal Bremsstrahlung radiation is divided into hard and soft processes. The soft radiative correction involves the emission of real photons, whereas the hard radiative process does not.

The relative probability for radiation in each spectrometer arm is calculated for the incoming and outgoing electron and the outgoing kaon. The radiated photon is assigned to be in a particular arm based on this value. If the outgoing electron does not fall into the HMS spectrometer acceptance without being radiated, then the radiated photon is assigned to be in that arm. The event is weighted by the relative probability that the outgoing electron would have radiated. The physics is recalculated for the events from which the incoming electron radiated.

However, when the final particle radiates, the 4-vector for the particle is modified. The direction of the radiated photon is fixed to be in the same direction as the particle from which it radiated. The energy of the photon is calculated based on a ω^{r-1} distribution, where ω is the photon energy and r is determined by the formulas used for radiative corrections. The radiative weights are combined with the physics cross section weight.

4.4 Decay Weight

The survival probability of the kaon with a flight path from the target to the aerogel detector is calculated in SIMC using equation 3.1. This is an added weight on the physics cross section. Only the two and three-body decay modes, in Table 3.5 are implemented. For the two-body decays, the decay particles' momenta in the decay rest frame are fixed. For the three-body decays, an average momentum is chosen rather than modeling the momentum distribution. After a random direction in the rest frame is chosen, the particles 4-vector is boosted into the lab frame and transported through the rest of the spectrometer. Because a small percentage of the decay products pass the kaon particle identification cuts, a correction has to be applied to the data yield to account for this double counting. A more detailed discussion can be found in Chapter 3.

4.5 Physics Cross Section

The kaons and coincident electrons that pass through the spectrometer and loose angle and momentum cuts are assigned a physics cross section weight. The e-K coincidence acceptance of the spectrometers is determined by combining the ratio of successes to attempts with the initial five-dimensional generation volume. The cross section parameterization, equation 4.2, that is used for Λ is discussed in detail in [11]. An iterative procedure was used to determine the function of each kinematic variable, Q^2, W, t, and ϕ. These functions are shown in equation 4.3, 4.4, 4.5, and 4.6. The constants, P_i, are shown in Table 4.2. The model for $\Sigma^{0,-}$ is just a W-parameterization, $\frac{p_K}{(W^2-M^2)W}$, where p_K is the three momentum of the kaon.

$$\frac{d\sigma}{d\Omega}(Q^2, W, t, \phi) = f(Q^2)g(W)h(t)i(\phi), \tag{4.2}$$

$$\begin{aligned}
f(Q^2) &= Constant & (4.3)\\
g(W) &= \frac{P_1 P_k^{CM}}{(W^2 - M_p^2)W} + \frac{P_2 W^2}{(P_3 W)^2 + (W^2 - P_4^2)^2} & (4.4)\\
h(t_{min} - t) &= P_1 e^{P_2(t_{min}-t)} & (4.5)\\
i(\phi) &= P_1 + P_2\cos(\phi) + P_3\cos(2\phi) & (4.6)
\end{aligned}$$

Function	P_1	P_2	P_3	P_4
$f(Q^2)$	0.430 ± 0.005			
$g(W)$	4.470 ± 0.005	0.00089 ± 0.00086	$0.0787 \pm .02458$	1.72 (fixed)
$h(\Delta t)$	0.4262 ± 0.0056	-2.144 ± 0.211		
$i(\phi)$	0.438 ± 0.006	$-0.048 \pm .009$	0.008 ± 0.009	

Table 4.2: The constants of the cross section parameterization.

Using the cross section model, a cross section in the center of mass of the virtual photon is calculated for each passed event. The five-fold differential cross section (laboratory cross section) is calculated by multiplying this number by a Jacobian and the virtual photon flux. This is shown in equation 4.7 as

$$\frac{d^5\sigma}{dE_{e\prime}d\Omega_{e\prime}d\Omega_K} = \Gamma J \frac{d\sigma}{d\Omega_K{}^*} \tag{4.7}$$

where the virtual photon flux, Γ, is

$$\Gamma = \frac{\alpha}{4\pi^2}\frac{E\prime(W^2 - M^2)}{EMQ^2(1-\epsilon)} \tag{4.8}$$

and the Jacobian, J, between the center-of-mass and the laboratory is given by $J = d\cos\theta^*/d\cos\theta$. Furthermore, a decay weight is applied to the cross section to correct for the survival probability of the kaon over the pathlength to the aerogel. The computed simulation yield includes target normalizations, decay, radiative corrections, spectrometer acceptance, the initial model cross section, and charge normalization. The data cross section is obtained by multiplying the average Monte

Carlo cross section by a factor necessary to scale the simulation to data. The agreement between the simulation and data for the reconstructed target quantities is shown in Figure 4.5

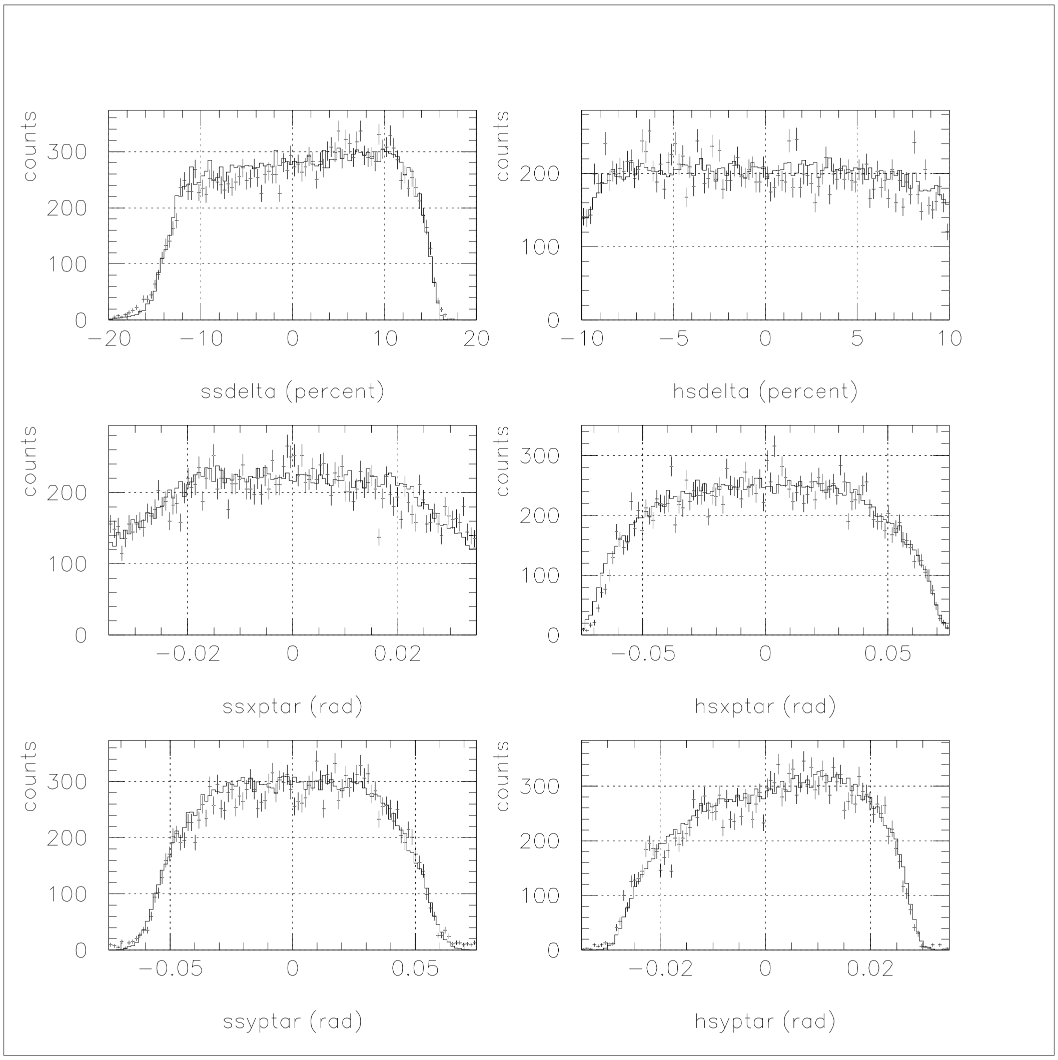

Figure 4.5: H(e,e'K)Λ data vs SIMC for reconstructed quantities. The solid line is SIMC and the data is shown with statistical error bars. The proper normalization has been applied to SIMC to scale to the data.

CHAPTER 5

Results

5.1 Hydrogen

Measurement of the differential cross section for kaon electroproduction on the elementary reaction, $p(e, e'K^{+})\Lambda(\Sigma^{0})$, provided a comparison with the measurement on helium, and the Λ/Σ^{0} production ratio. This ratio remaining the same for the quasifree production on helium is an assumption that is used to separate the missing mass distribution for Σ^{-}. The reconstructed missing mass was calculated using equation 5.1,

$$M_{Y}^{2} = (\omega + M_{T} - E_{K})^{2} - (\vec{q} - \vec{P}_{K})^{2}. \tag{5.1}$$

The missing mass spectrum for hydrogen at $\theta_{\gamma K} = 0^{o}$ is shown in Figure 5.1. The random coincidence events and the events from the target windows are shown in the shaded regions. The contribution from these events were subtracted to leave sharp Λ and Σ^{0} peaks, the width of each peak is due to the 4 MeV resolution. Figure 5.2 shows the ϕ coverage for each setting. There is full ϕ coverage only at $\theta_{\gamma K} = 0^{o}$.

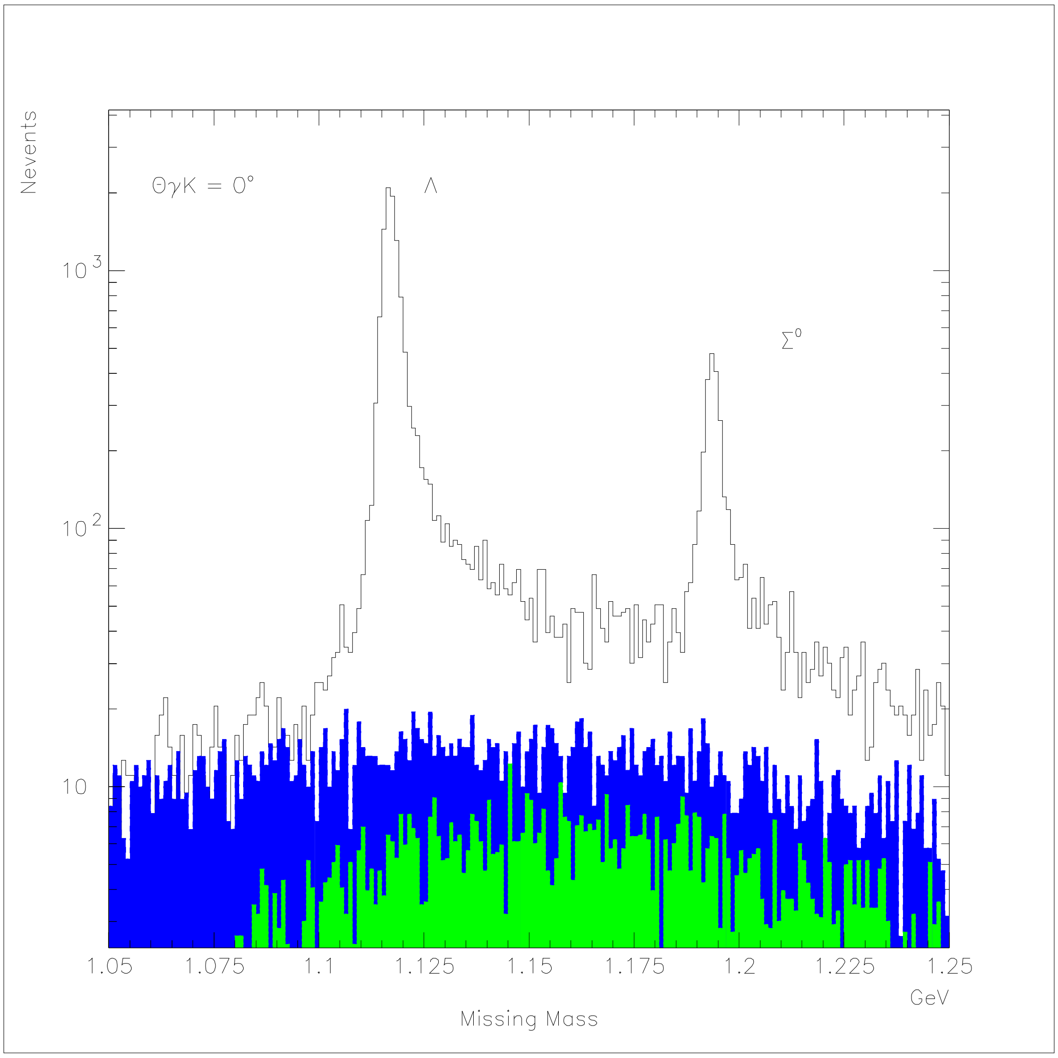

Figure 5.1: Raw missing mass spectrum for p(e,e'K) at $\theta_{\gamma K} = 0^o$. The shaded regions show the random kaon events and the real dummy events.

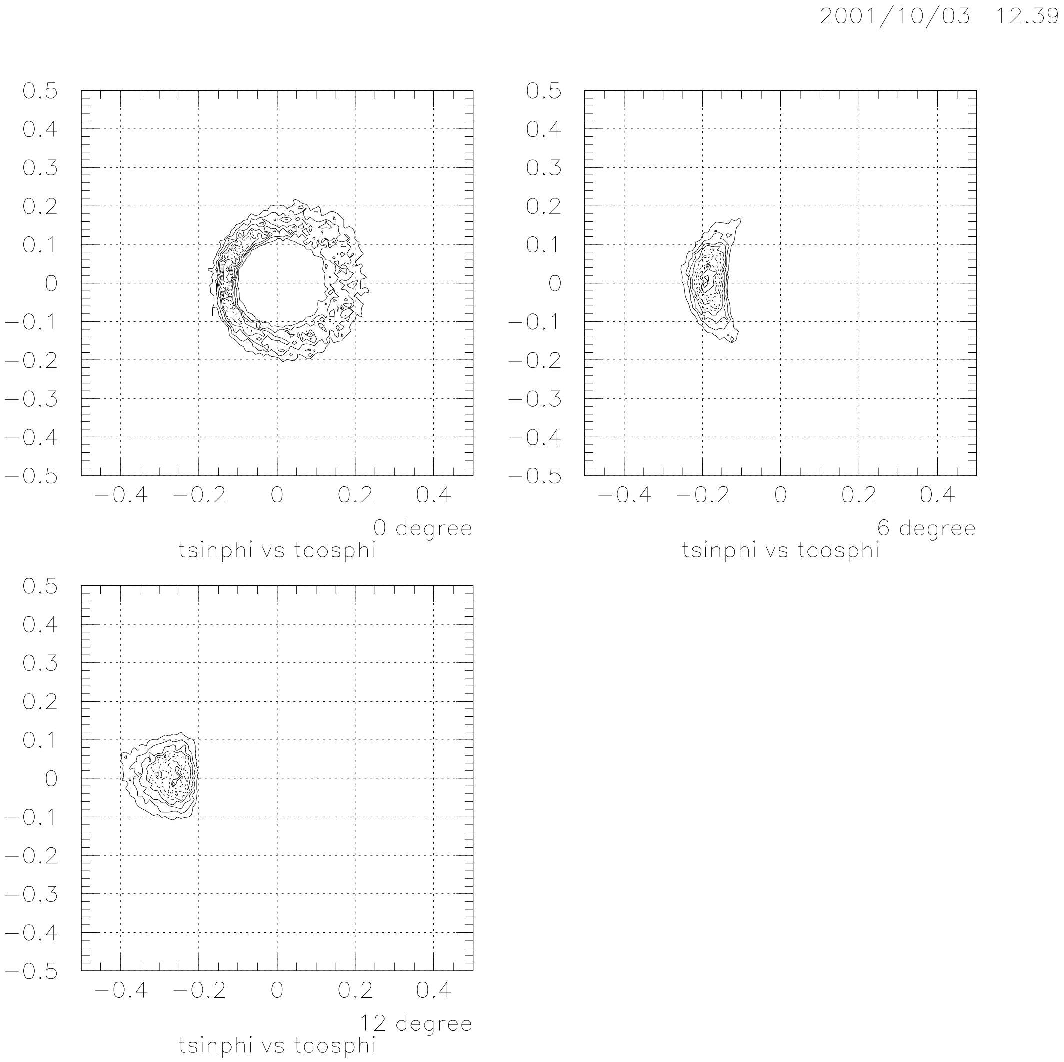

Figure 5.2: ϕ distributions for H(e,e'K)Λ at $\theta_{\gamma K} = 0^o, 6^o$, and 12^o.

Recall that the cross section model for Λ production is the product of independent functions of the kinematic variables $Q^2, W, t,$ and ϕ,

$$\frac{d\sigma}{d\Omega}(Q^2, W, t, \phi) = f(Q^2)g(W)h(t)i(\phi). \tag{5.2}$$

For Σ^0 production, the Monte Carlo simulation used a W-parameterization, $\frac{p_K}{(W^2-M^2)W}$, where p_K is the three momentum of the kaon. Using this parameterization, the simulation was scaled to fit the data, and the center of mass cross section was calculated using

$$\frac{d\sigma}{d\Omega_{(data)}} = \frac{d\sigma}{d\Omega_{(MC)}} FC, \tag{5.3}$$

where $\frac{d\sigma}{d\Omega}(MC)$ is the average center of mass Monte Carlo cross section, F is the scaling factor given by equation 5.4, and C is the particle identification cut correction listed in Table 3.3. The corrections listed in Table 3.4 went into the scaling factor. The scaling factor, F, was found for Λ and Σ^0 at $\theta_{\gamma K} = 0^o, 6^o$, and 12^o.

$$F = \frac{Yield_{data}}{Yield_{MC}}. \tag{5.4}$$

The measurements of $\frac{d\sigma}{d\Omega}$ are listed in Tables 5.1 and 5.2 . The errors include statistical errors and the systematic errors discussed in Chapter 3. The total error is dominated by the systematic error. The increase in $\frac{d\sigma}{d\Omega}$ as $\theta_{\gamma K}$ moves from 0^o to 6^o could indicate a contribution from the interference terms, σ_{LT} and σ_{TT}. However,

$\theta_{\gamma K}$ (deg)	Q^2 (GeV^2)	W (GeV)	t (GeV^2)	$\frac{d\sigma}{d\Omega}$(μb/sr) Λ
0	0.350	1.917	-0.156	0.3969 ± 0.0415
6	0.350	1.917	-0.191	0.4572 ± 0.0510
12	0.348	1.920	-0.284	0.3736 ± 0.0429

Table 5.1: Hydrogen Λ average cross sections at central kinematics. The error includes the systematic errors and statistical error.

$\theta_{\gamma K}$ (deg)	Q^2 (GeV^2)	W (GeV)	t (GeV^2)	$\frac{d\sigma}{d\Omega}$(μb/sr) Σ^0
0	0.340	1.937	-0.200	0.1272 ± 0.0134
6	0.339	1.940	-0.238	0.1635 ± 0.0184
12	0.335	1.950	-0.332	0.1619 ± 0.0193

Table 5.2: Hydrogen Σ^0 average cross sections at central kinematics. The error includes the systematic errors and statistical error.

as $\theta_{\gamma K}$ continues to increase, the contribution from these interference terms could increase much slower relative to the decrease in cross section with respect to t. The Σ^0 has a smaller phase space acceptance than Λ for these kinematics. The overall production ratio of Λ to Σ^0 is about 3:1.

As shown in Figures 5.3, 5.4, and 5.5, the simulation reproduces the data well. The knowledge of the beam energy and spectrometer setting offsets were determined by calibrations. With these offsets applied, the data had to be shifted by $\sim$ 1 MeV to align the sharp Λ and Σ^0 peaks from hydrogen. The same offsets were applied to the ^{3,4}He missing mass spectra so that the energy scale was known within 1 MeV.

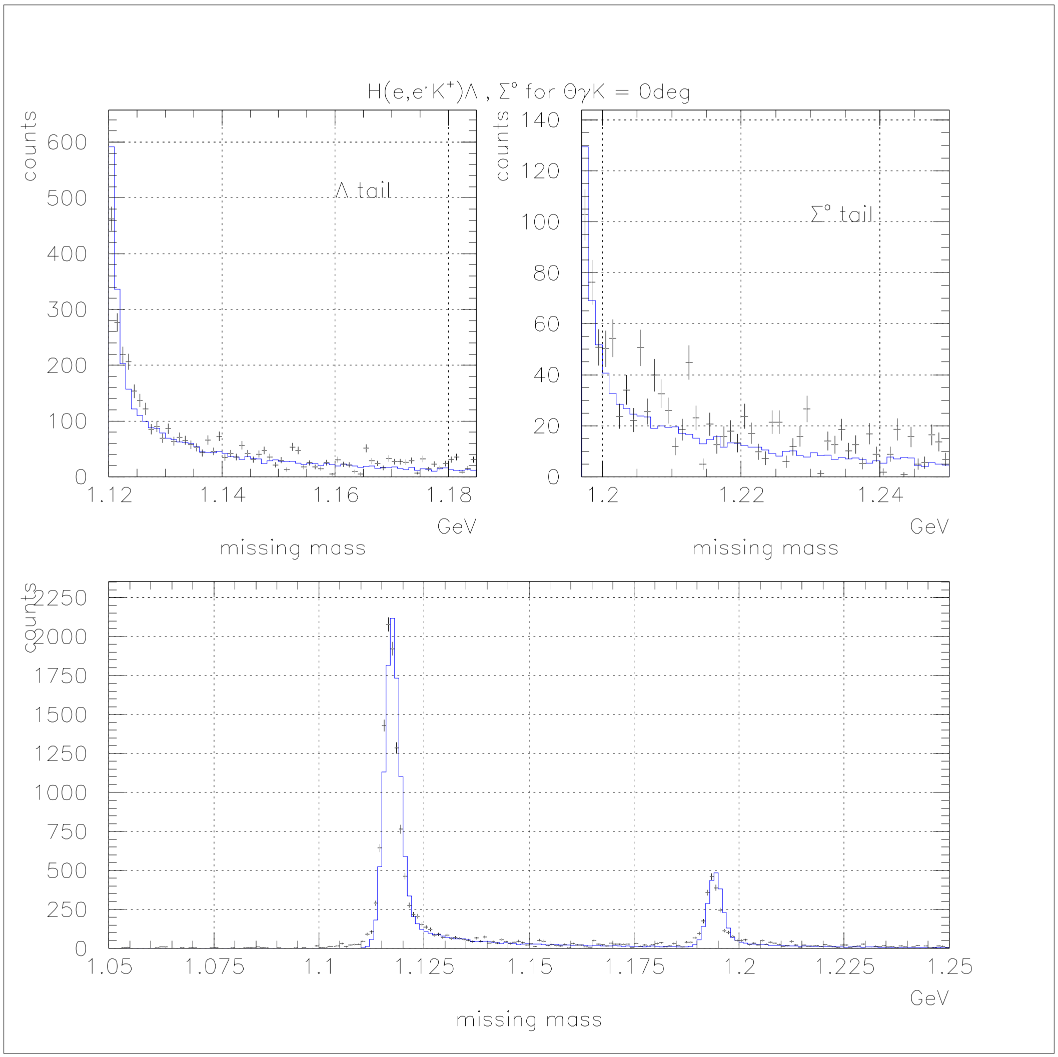

Figure 5.3: Missing mass spectrum for $\theta_{\gamma K} = 0^o$ with MC overlay. The solid line is the Monte Carlo and the data are the points with statistical error bars.

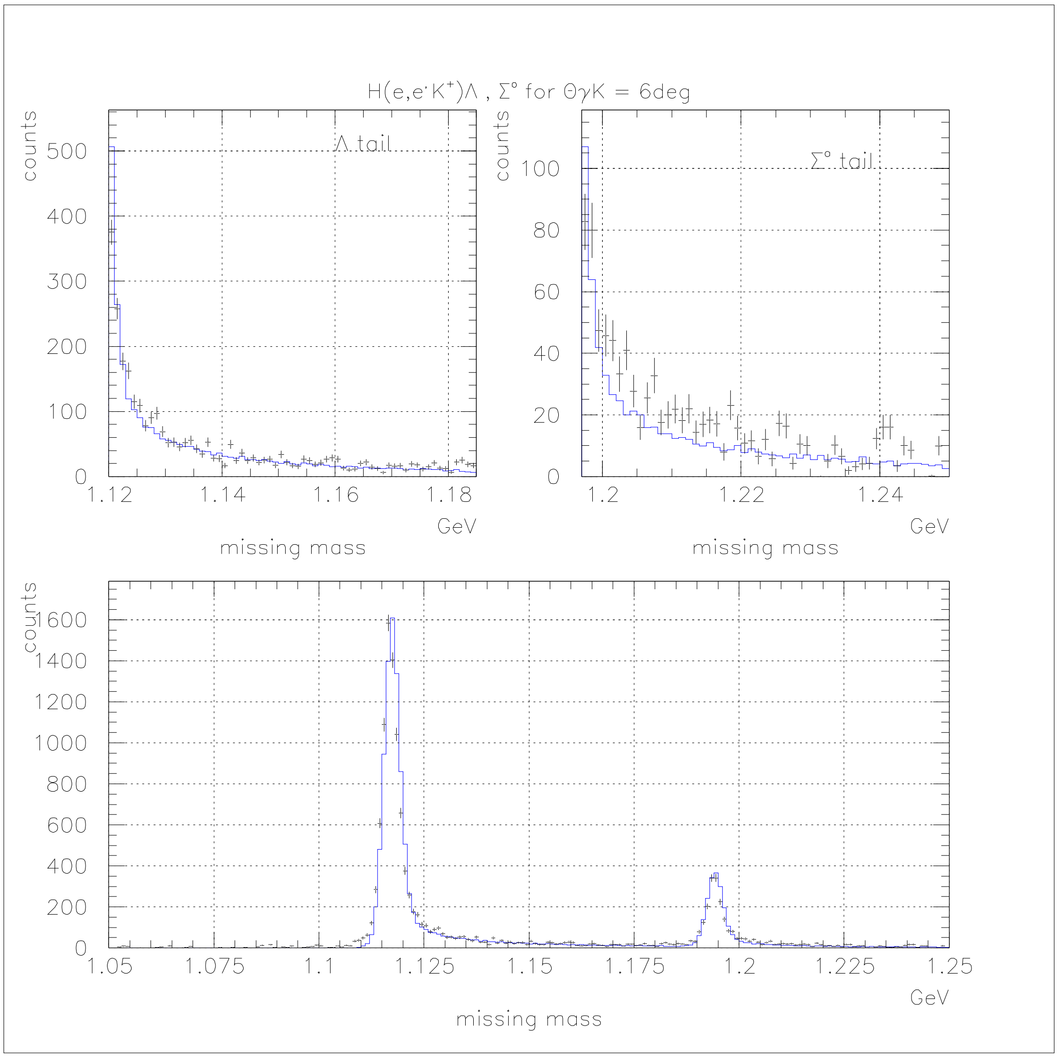

Figure 5.4: Missing mass spectrum for $\theta_{\gamma K} = 6^o$ with MC overlay. The solid line is the Monte Carlo and the data are the points with statistical error bars.

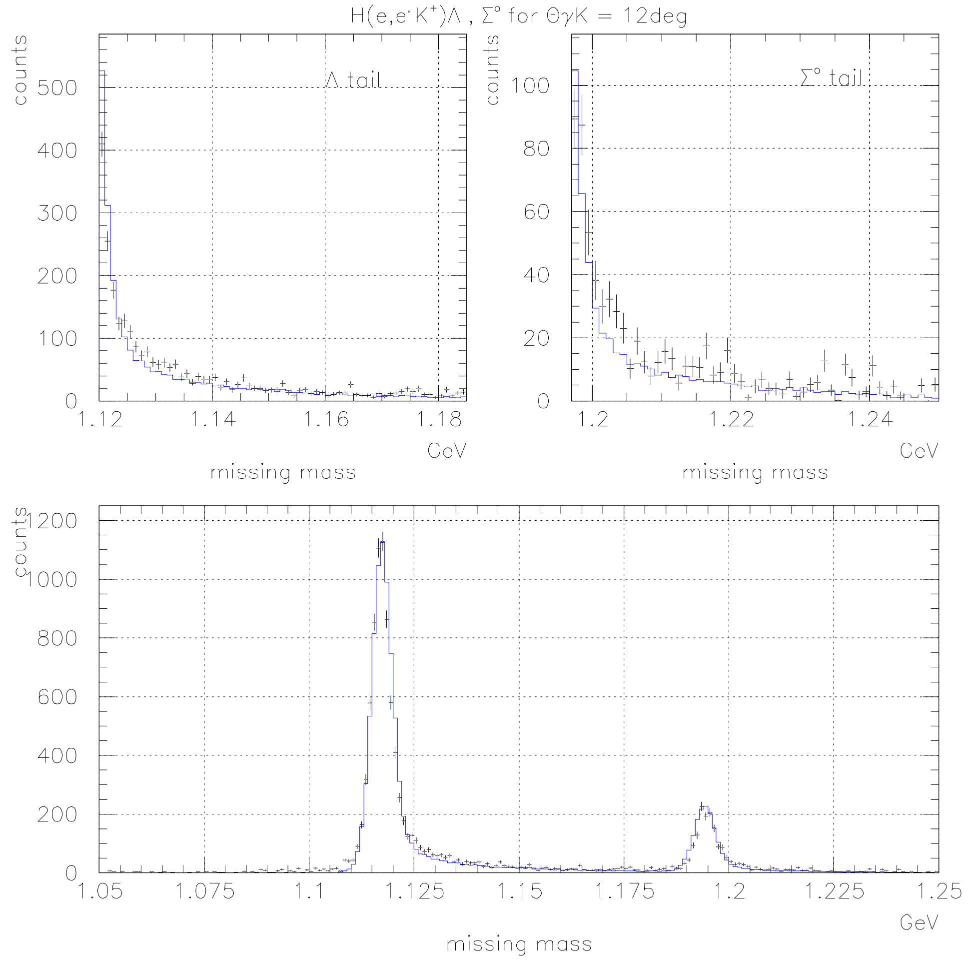

Figure 5.5: Missing mass spectrum for $\theta_{\gamma K} = 12^o$ with MC overlay. The solid line is the Monte Carlo and the data are the points with statistical error bars.

Target	$\theta_{\gamma K}$ (deg)	Q^2 (GeV^2)	W (GeV)	t (GeV^2)
^{3}He	0	0.348	1.929	-0.166
^{3}He	6	0.348	1.929	-0.201
^{3}He	12	0.346	1.933	-0.291
^{4}He	0	0.345	1.935	-0.174
^{4}He	6	0.345	1.936	-0.208
^{4}He	12	0.344	1.941	-0.295

Table 5.3: ^{3}He and ^{4}He central kinematics for Λ production.

Target	$\theta_{\gamma K}$ (deg)	Q^2 (GeV^2)	W (GeV)	t (GeV^2)
^{3}He	0	0.339	1.948	-0.204
^{3}He	6	0.338	1.950	-0.240
^{3}He	12	0.336	1.958	-0.327
^{4}He	0	0.336	1.956	-0.208
^{4}He	6	0.336	1.958	-0.243
^{4}He	12	0.335	1.965	-0.328

Table 5.4: ^{3}He and ^{4}He central kinematics for Σ^0 production.

5.2 ^{3,4}He(e,e'K$^+$)

Data from the ^{3,4}He targets were taken at $\theta_{\gamma K} = 0^o, 6^o$, and 12^o. The central kinematics are listed in Tables 5.3, 5.4, and 5.5. The main differences between the helium and hydrogen target are the inclusion of the Σ^- hyperon, which is produced from the neutron, and the Fermi motion of the nucleons. Final state interactions of the recoil nucleus from helium were also observed. The lambda cross section model was the same as hydrogen with some kinematical differences. In the Monte Carlo, the cross section model for Σ^- was the same as Σ^0. The difference is the 5 MeV mass difference between them. This data were studied using a Monte

Target	$\theta_{\gamma K}$ (deg)	Q^2 (GeV^2)	W (GeV)	t (GeV^2)
^{3}He	0	0.337	1.954	-0.209
^{3}He	6	0.337	1.956	-0.245
^{3}He	12	0.335	1.963	-0.331
^{4}He	0	0.336	1.958	-0.210
^{4}He	6	0.336	1.959	-0.245
^{4}He	12	0.334	1.966	-0.329

Table 5.5: ^{3}He and ^{4}He central kinematics for Σ^- production.

Carlo simulation that included a momentum distribution and a simulation with a full spectral function. In order to extract the Σ^- differential cross section, the assumption was made that the Λ to Σ^0 production ratio measured from hydrogen remained constant for the nuclear targets.

5.2.1 Missing Mass Spectra

The raw missing mass spectra for ^{3}He and ^{4}He are shown in Figures 5.6 and 5.7 with a bin size of 2 MeV. The shaded areas are the contributions from the random coincidences and the target window which had to be subtracted to leave the real coincident kaons. The lambda and sigma peaks are not clearly separated as they are in hydrogen. In ^{3}He, the Σ^0 peak cannot be seen, but is only a broad shoulder above 3.1 GeV in missing mass. In ^{4}He, there is such a huge overlap, the shoulder is no longer present. The sigma region, which includes Σ^0 and Σ^-, contains the large Λ tail which must be subtracted. An overlay of the data for $\theta_{\gamma K} = 0^o, 6^o$, and 12^o shows the position of the lambda peak shifting to a higher missing mass because the increasing angle, $\theta_{\gamma K}$, results in an increasing momentum transfer. This results in the increase of energy of the YN system, which is just a kinematical effect. As $\theta_{\gamma K}$ increases, the overlap of the lambda and sigma region also increases. This is shown in Figure 5.8.

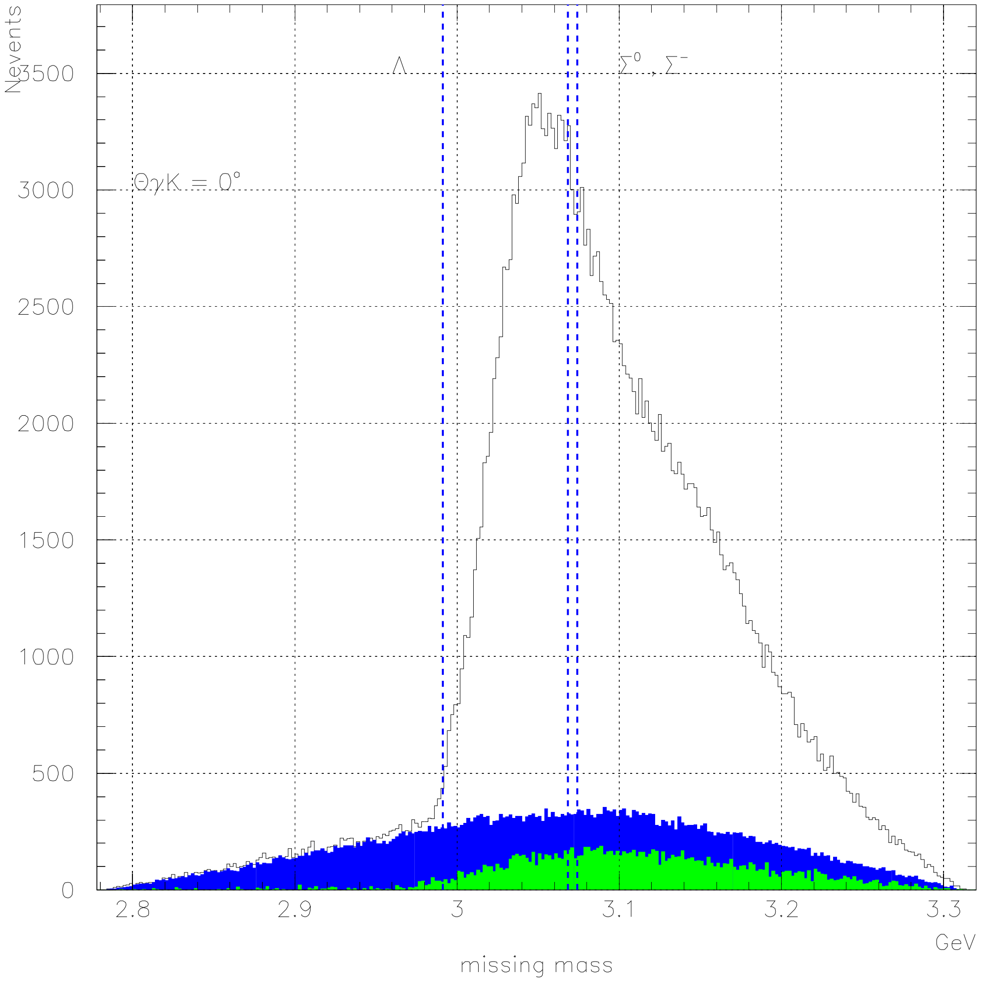

Figure 5.6: ^{3}He missing mass spectrum for $\theta_{\gamma K} = 0^o$. The shaded areas are the random coincidences and the dummy target contributions.

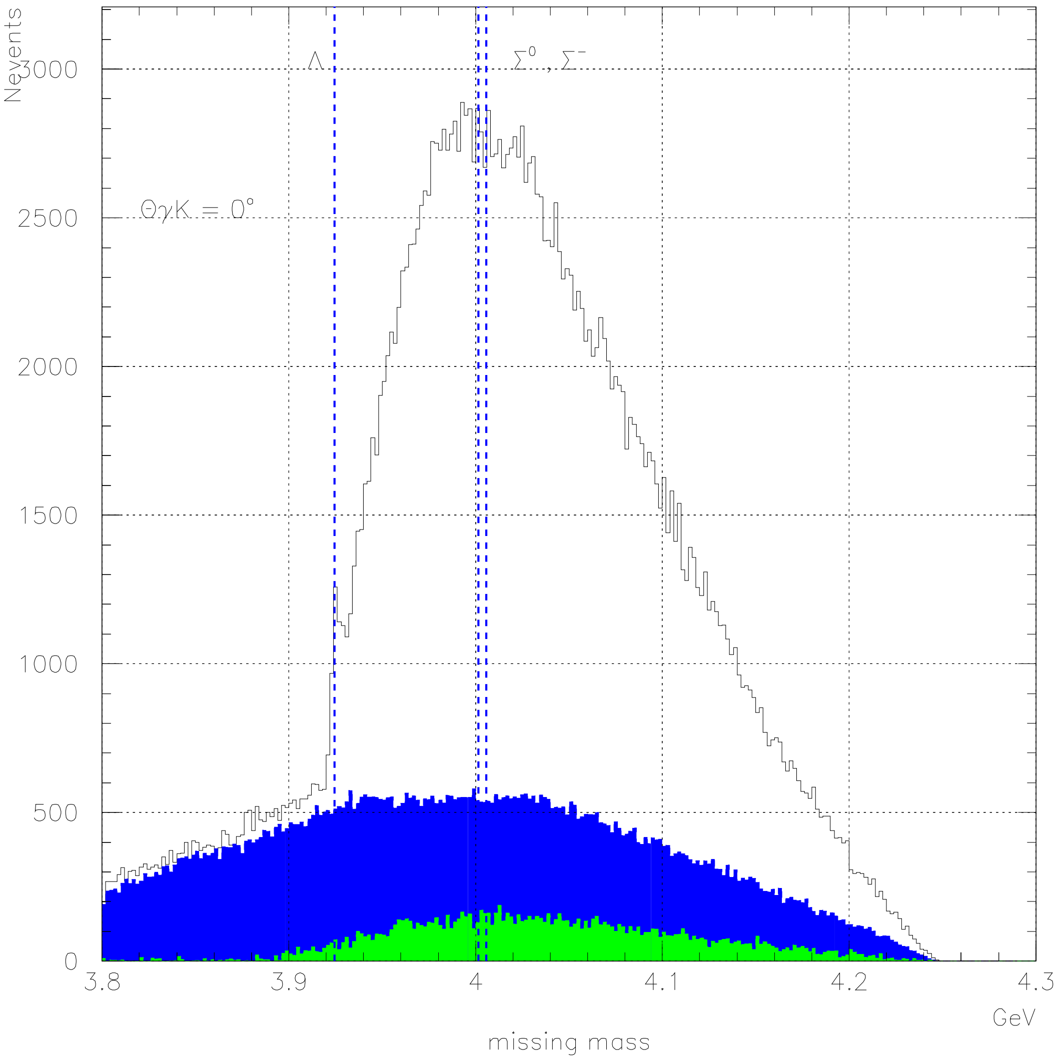

Figure 5.7: ^{4}He missing mass spectrum for $\theta_{\gamma K} = 0^o$. The shaded areas are the random coincidences and the dummy target contributions.

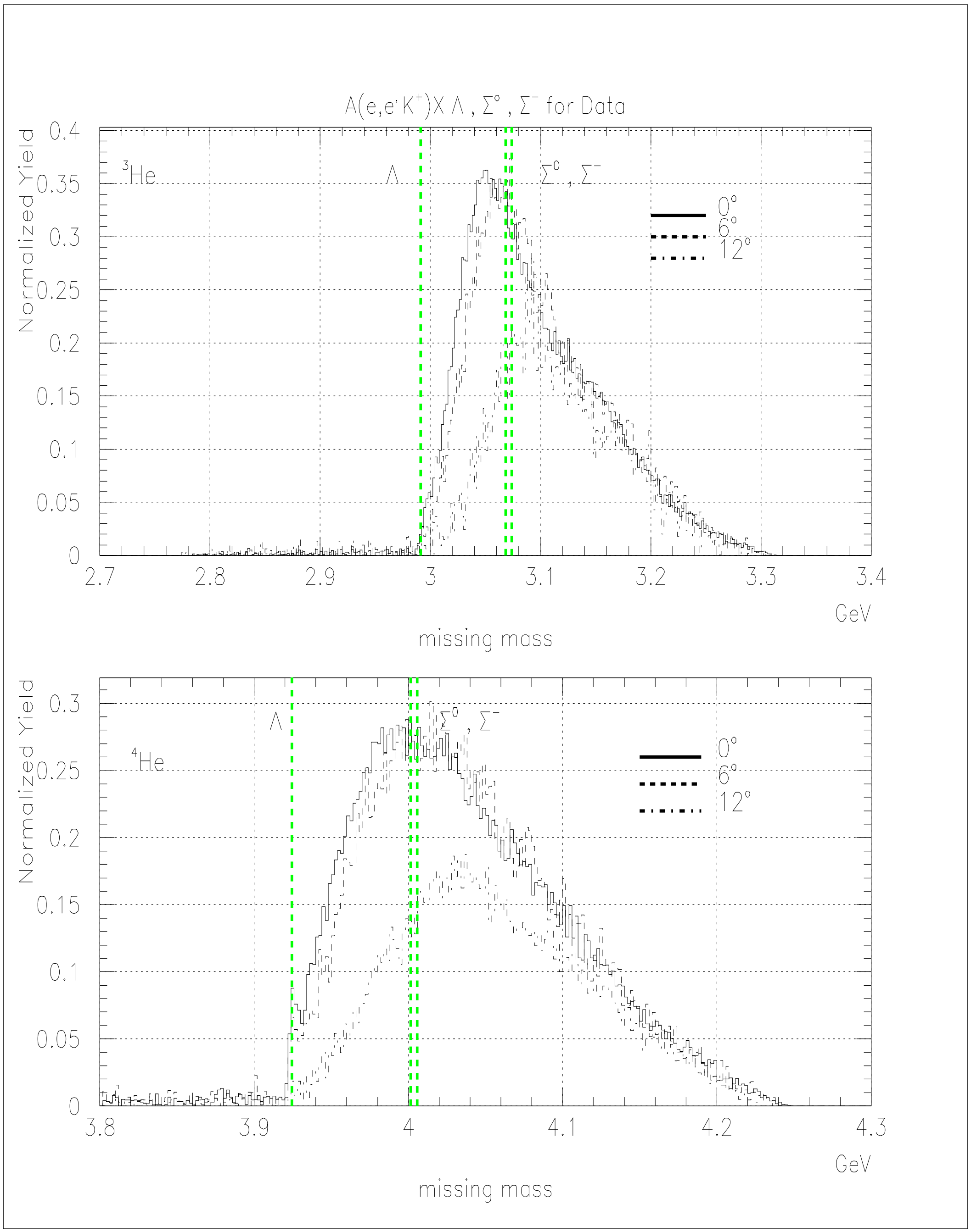

Figure 5.8: ^{3,4}He missing mass spectra for $\theta_{\gamma K} = 0^o, 6^o$, and 12^o. The yields have been normalized to charge and corrected for dead time, tracking, and trigger efficiencies.

5.2.2 Fitting with SIMC

As previously stated, the production of kaons from hydrogen plays an essential role when measuring the quasifree production of kaons on nuclear targets such as ^{3}He and ^{4}He. The Λ to Σ^0 production ratio from the free proton in hydrogen is assumed to remain constant. This is used to understand the Σ^- production from the neutron in the helium targets. Monte Carlo simulations for Λ, Σ^0, and Σ^- were produced and compared with the data. There were fits using simulations from the Atti momentum distributions and simulations using the Benhar full spectral functions. The fitting used a maximum likelihood fit with the constraint that the Λ/Σ^0 ratio is fixed [34]. The fit used fitting ranges between 3.027-3.060 GeV and 3.130-3.290 GeV for Λ and Σ^- on ^{3}He. For ^{4}He, the fit ranges were between 3.957-3.995 GeV and 4.03-4.23 GeV for Λ and Σ^-, respectively. The upper limit on Λ was chosen to be below the Σ^0 threshold. These fitting ranges were chosen to exclude the threshold regions because the model does not include final state interactions. The high missing mass regions were also excluded due to other reaction channels that are not described by the model. The fit determined the scaling factors for the Λ and Σ^- distribution over the given missing mass range. The average cross section over the full acceptance for each $\theta_{\gamma K}$ was calculated using equation 5.3. The Σ^- cross section depended heavily on how well the Λ distribution was modeled. Because of the large overlap of the Λ tail in the Σ region, a 1% error in fitting the Λ tail would cause a 3% - 18% difference in the Σ^- cross section. Due to the low statistics in the Σ^- distribution for ^{3}He at $\theta_{\gamma K} = 12^o$ and ^{4}He at $\theta_{\gamma K} = 6^o$ and 12^o in SIMC2, the fitting routine failed, giving negative values in some cases. For these particular settings, a simple scaling method was used to determine the cross section in which the scaling factor was determined by comparing the data yield to the simulation yield over a given range in missing mass. The error on those points were dominated by the statistical error.

The missing mass spectra at each $\theta_{\gamma K}$ setting for each simulation are shown in Figures 5.9 through 5.20 for both the ^{3}He and ^{4}He targets. The Monte Carlo is the solid line and the data are the points with statistical error bars. The simulation containing only the momentum distribution is labeled SIMC1, while the full spectral function is called SIMC2. The simulations do not include final state interactions. The excess in cross section seen near lambda threshold is presumed to be from ΛN and NN interactions. The ^{4}He missing mass distribution shows a possible Λ bound state for the $\theta_{\gamma K} = 0^o$ and 6^o data which should appear at 3.923 GeV for the ground state and 3.924 GeV for the first excited state.

The Atti momentum distributions seem to be in good agreement with the data for ^{3}He and ^{4}He. However, it is more narrow than the data at the peak surrounding Σ^0 threshold. The simulation with the spectral functions slightly overshoots the ^{4}He data from 4.04-4.07 GeV, but the width of the peak is in better agreement for the ^{3}He and ^{4}He simulations because perhaps a better description of the sigma region is modeled. Ideally, the spectral function should give a better description of the shape of the missing mass spectra because it contains more information regarding the momentum and the excitation energy of the struck nucleon.

Tables 5.6 and 5.7 list the cross section results measured from the simulations using the Atti momentum distribution (SIMC1) and the Benhar spectral functions (SIMC2). For ^{3}He, the largest disagreement between SIMC1 and SIMC2 is with the Σ^- cross sections for $\theta_{\gamma K} = 0^o$. The Λ and Σ^0 for all other settings on ^{3}He and ^{4}He agree within $\sim$ 10% - 12%. For ^{4}He, there is a 38% difference in the results obtained for the Σ^- at $\theta_{\gamma K} = 0^o$. Perhaps the measured cross sections can only be known within the percent difference of both simulations. Because there is still more to be understood about the modeling of kaon electroproduction on ^{3}He and ^{4}He, this analysis will show the results obtained from using both the momentum distribution and the full spectral function.

$\theta_{\gamma K}$	$\frac{d\sigma}{d\Omega}(\mu\text{b/sr})\ \Lambda$	$\frac{d\sigma}{d\Omega}(\mu\text{b/sr})\ \Sigma^0$	$\frac{d\sigma}{d\Omega}(\mu\text{b/sr})\ \Sigma^-$
SIMC1			
0	0.3806 ± 0.0232	0.1236 ± 0.0076	0.1526 ± 0.0208
6	0.4224 ± 0.0276	0.1575 ± 0.0105	0.0800 ± 0.0133
12	0.3546 ± 0.0291	0.1563 ± 0.0138	0.0796 ± 0.0142
SIMC2			
0	0.4165 ± 0.0255	0.1374 ± 0.0085	0.0979 ± 0.0134
6	0.4476 ± 0.0288	0.1647 ± 0.0107	0.0913 ± 0.0152
12	0.3767 ± 0.0311	0.1672 ± 0.0150	0.0898 ± 0.0376

Table 5.6: ^{3}He Λ, Σ^0, and Σ^- cross sections at central kinematics. The central kinematics are listed in Tables 5.3, 5.4, and 5.5. The error includes the systematic errors and statistical error.

$\theta_{\gamma K}$	$\frac{d\sigma}{d\Omega}(\mu\text{b/sr})\ \Lambda$	$\frac{d\sigma}{d\Omega}(\mu\text{b/sr})\ \Sigma^0$	$\frac{d\sigma}{d\Omega}(\mu\text{b/sr})\ \Sigma^-$
SIMC1			
0	0.3364 ± 0.0208	0.1090 ± 0.0085	0.0801 ± 0.0123
6	0.3749 ± 0.0243	0.1396 ± 0.0117	0.0428 ± 0.0072
12	0.3158 ± 0.0245	0.1415 ± 0.0102	0.0404 ± 0.0073
SIMC2			
0	0.3559 ± 0.0219	0.1175 ± 0.0075	0.0583 ± 0.0087
6	0.4099 ± 0.0336	0.1507 ± 0.0099	0.0520 ± 0.0129
12	0.3462 ± 0.0245	0.1561 ± 0.0110	0.0596 ± 0.0169

Table 5.7: ^{4}He Λ, Σ^0, and Σ^- cross sections at central kinematics. The central kinematics are listed in Tables 5.3, 5.4, and 5.5. The error includes the systematic errors and statistical error.

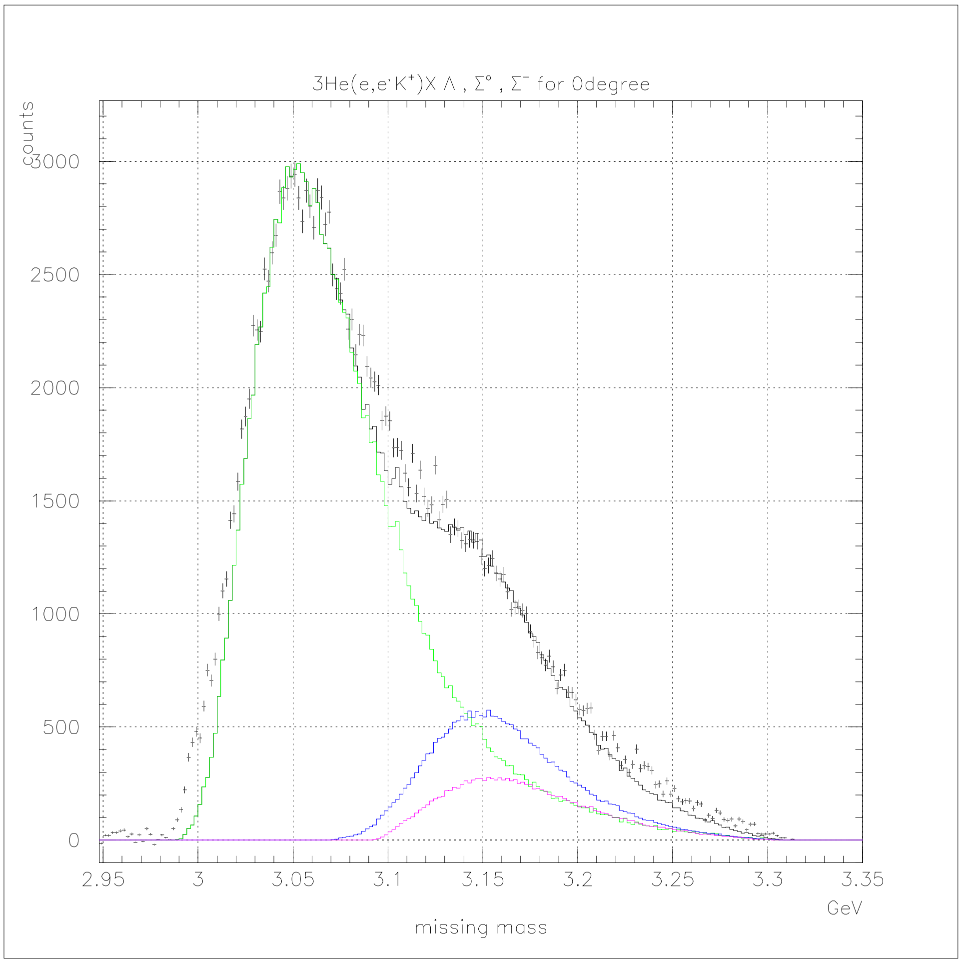

Figure 5.9: The ^{3}He(e,e'K$^+$)YN missing mass at $\theta_{\gamma K} = 0^o$ and SIMC1. The solid lines are of the Λ, Σ^0, and Σ^- scaled simulations and the sum.

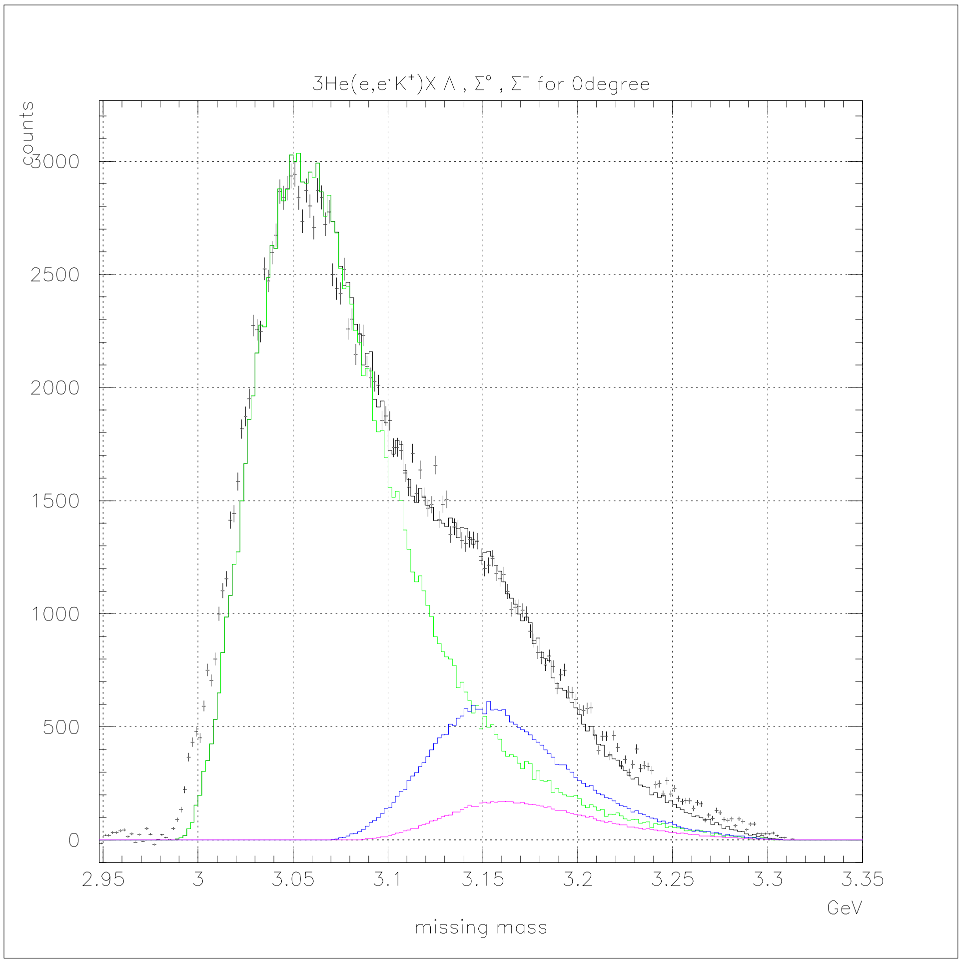

Figure 5.10: The ^{3}He(e,e'K$^+$)YN missing mass at $\theta_{\gamma K} = 0^o$ and SIMC2. The solid lines are of the Λ, Σ^0, and Σ^- scaled simulations and the sum.

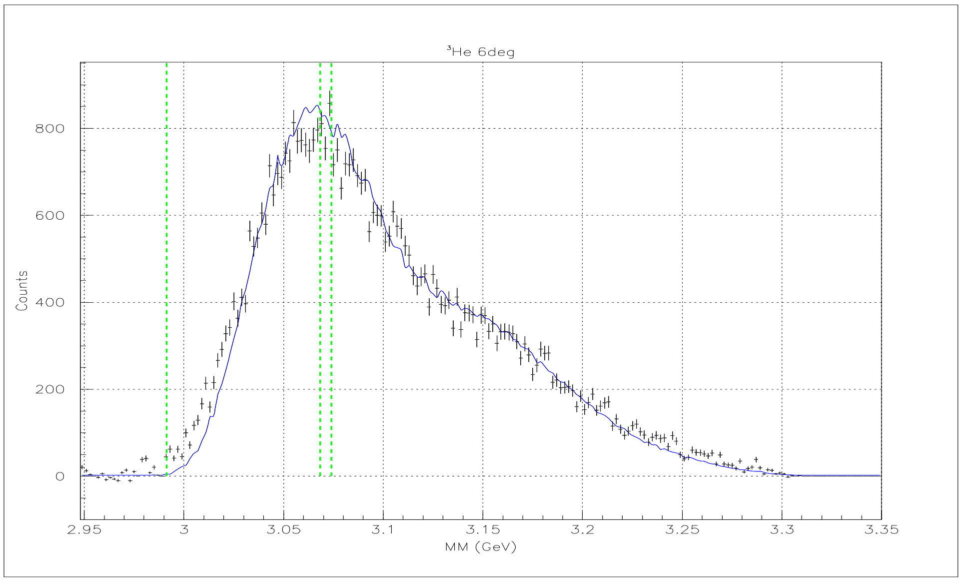

Figure 5.11: The ^{3}He(e,e'K$^+$)YN missing mass at $\theta_{\gamma K} = 6^o$ and SIMC1. The solid line is the sum of the Λ, Σ^0, and Σ^- scaled simulations.

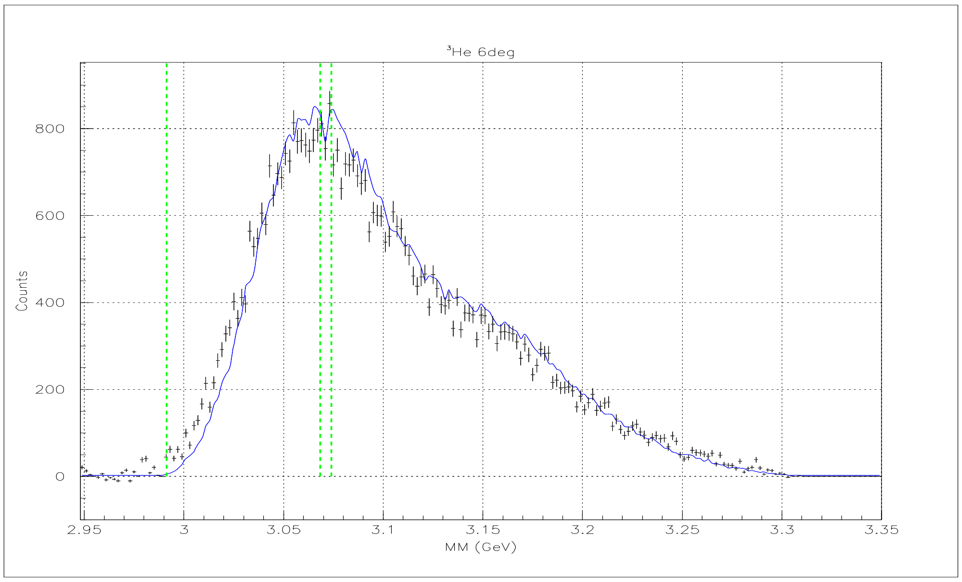

Figure 5.12: The ^{3}He(e,e'K$^+$)YN missing mass at $\theta_{\gamma K} = 6^o$ and SIMC2. The solid line is the sum of the Λ, Σ^0, and Σ^- scaled simulations.

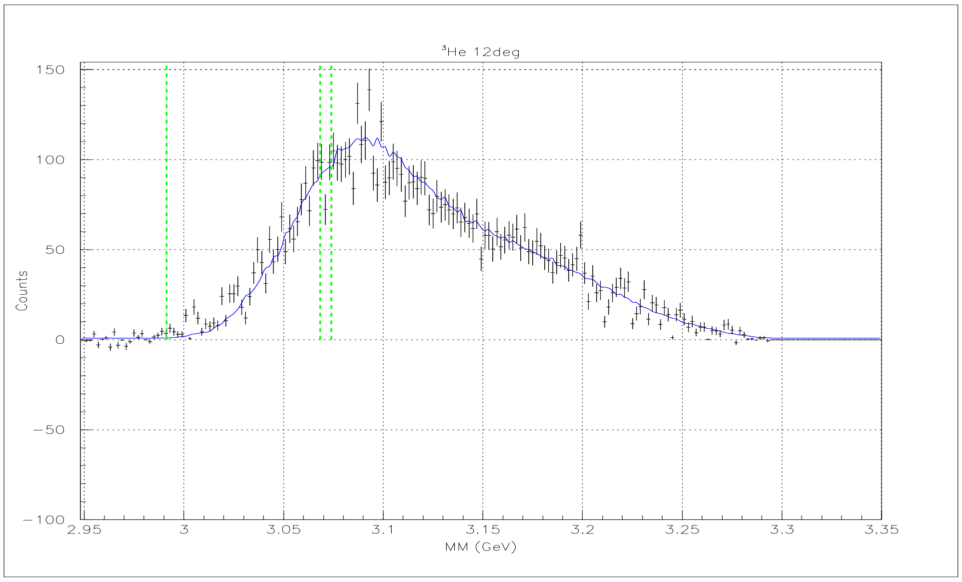

Figure 5.13: The ^{3}He(e,e'K$^+$)YN missing mass at $\theta_{\gamma K} = 12^o$ and SIMC1. The solid line is the sum of the Λ, Σ^0, and Σ^- scaled simulations.

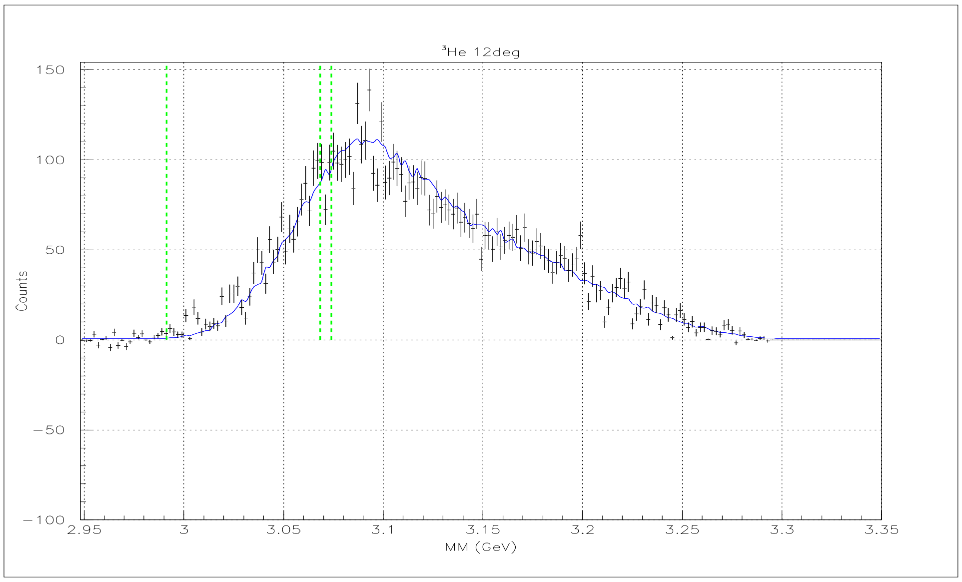

Figure 5.14: The ^{3}He(e,e'K$^+$)YN missing mass at $\theta_{\gamma K} = 12^o$ and SIMC2. The solid line is the sum of the Λ, Σ^0, and Σ^- scaled simulations.

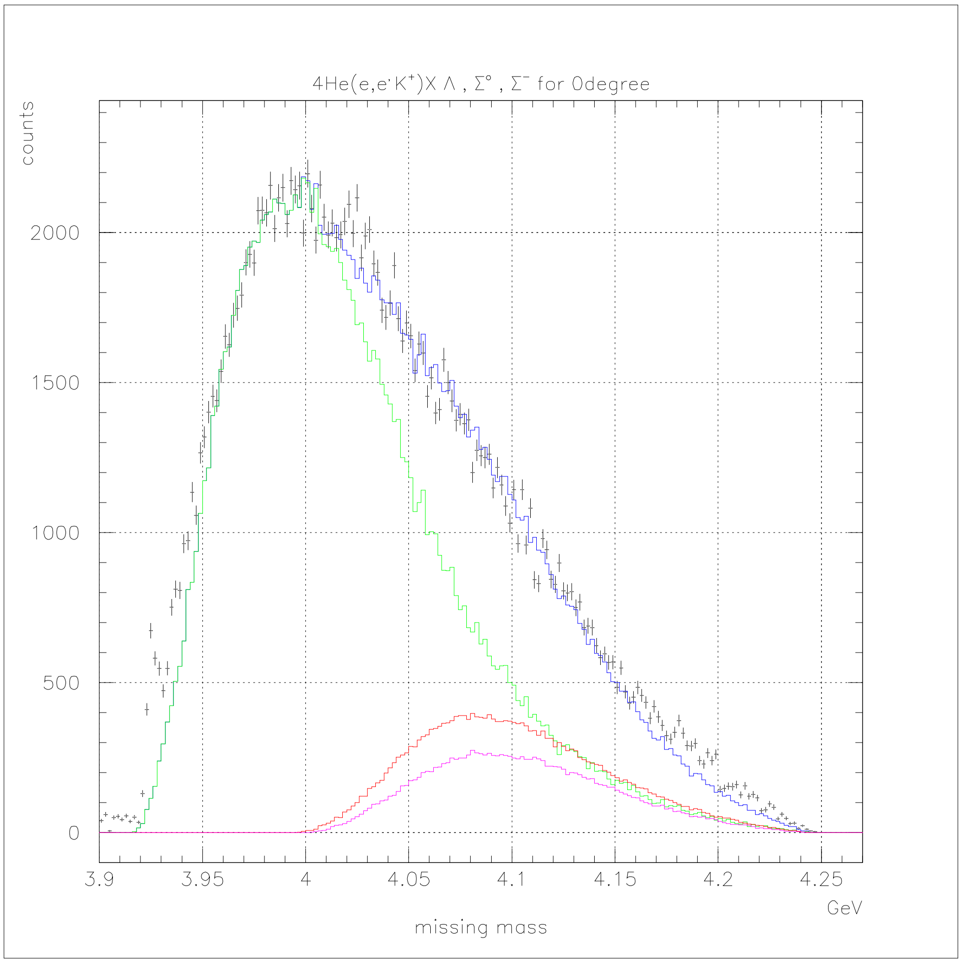

Figure 5.15: The ^{4}He(e,e'K$^+$)YN missing mass at $\theta_{\gamma K} = 0^o$ and SIMC1. The solid lines are of the Λ, Σ^0, and Σ^- scaled simulations and the sum.

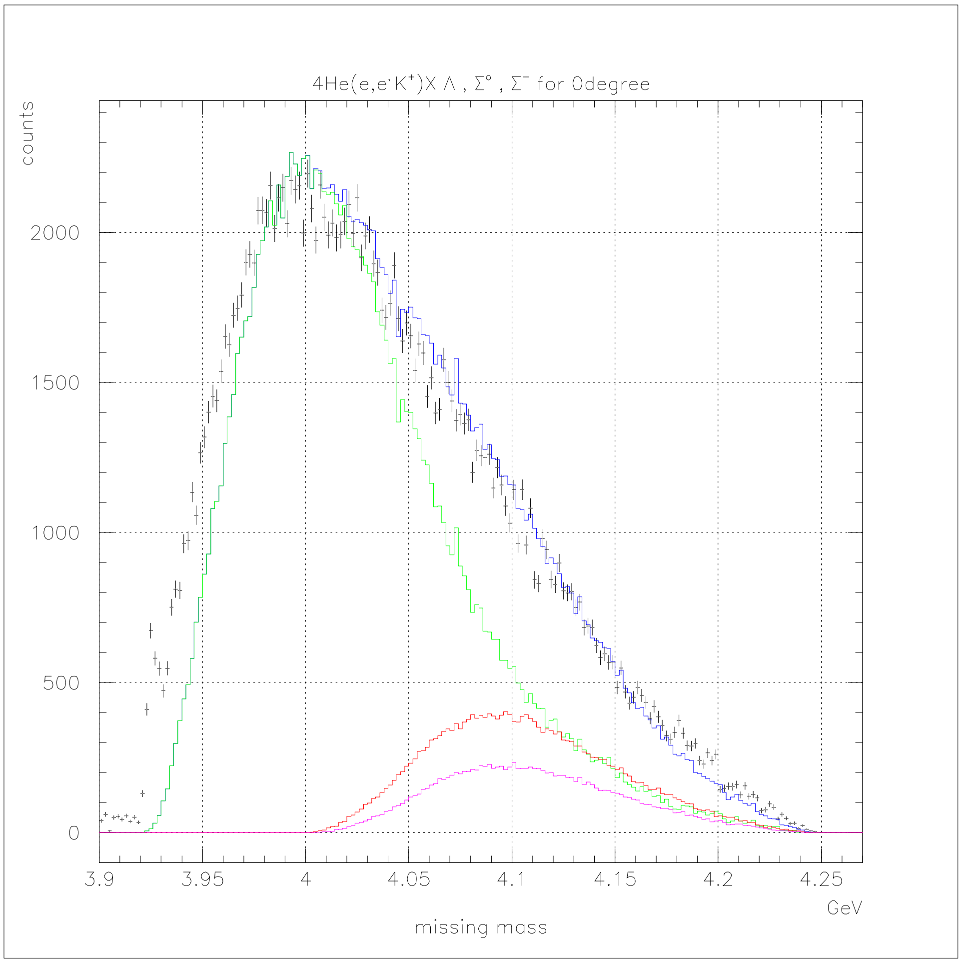

Figure 5.16: The ^{4}He(e,e'K$^+$)YN missing mass at $\theta_{\gamma K} = 0^o$ and SIMC2. The solid lines are of the Λ, Σ^0, and Σ^- scaled simulations and the sum.

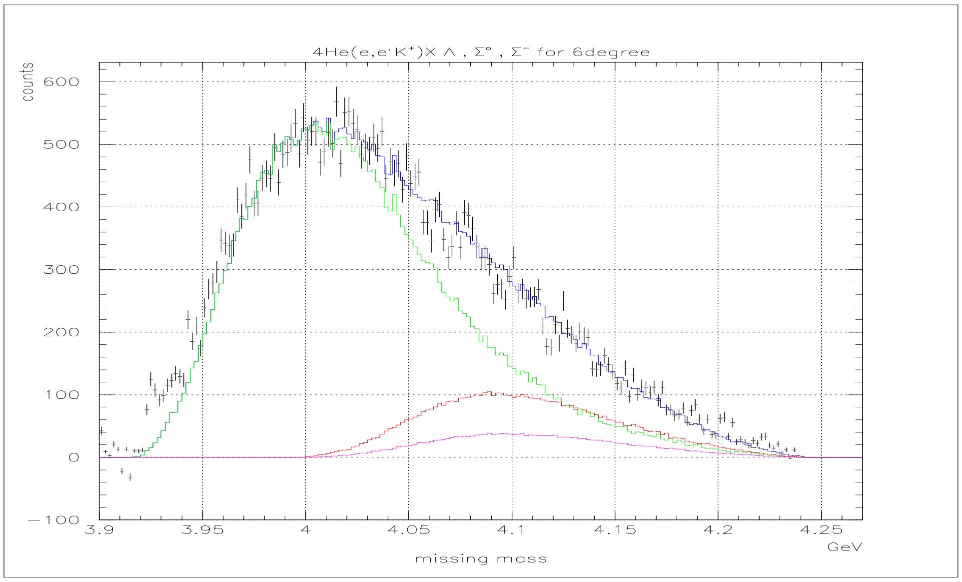

Figure 5.17: The ^{4}He(e,e$'$K^{+})YN missing mass at $\theta_{\gamma K} = 6^{o}$ and SIMC1. The solid lines are of the Λ, Σ^{0}, and Σ^{-} scaled simulations and the sum.

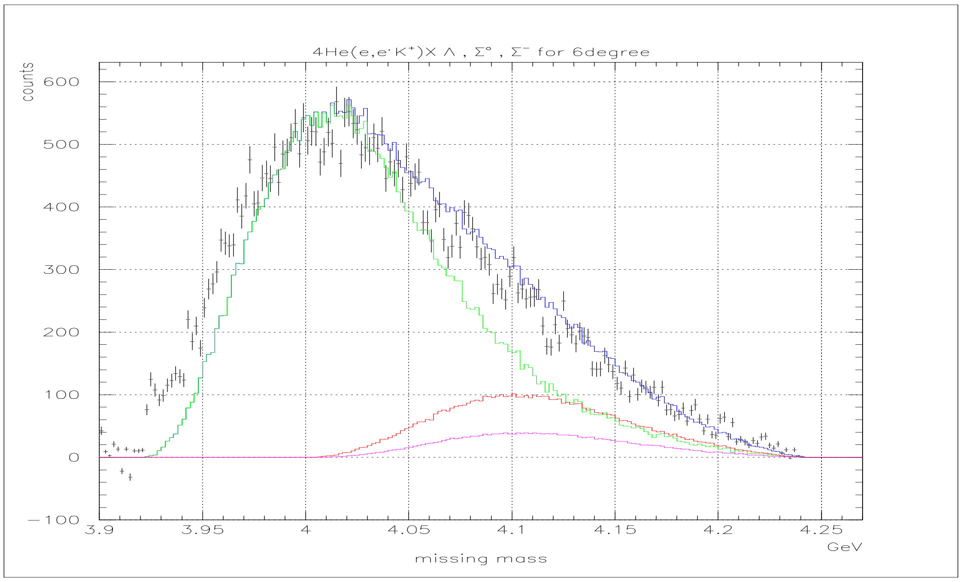

Figure 5.18: The ^{4}He(e,e$'$K^{+})YN missing mass at $\theta_{\gamma K} = 6^{o}$ and SIMC2. The solid lines are of the Λ, Σ^{0}, and Σ^{-} scaled simulations and the sum.

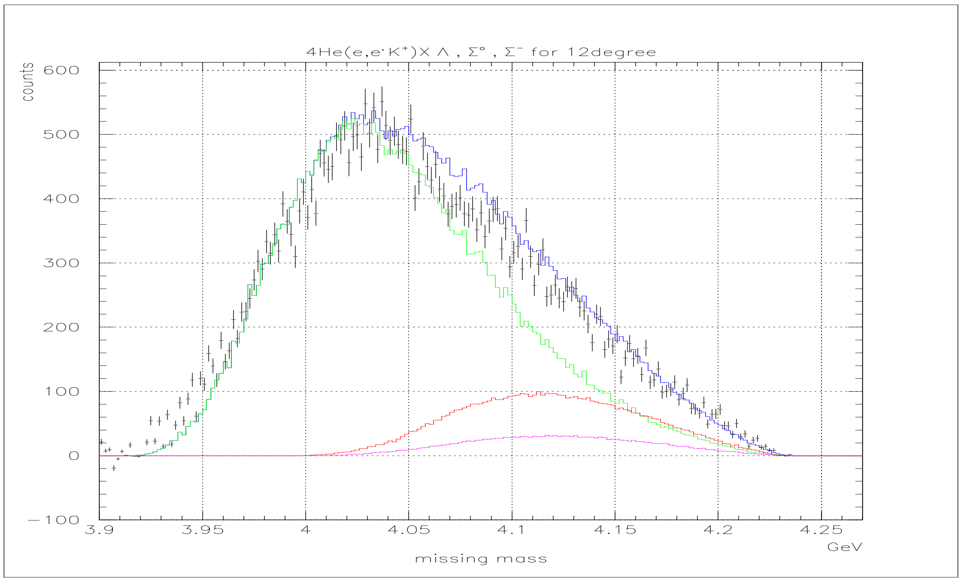

Figure 5.19: The ^{4}He(e,e'K^{+})YN missing mass at $\theta_{\gamma K} = 12^{o}$ and SIMC1. The solid lines are of the Λ, Σ^{0}, and Σ^{-} scaled simulations and the sum.

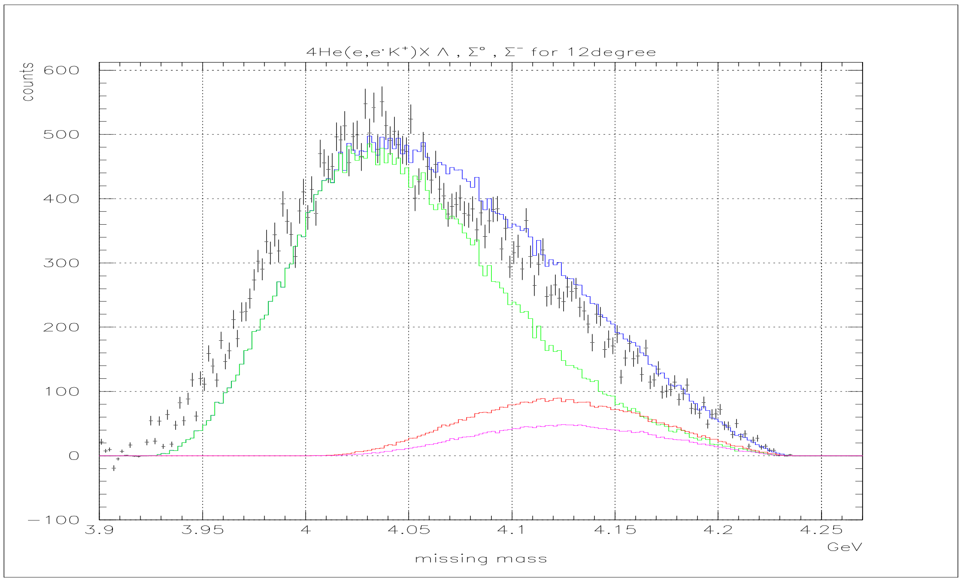

Figure 5.20: The ^{4}He(e,e'K^{+})YN missing mass at $\theta_{\gamma K} = 12^{o}$ and SIMC2. The solid lines are of the Λ, Σ^{0}, and Σ^{-} scaled simulations and the sum.

5.3 Deuterium

Although the main focus of **E91-016** was to study quasifree kaon electroproduction on ^{3}He and ^{4}He targets, deuterium data were also taken at $\theta_{\gamma K} = 0^o$. Deuterium was analyzed in much greater detail during the previous **E91-016** in 1996 [11] [13]. Hydrogen has only a proton which gives the elementary cross section for Λ and Σ^0. Deuterium has the addition of one neutron from which the elementary Σ^- cross section was extracted. The same assumption was made that the Λ/Σ^0 production ratio from hydrogen remained constant for nuclear targets. Using the same fitting procedure as for helium, the scaling factors for Λ, Σ^0, and Σ^- were extracted and the center-of-mass cross sections were determined. The results are shown in Table 5.8. Figure 5.21 shows the missing mass spectrum for deuterium at $\theta_{\gamma K} = 0^o$. The Λ and Σ peaks are clearly distinguishable although the Σ region has a large contribution from the Λ tail which must be subtracted. The Monte Carlo has to include the Fermi motion of the bound proton and neutron. The deuteron wave function from the Bonn potential was used to determine the initial momentum distributions of the struck nucleon. Final state interactions were not included in the Monte Carlo simulation.

$\theta_{\gamma K} = 0^o$	Q^2 (GeV^2)	W (GeV)	t (GeV^2)	$\frac{d\sigma}{d\Omega}$(μb/sr)
Λ	0.348	1.923	-0.162	0.3412 ± 0.0321
Σ^0	0.339	1.943	-0.202	0.1119 ± 0.0124
Σ^-	0.338	1.944	-0.204	0.0619 ± 0.0071

Table 5.8: ^{2}H Λ, Σ^0, and Σ^- cross sections at central kinematics. The error includes the systematic errors and statistical error.

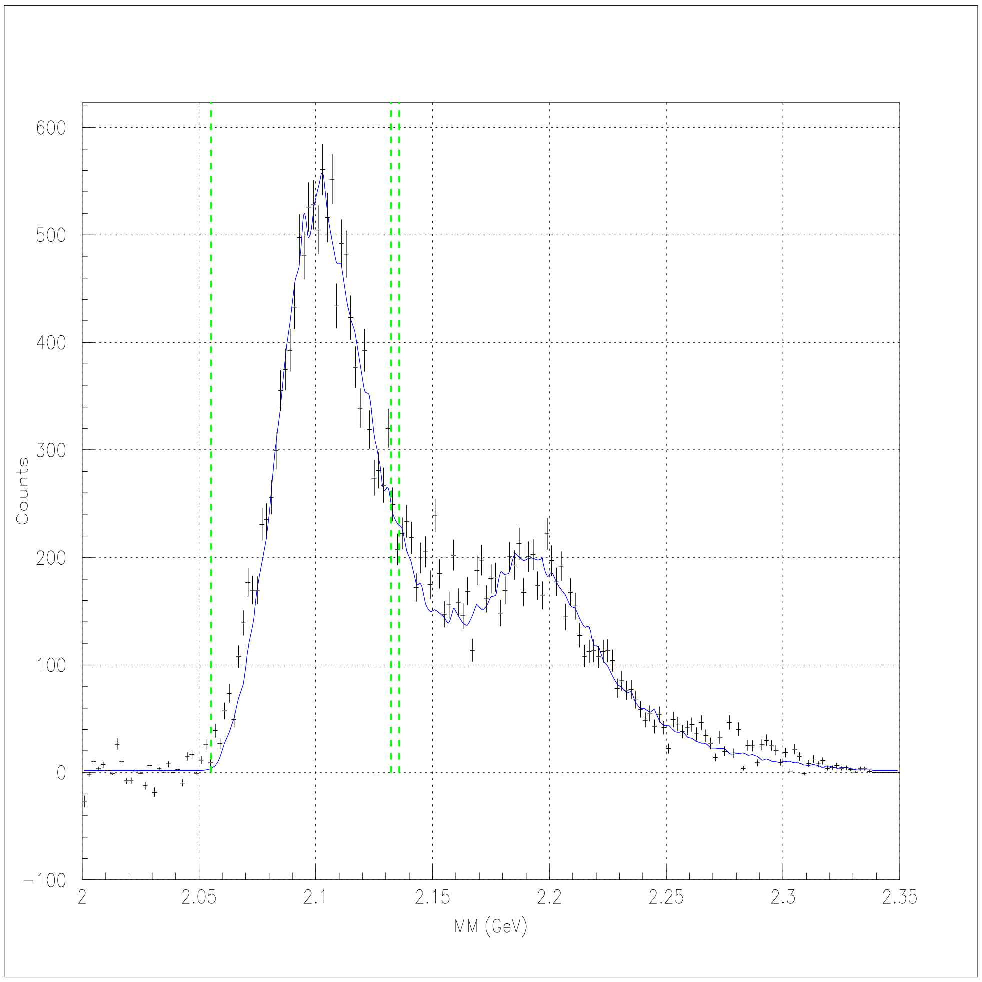

Figure 5.21: The ^{2}H(e,e'K$^+$)YN missing mass at $\theta_{\gamma K} = 0^o$. The solid line is the sum of the Λ, Σ^0, and Σ^- scaled simulations. The vertical dashed lines represent the threshold production for each hyperon.

5.4 Angular Distribution

The angular dependence of the cross sections for Λ, Σ^0, and Σ^- was studied for all four targets. Recall the settings were $\theta_{\gamma K} = 0^o, 6^o$, and 12^o, and deuterium data only at $\theta_{\gamma K} = 0^o$. Figures 5.22 and 5.23 display the angular distribution for each target for the Λ and Σ^- channels. The possible contribution of the interference terms can be seen in Λ with the increase in the cross section at the 6^o setting, and the decrease with at the 12^o setting. The Σ^- and Σ^0 show no angular dependence. Once the simulation for Λ and Σ^0 are fit, everything that is left is fit as Σ^-. The resulting distribution would possibly contain final states that were not modeled in the simulation. This could result in an enhanced scaling factor for Σ^-. However, the cross section for Σ^- would be lower than expected if the resulting Λ and Σ^0 fits were scaled too high. As $\theta_{\gamma K}$ increased, the full missing mass spectrum had less well-defined structure in the Σ region, so the overall fit for each hyperon distribution was in better agreement. If ^{4}He is just viewed as two deuterium, the cross section results would be expected to be similar to those of deuterium. The results for $\frac{d\sigma}{d\Omega(CM)}$ for Λ, Σ^0, and Σ^- on both the ^{3}He and ^{4}He targets will be studied more closely by comparing the results to those of hydrogen.

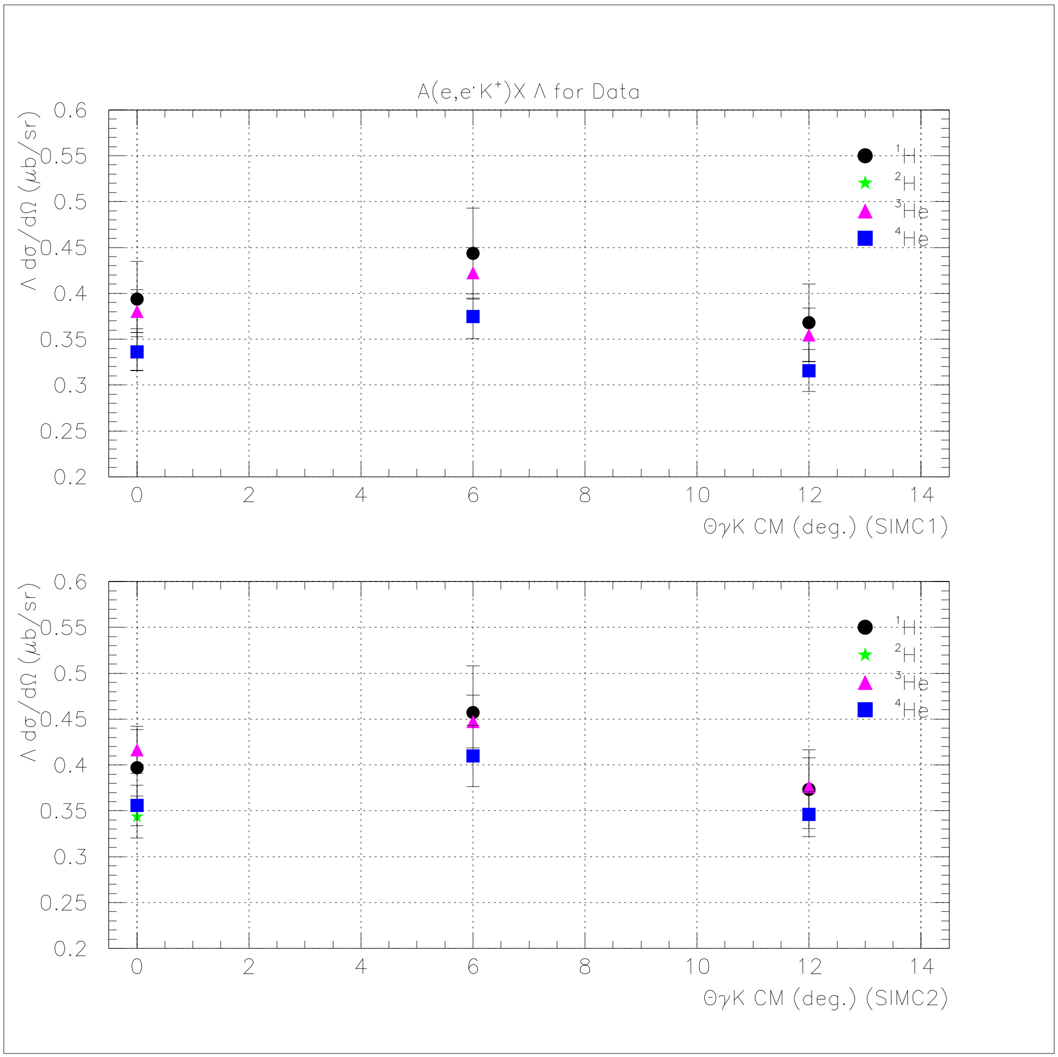

Figure 5.22: Cross sections for A$(e, e'K^+)\Lambda$N. The symbols represent each target.

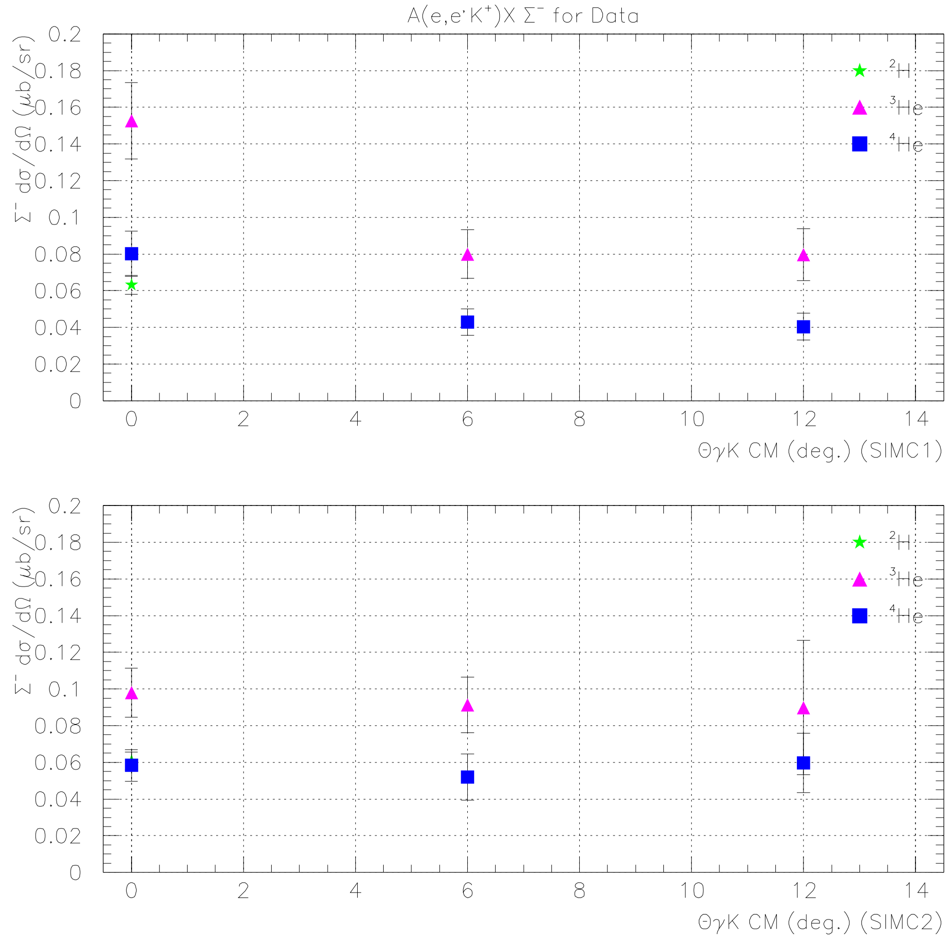

Figure 5.23: Cross sections for A$(e, e' K^+)\Sigma^-$N. The symbols represent each target.

5.5 Cross Section Ratios

Ratios of the cross sections, Λ/Σ^0 and Σ^0/Σ^-, were calculated for this data. Recall that the Σ^0 cross section was measured only on hydrogen. The Σ^0 on the deuterium and helium targets were calculated according to the Λ/Σ^0 ratio from hydrogen. The **E91-016** in 1996 data has shown the Λ/Σ^0 ratio to be $\sim$ 3:1 for $\theta_{\gamma K} = 1.5^o$ at $Q^2 = 0.38$ GeV^2 [11]. This hydrogen data are consistent with previous results at the similar kinematic settings. The Σ^-/Σ^0 cross section ratio averaged 0.61 for the previous data on deuterium. This ratio shows that there is more Σ^0 contributing to the total Σ cross section. These results yield an average of 0.407 ± 0.11 for ^{4}He and 0.60 ± 0.18 for ^{3}He using the spectral function. The ^{3}He ratio for those settings is consistent with previous data, while the ^{4}He ratio is lower. The results of SIMC1 and SIMC2 are shown in Table 5.9 for each target. For $\theta_{\gamma K} = 0^o$, the Σ^-/Σ^0 ratios vary significantly from ^{3}He to ^{4}He depending upon the use of the Atti momentum distribution (SIMC1) or the Benhar spectral function (SIMC2). The lack of a better fit for the ^{3}He in the region beyond sigma threshold at this setting for SIMC1 could explain these odd results. The spectral function in SIMC2 yields results for the Σ^-/Σ^0 which are in better agreement with the previous and present deuterium data. Assuming the cross section is dominated by pure t-channel isospin-$\frac{1}{2}$ exchange, the ratio of Σ^-/Σ^0 has an expected value of 3.0. The Σ^-/Σ^0 measurement from this data, however, corresponds to the isospin-$\frac{3}{2}$ exchange, where the calculated ratio of $\frac{\sigma(\Sigma^-)}{\sigma(\Sigma^0)}$ from the comparison of

Target	$\theta_{\gamma K}$	Σ^-/Σ^0 (SIMC1)	Σ^-/Σ^0 (SIMC2)
D	0	0.573 ± 0.092	0.535 ± 0.085
^{3}He	0	1.234 ± 0.244	0.713 ± 0.142
^{3}He	6	0.508 ± 0.118	0.554 ± 0.128
^{3}He	12	0.509 ± 0.136	0.537 ± 0.267
^{4}He	0	0.734 ± 0.170	0.496 ± 0.106
^{4}He	6	0.307 ± 0.077	0.345 ± 0.106
^{4}He	12	0.286 ± 0.072	0.381 ± 0.131

Table 5.9: Cross section ratios of Σ^-/Σ^0 for SIMC1 and SIMC2.

the Clebsch-Gordan coefficients is 0.5. The W-dependence suggests that the Δ resonances beyond W = 1.8 GeV should not contribute to the cross section [11]. Perhaps new theoretical analyses will need to be done for this data. Ratios of the cross sections, Λ/Σ^0 and Σ^0/Σ^-, are shown in Figures 5.24 and 5.25.

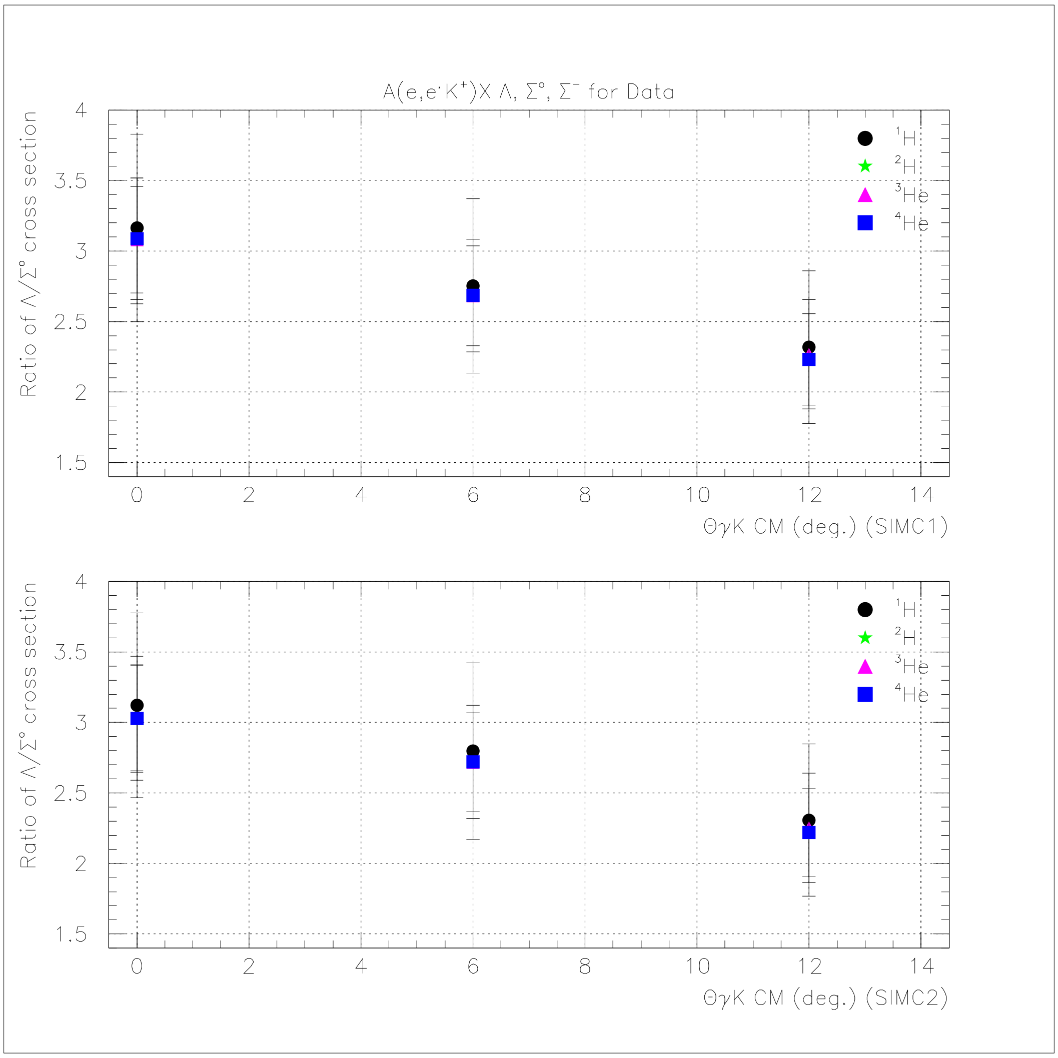

Figure 5.24: The Λ/Σ^0 ratios of the experimental cross sections. The symbols represent each target.

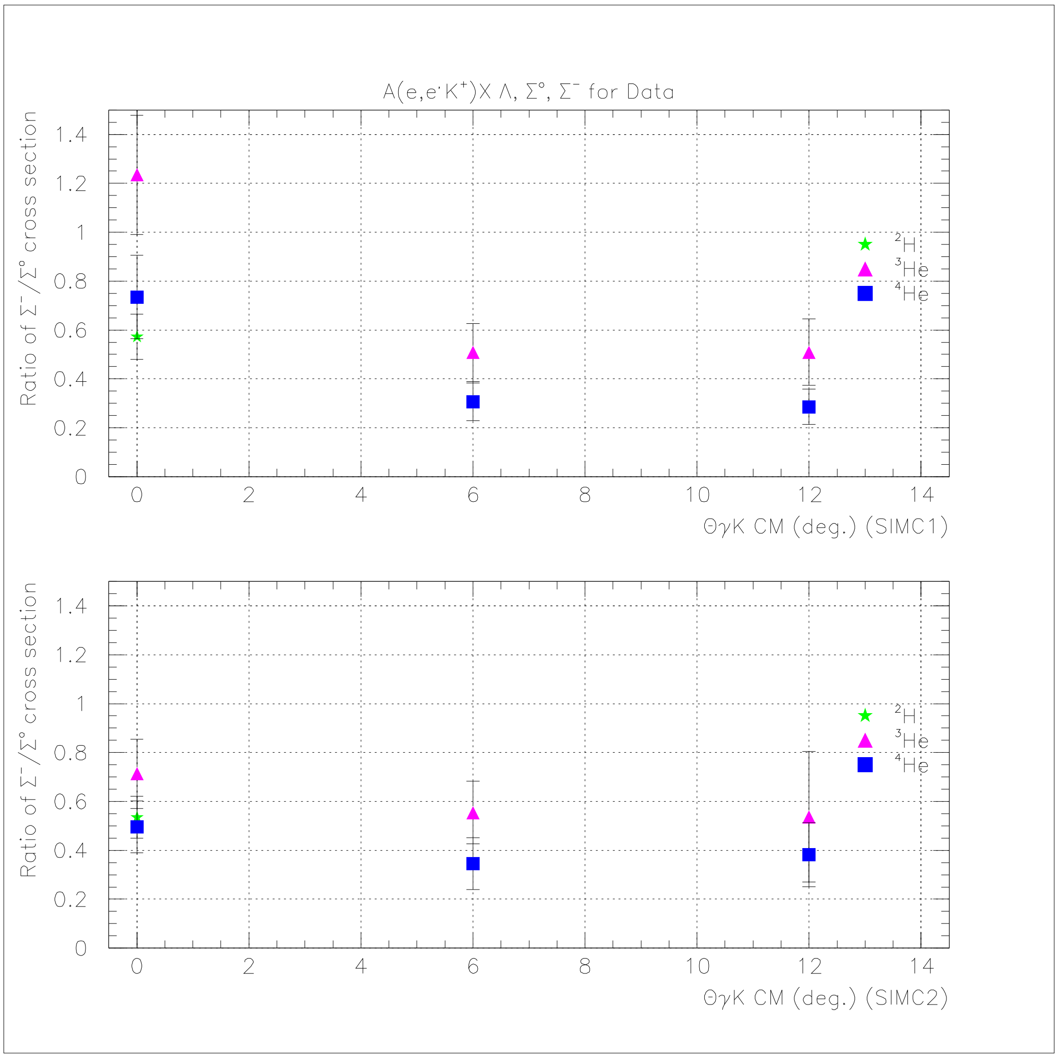

Figure 5.25: The Σ^-/Σ^0 ratios of the experimental cross sections. The symbols represent each target.

Target	p_{eff} (SIMC1)	p_{eff} (SIMC2)
H	1.000 ± 0.133	1.000 ± 0.133
D	0.886 ± 0.092	0.891 ± 0.093
^{3}He	1.989 ± 0.191	2.164 ± 0.198
^{4}He	1.793 ± 0.184	1.891 ± 0.188

Table 5.10: Effective proton number for $\theta_{\gamma K} = 0^o$ for SIMC1 and SIMC2.

5.6 Λ Comparison

An interesting result was the comparison of Λ scaling factors on the nuclear targets to hydrogen. The assumption was made that the proton in ^{3,4}He can be treated as a free proton and, the Λ/Σ^0 production from helium would be the same as hydrogen, with some differences in the kinematic effects due to the final states. An important check on this procedure would be comparing the Λ scaling factor from hydrogen to that of ^{3}He and ^{4}He per nucleon. As shown in Figure 5.26, the ratio averages $\sim$ 1.01 for ^{3}He and $\sim$ 0.922 for ^{4}He across each setting.

The effective proton number was calculated using the Λ cross section from hydrogen as the elementary cross section. The D/H ratio for the Λ cross section is 0.889 ± 0.151. This ratio is considerably lower than the previous D/H ratio of 0.987. The $\theta_{\gamma K}$ for the 1996 data was 1.5^o at $Q^2 = 0.38$ (GeV/c)^2. Recall that $Q^2 = 0.35$ (GeV/c)^2 for this data. The average ^{3}He/H ratio for $\theta_{\gamma K} = 0^o$ is 2.077 ± 0.195 and 1.842 ± 0.186 for ^{4}He/H. These results agree well within error with the expectation of 2 due to the 2:1 proton number ratio of helium to hydrogen. Perhaps the lower value for ^{4}He corresponds to some kaon absorption in the nucleus [35] [36]. Table 5.10 gives a complete list of the effective proton number determined for $\theta_{\gamma K} = 0^o$. Each value includes a 3% correction due to the differences in kinematic effects. Figure 5.27 shows the previously measured Λ cross section on hydrogen, deuterium, carbon and aluminum for the similar Q^2 values. The bottom plots shows the resulting effective proton number for each target.

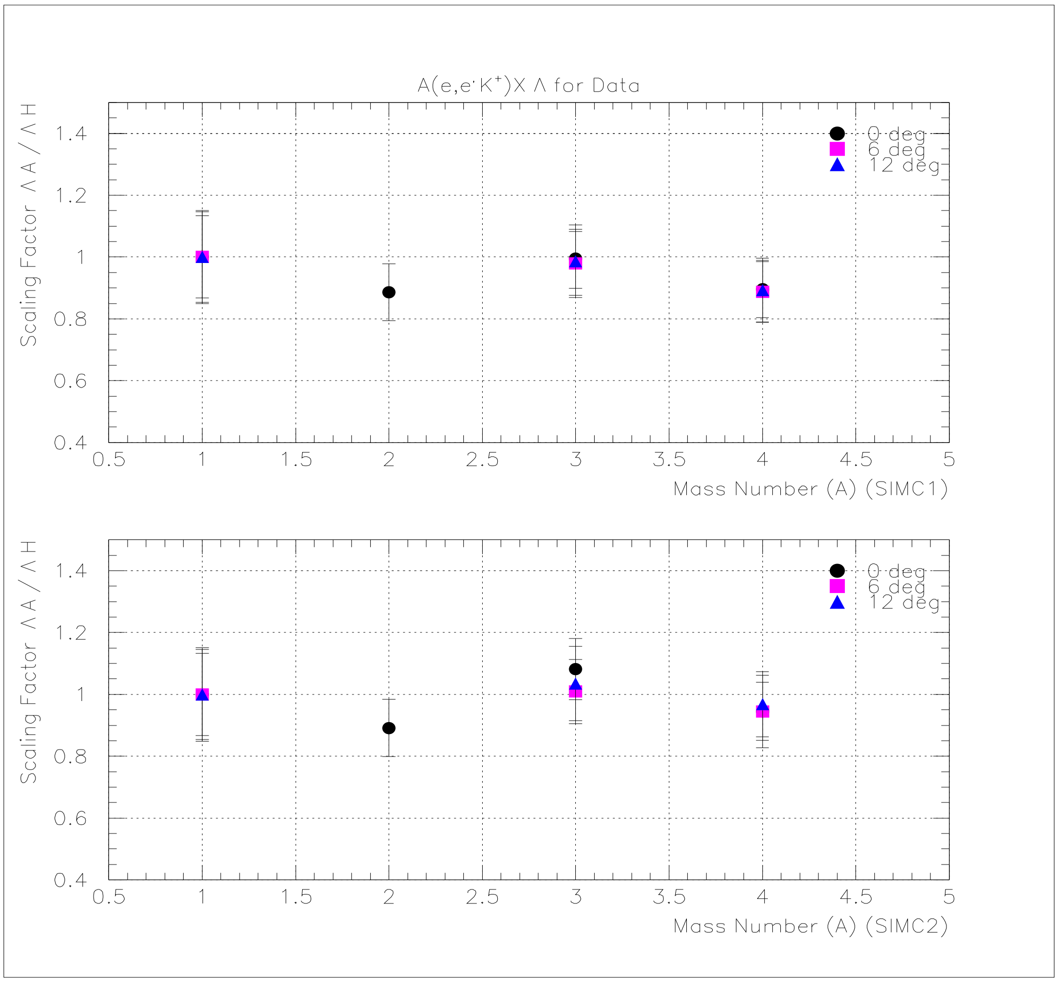

Figure 5.26: Λ scaling factors for each target normalized to hydrogen.

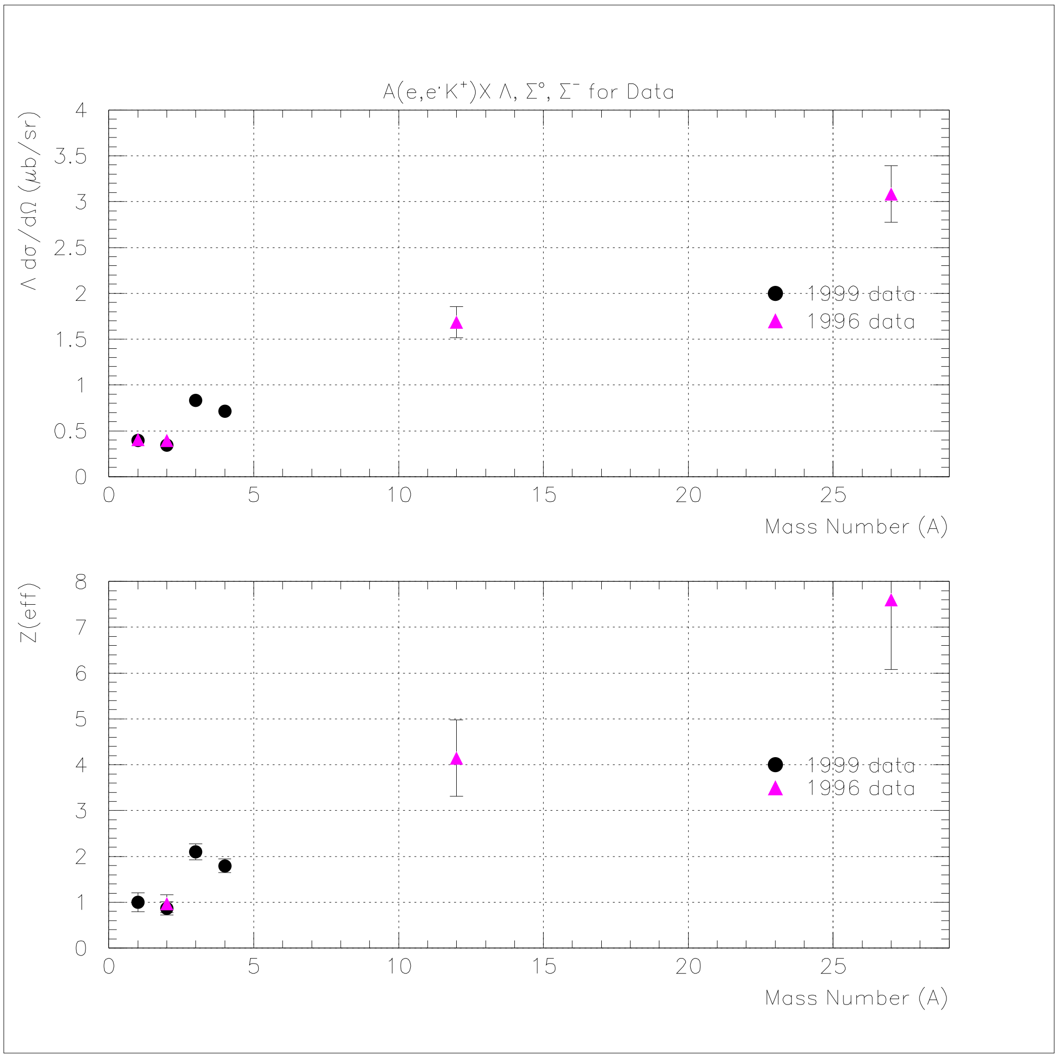

Figure 5.27: The Λ cross section and effective proton number for $\theta_{\gamma K} = 0^o$. Shown are the present data and 1996 kaon electroproduction data which includes the aluminum and carbon targets.

5.7 Bound Region

One of the motivations of **E91-016** was to produce bound Λ-hypernuclear states from (e,e'K$^+$) reactions on ^{3}He and ^{4}He targets and search for bound Σ-hypernuclear states. To maximize the *sticking* probability of the lambda in the nucleus, data were taken at far forward angles so the coincident kaons were detected in the direction of the virtual photon. The momentum transferred to the residual system was lowest at these settings. With less momentum transfer, the lambda produced from the proton has a greater probability to remain in the nucleus to form a hypernuclear bound state. Peak widths are predicted to be 4 MeV for $^4{}_\Lambda H$ and $\sim$ 5 MeV for $^4{}_\Sigma H$. Subtractions of the data and simulation missing mass spectra can be used to determine the contribution of physical processes other than quasifree kaon electroproduction. After the contribution from the random coincidences and the target windows were subtracted from the raw missing mass distributions, the final state interactions are clearly seen in both ^{3}He and ^{4}He. Subtraction of the quasifree ^{4}He simulation from the data left a statistically significant enhancement near lambda threshold. This could be evidence for a bound Λ state, as seen in Figure 5.28. In the ^{4}He(e,e'K$^+$) reaction, the 1^+ excited state is predicted to be favorable over the 0^+ ground state and have a larger cross section [37]. An accurate measurement of a hyperon bound state would require a model of FSI for ^{3}He and ^{4}He. The difficulty lies with the several possible final states in both ^{3}He and ^{4}He.

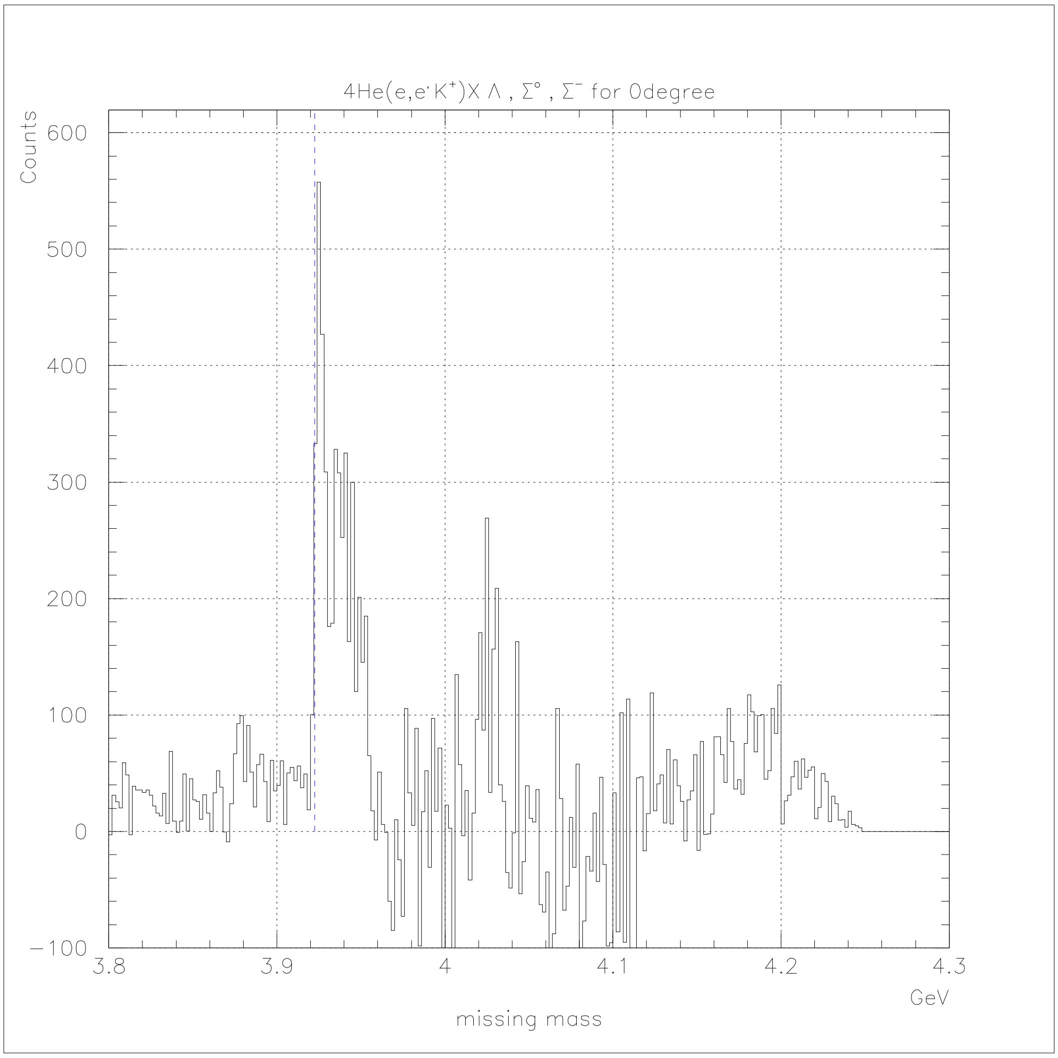

Figure 5.28: ^{4}He(e,e'K$^+$) $\theta_{\gamma K} = 0^o$ data after SIMC subtraction. The dashed line indicates the threshold for a Λ bound state at 0^+ ground state.

CHAPTER 6

Conclusion

Experiment **E91-016** presented the first data of kaon electroproduction on ^{3}He and ^{4}He targets at Thomas Jefferson National Accelerator Facility. The scattered electron and kaon were detected in coincidence using the standard Hall C configuration of the HMS and SOS. An abundance of quality data were obtained at $Q^2 = 0.35$ GeV^2 for $\theta_{\gamma K} = 0^o, 6^o$, and 12^o for an angular distribution. An opening angle of just 28.3^o was achieved, minimizing the momentum transfer to the nucleus. The missing mass distribution of the quasifree production for three hyperon channels, Λ, Σ^0, and Σ^-, were indistinguishable due to the increased Fermi motion of the target nucleons. Because quasifree kaon production from a helium nucleus is still not well understood, two separate simulations were used to describe the data. The first simulation used a pure momentum distribution from Ciofi degli Atti, while the other contained a full spectral function taken from O. Benhar. Cross sections of Λ, Σ^0, and Σ^- were determined by assuming the nucleons are free in the nuclear medium. The production ratio of Λ/Σ^0 from hydrogen was measured for each setting. Because there was no clear separation between the Σ^0 and Σ^- regions, this ratio from hydrogen was assumed to remain constant for ^{3}He and ^{4}He in order to extract the Σ^- cross section. By scaling the Σ^0 cross section on the helium targets as Σ^0 on hydrogen, the Σ^- missing mass could be separated from the entire missing mass distribution and the cross section measured.

The angular distribution of the cross sections gave information on the angular dependence of the production mechanisms for each hyperon. In Λ, there was a slight increase from $\theta_{\gamma K} = 0^o$ to 6^o. This increase could indicate a contribution from the interference terms, $\frac{d\sigma_{LT}}{d\Omega_{cm}}$ and $\frac{d\sigma_{TT}}{d\Omega_{cm}}$. The effect of this contribution becomes small compared to the behavior of the cross section with t as $\theta_{\gamma K}$ increased to 12^o. Neither Σ^- or Σ^o show a strong cross section dependence with $\theta_{\gamma K}$. The ratio Σ^-/Σ^0 was found to be 0.60 for ^{3}He and 0.41 for ^{4}He. The value for ^{3}He is in good agreement a previous measurement of 0.61 in 1996 on deuterium. The measurements agree with the pure isospin-$\frac{3}{2}$ exchange, where the calculated Σ^-/Σ^0 ratio is 0.5, rather than 2.0, which corresponds to the pure isospin-$\frac{1}{2}$ exchange in t-channel reactions. The ratio of Λ on deuterium, ^{3}He, and ^{4}He to hydrogen was also measured to determine the validity of the statement that the protons in the heavier targets can be treated as free protons. The effective proton number was obtained by using the Λ cross section hydrogen as the elementary process. The average results were 2.077 ± 0.195 for ^{3}He and 1.842 ± 0.186 for ^{4}He. Some effects due to kaon absorption in the nucleus could explain the lower effective proton number in ^{4}He.

One of the goals of **E91-016** was to measure Λ-hypernuclear states from (e,e'K$^+$) reactions on ^{3}He and ^{4}He targets and search for bound Σ-hypernuclear states. The quasifree contribution was subtracted as background so threshold FSI could be observed. A sharp peak was seen just below the threshold for Λ production on the ^{4}He, $\theta_{\gamma K} = 0^o$ data. This peak was a possible Λ bound state with contributions from FSI. The energy resolution in Hall C would not allow the narrow bound state peak to be resolved from FSI effects. An accurate measurement of a hyperon bound state would require a model of FSI for ^{3}He and ^{4}He. The difficulty lies with the several possible final states in both ^{3}He and ^{4}He. Although a small contribution compared to the entire distribution, the inclusion of FSI effects could result in significant differences in the hyperon cross sections. Perhaps the largest weakness of this analysis was the lack of FSI effects in the simulation. Currently, the **E91-016** collaboration is attempting to model Y-N FSI on ^{3}He and ^{4}He which could quantify the strength of the Λ-n interaction and provide a measurement of the Λ-n scattering length [34]. Future programs in Hall C at Jefferson Lab certainly have the ability to resolve final state interactions on nuclear targets and measure hyperon bound states [8].

BIBLIOGRAPHY

[1] J. D. Walecka, *Theoretical Nuclear and Subnuclear Physics.* Oxford, New York, 1995.

[2] T. Donnelly and S. Cotanch, Using kaon electromagnetic production to study hypernuclear systems. In *Proceedings of the 1984 Workshop on Electron and Photon Interactions at Medium Energies*, pages 7–1 – 7–24, 1985.

[3] J. C. David et al., Electromagnetic production of associated strangeness. In *Proceedings of the 14th International Few-Body Conference*, November 1995.

[4] B. Zeidman, Electroproduction of kaons and light hypernuclei. PR-89-013, CEBAF Internal Report (unpublished), 1991.

[5] D. E. Groom et al., *Eur. Phys. Jour.*, C15:8, 2000.

[6] G. Niculescu et al., *Phys. Rev. Lett.*, 81:1805, 1998.

[7] L. Tang and K. Baker, *Hypernuclear Physics Program at CEBAF.* Hall C Internal Report, April 1992.

[8] L. Tang and O. Hashimoto, In *Proceedings of Jlab Sponsored Workshop on Hypernuclear Physics with Electromagnetic Probes*, pages pp. 1–23, December 1999.

[9] W. Hinton, Ph.D. dissertation, Hampton University (unpublished), 2000.

[10] T. Nagae et al., *Phys. Rev. Lett.*, 80:1605, 1998.

[11] J. Cha, Ph.D. dissertation, Hampton University (unpublished), 2000.

[12] J. Cha, Private communication, 2001.

[13] D. M. Koltenuk, Ph.D. dissertation, University of Pennsylvania (unpublished), 1999.

[14] B. Zeidman, Private communication, 2001.

[15] T. Azemoon et al., *Nuc. Phy.*, B95:77–97, 1975.

[16] M. Sotona and S. Frullani, *Progess of Theoretical Physics Supplement*, 117:151–175, 1994.

[17] P. Gueye, Private communication, 2001.

[18] R. Carlini et al., *Hall C Operating Manual.* Hall C internal report (unpublished), 1995.

[19] J. Dunne, *Cryo and Dummy Target Information.* CEBAF Hall C Document (unpublished), 1998.

[20] J. Dunne, Private communication, 2001.

[21] C. Armstrong, Private communication, 2000.

[22] C. Armstrong, *Hall C Time of Flight Fitting Code.* Hall C internal report (unpublished), 1998.

[23] J. Arrington, Ph.D. dissertation, Ohio University (unpublished), 1998.

[24] R. M. Mohring, Ph.D. dissertation, University of Maryland (unpublished), 1999.

[25] S. A. Wood, *The CEBAF Test Package.* Continuous Electron Beam Accelerator Facility, Newport News, Virginia, January 1995.

[26] *HBOOK Reference Manual*, CERN Program Library Long Writeups Y250, 1995.

[27] K. Assamagan, D. Dutta, and P. Welch, *Hall C Matrix Elements Optimization.* CEBAF Hall C Internal Report, 1997.

[28] J. Reinhold, Private communication, 2000.

[29] D. Dutta, Ph.D. dissertation, Northwestern University (unpublished), 1999.

[30] J. Arrington, *A B C SIMC*, July 2001. CEBAF Internal Report (unpublished).

[31] C. Ciofi degli Atti and S. Simula, *Phys. Rev.*, C53:1689–1710, 1996.

[32] O. Benhar et al., *Phys. Rev.*, C44:2328, 1991.

[33] M. Berz, *COSY Infinity Version 7 Reference Manual.* Michigan State University, NSCL Technical Report MSUCL-977, 1995.

[34] F. Dohrmann, Private communication, 2000.

[35] R. Ent, Private communication, 2001.

[36] W. Hinton, Private communication, 2002.

[37] T. Saito et al., Electroproduction of hypernuclei in 3He and 4He. Hall A Jefferson Lab Proposal (unpublished).

VITA

Alicia Renee Uzzle was born in Salisbury, Maryland, on October 31, 1971 to Linda and Grant Wallop. She graduated from Chincoteague High School in 1989 and went on to pursue and complete her Bachelor of Arts and Master of Science degrees in physics at Hampton University in 1995. She became a physics teacher for Newport News Public Schools, where she worked for three years before returning to Hampton University in 1998 to complete her graduate studies. In 1999, she was married to Robert L. Uzzle, Jr. They have three children, Robert, Aaron, and Jared. She completed her dissertation work in experimental nuclear physics in May 2002 and was awarded her Ph.D. Currently, Alicia and her family reside in Hampton, Virginia.